



**pennsylvania**

DEPARTMENT OF TRANSPORTATION

# Faulting Model Improvements for MEPDG

FINAL REPORT

August 2021

By (PI) Lev Khazanovich  
University of Pittsburgh

COMMONWEALTH OF PENNSYLVANIA  
DEPARTMENT OF TRANSPORTATION

CONTRACT # 4400018535  
WORK ORDER # PIT 001/511801



<b>1. Report No.</b> FHWA-PA-2021-005-PITT WO 001	<b>2. Government Accession No.</b>	<b>3. Recipient's Catalog No.</b>	
<b>4. Title and Subtitle</b> Faulting Model Improvements for MEPDG		<b>5. Report Date</b> August 2021	<b>6. Performing Organization Code</b>
<b>7. Author(s)</b> Lev Khazanovich, Julie Vandebossche, Lucio Salles, Sushobhan Sen, Charles Donnelly, Katelyn Kosar		<b>8. Performing Organization Report No.</b>	
<b>9. Performing Organization Name and Address</b> Department of Civil and Environmental Engineering University of Pittsburgh Benedum Hall 3700 O'Hara Street   Pittsburgh, PA 15261		<b>10. Work Unit No. (TRAIS)</b>	<b>11. Contract or Grant No.</b> XXX
<b>12. Sponsoring Agency Name and Address</b> The Pennsylvania Department of Transportation Bureau of Planning and Research Commonwealth Keystone Building 400 North Street, 6 <sup>th</sup> Floor Harrisburg, PA 17120-0064		<b>13. Type of Report and Period Covered</b> July 2019 – August 2021	<b>14. Sponsoring Agency Code</b>
<b>15. Supplementary Notes</b> PI contact info: 742 Benedum Hall, 3700 O'Hara Street, Pittsburgh, PA 15261 – lev.k@pitt.edu			
<b>16. Abstract</b> <p>Accurate joint transverse faulting prediction is essential for proper pavement design. Departments of transportation are encouraged to evaluate, recalibrate, and even modify the faulting model if discrepancies between predicted and field measured faulting are observed. The Pennsylvania Department of Transportation (PennDOT) identified a series of problems with Pavement ME faulting prediction for jointed plain concrete pavements (JPCP). Moreover, the current design of bonded concrete overlays on asphalt (BCOA) lacks a faulting model that simulates the different aspects of the BCOA structure. To address these issues, this project had two main objectives: reevaluate and modify Pavement ME faulting model for JPCP and develop a singular faulting model for BCOA.</p> <p>For JPCP, the faulting predictions of the current version of Pavement ME with various reliability levels were evaluated using PennDOT's Road Management System (RMS). The approach adopting RMS data shows potential for a new use of these types of databases for calibration of distress prediction model evaluation. In addition, a novel methodology accounting for the so-called "survival issue" of the pavement performance databases in model evaluation was introduced. It was found that Pavement ME greatly overpredicted faulting for most cases. Thus, the faulting model was modified and calibrated accordingly improving prediction accuracy.</p> <p>For BCOA, a series of Artificial Neural Networks (ANNs) were developed to estimate the structural response of BCOA to vehicle and environmental loading. This response was quantified in terms of the difference between the deflection basins on the loaded and unloaded slabs and related to Differential Energy (DE). Differential energy is used to characterize damage accumulation which is related to the predicted faulting. The ANNs were then combined with field measurements of faulting to calibrate a faulting model similar to the JPCP faulting model used in Pavement ME but considering the different structural aspects of BCOA. As is the case with the modified JPCP model, the new BCOA model shows good agreement with field data.</p>			
<b>17. Key Words</b> Joint transverse faulting; faulting model; jointed plain concrete pavement; road management system; bonded concrete over asphalt; Artificial Neural Networks		<b>18. Distribution Statement</b> No restrictions. This document is available from the National Technical Information Service, Springfield, VA 22161	
<b>19. Security Classif. (of this report)</b> Unclassified	<b>20. Security Classif. (of this page)</b> Unclassified	<b>21. No. of Pages</b> 149	<b>22. Price</b>

## **ACKNOWLEDGEMENT**

This work was sponsored by the Pennsylvania Department of Transportation and the U.S. Department of Transportation, Federal Highway Administration.

## **DISCLAIMER**

The contents of this report reflect the views of the authors who are responsible for the facts and the accuracy of the data presented herein. The contents do not necessarily reflect the official views or policies of the U.S. Department of Transportation, Federal Highway Administration, or the Commonwealth of Pennsylvania at the time of publication. This report does not constitute a standard, specification or regulation.

## Table of Contents

1 INTRODUCTION .....	12
2 CHAPTER 1: EVALUATION OF THE FAULTING MODEL FOR PENNSYLVANIA CONDITIONS .....	13
2.1 Literature Review of Faulting Models .....	13
2.1.1 Mechanistic-Empirical Faulting Models.....	13
2.1.1.1 FHWA PAVESPEC 3.0 Faulting Model .....	13
2.1.1.2 MEPDG Faulting Model.....	15
2.1.1.3 MEPDG Faulting Reliability Analysis .....	19
2.1.1.4 PittRigid-ME.....	20
2.3 Pavement ME Sensitivity Analysis.....	20
2.4 Faulting Field Data Collection and Processing.....	23
2.4.1 LTPP Faulting Data .....	24
2.4.2 PennDOT RMS Faulting Data Processing.....	25
2.4.2.1 Permanently Excluded Data.....	25
2.4.2.2 Questionable Data.....	26
2.5 Faulting Data Statistical Analysis .....	27
2.5.1 Critical Faulting Per Traffic Level.....	30
2.6 Evaluation of Pavement ME Faulting Model Based on Pennsylvania Field Data .....	32
2.6.1 General Case 1: Joint Spacing 15 ft.....	32
2.6.2 General Case 2: Joint Spacing 20 ft.....	33
2.6.3 Comparison of Pavement ME Faulting Model with Other Models Regarding Field Data .....	34
3 CHAPTER 2: JPCP FAULTING MODEL IMPROVEMENT .....	36
3.1 Modification of the Faulting Reliability Model.....	37
3.1.1 Pavement ME Reliability Faulting Model .....	37
3.1.2 The “Survivals” Issue: Potential Rehabilitated Sections in the Faulting Database .....	38
3.1.3 Step-by-Step Procedure for RMS Calibrated Reliability Model Considering Potential Rehabilitated Observations .....	40
3.1.3.1 Step 1: Database Group Arrangement .....	40
3.1.3.2 Step 2: Group Data Organization.....	42
3.1.3.3 Step 3: Distress Prediction Variability Analysis.....	42
3.1.3.4 Step 4: Standard Deviation and Intercept Models .....	44
3.2 Reliability Model Validation .....	47

3.3	Faulting Model Modifications .....	53
3.3.1	Faulting Model Modification and Calibration .....	56
3.3.1.1	Coefficients Calibration .....	58
3.3.2	Modified Model Validation .....	62
3.3.3	Modified Model Sensitivity Analysis .....	66
3.3.3.1	Effect of high level of concrete coefficient of thermal expansion (COTE).....	68
3.3.3.2	Effect of widened lanes.....	71
3.3.4	Design Examples .....	73
4	CHAPTER 3: FAULTING MODEL FOR BCOA .....	77
4.1	Calibration Sections .....	77
4.2	Develop Structural Model and Artificial Neural Networks .....	78
4.2.1	Computational Models.....	78
4.2.1.2	Interface Between Layers .....	80
4.2.1.3	Joints .....	81
4.2.1.4	Wheel and Thermal Loads .....	81
4.2.1.5	Finite Element Mesh.....	82
4.2.1.6	Model Validation .....	83
4.2.2	Artificial Neural Network Response Prediction Models .....	86
4.2.2.1	Critical Response Parameters .....	86
4.2.2.2	Development of Artificial Neural Networks.....	88
4.2.2.3	Special consideration for joint spacing.....	90
4.2.2.4	ANN Training.....	91
4.2.2.5	ANN Predictors.....	91
4.2.3	Validation.....	91
4.2.4	Sensitivity Analysis .....	100
4.2.5	Summary .....	114
4.3	Joint Faulting Model Development .....	114
4.3.1	Introduction.....	114
4.3.2	Faulting Model Framework .....	114
4.3.2.1	Climate.....	116
4.3.2.2	Traffic .....	118
4.3.2.3	Model Inputs .....	123
4.4	Model calibration .....	131
4.4.1	Reliability model.....	133

4.4.2 Examples .....	135
4.5 BCOA-ME Webtool .....	136
5 CONCLUSIONS.....	139
References.....	141
Appendix A.....	144
Appendix B .....	147

## List of Figures

Figure 1 – Pavement ME faulting prediction for different levels of traffic .....	21
Figure 2 – Pavement ME faulting prediction for different slab thicknesses and dowel bar diameters .....	21
Figure 3 – Pavement ME faulting prediction for different coefficients of thermal expansion (CTE x 10 <sup>-6</sup> /°F) .....	22
Figure 4 – Pavement ME faulting prediction for different joint spacing.....	22
Figure 5 – Pavement ME faulting prediction for different slab widths .....	22
Figure 6 – Pavement ME faulting prediction for different tied PCC shoulders and other types of shoulders .....	23
Figure 7 – Pavement ME faulting prediction for different pavement bases .....	23
Figure 8 – LTPP edge and wheel path faulting versus pavement age (a and b) and traffic (c and d) for Pennsylvania .....	24
Figure 9 – LTPP edge and wheel path faulting versus pavement age (a and b) and traffic (c and d) for Ohio.....	25
Figure 10 – Observations distribution regarding (a) pavement age and (b) average joint faulting .....	27
Figure 11 – Average joint faulting versus (a) pavement age, (b) cumulative ESALs and (c) average IRI.....	29
Figure 12 – Average joint faulting per traffic levels (ESAL x10 <sup>7</sup> ).....	30
Figure 13 – Critical average faulting (90% reliability) versus cumulative traffic .....	30
Figure 14 – Pavement ME faulting prediction versus field data: General Case 1 .....	33
Figure 15 – Pavement ME faulting prediction versus field data: Sub-Case 1 .....	33
Figure 16 – Pavement ME faulting prediction versus field data: General Case 2 .....	34
Figure 17 – Comparison of different versions of faulting models.....	35
Figure 18 – Faulting predictions using a single model with different reliability models .....	38
Figure 19 – Hypothetical performance model validation (a) using conventional field data collection, and (b) considering rehabilitated sections.....	39
Figure 20 – PA JPCP rehabilitation probability in relation to pavement age.....	40
Figure 21 – Predicted faulting groups range selection.....	41
Figure 22 – Faulting prediction variability versus standard normal deviate (Z) for Group 3 .....	43
Figure 23 – Faulting prediction variability versus standard normal deviate (Z) .....	44
Figure 24 – Faulting variability regression (a) slope and (b) intercept versus average predicted faulting .....	45
Figure 25 – Faulting predictions using a single faulting model (NCHRP 20-07 calibration) with different reliability models.....	46
Figure 26 – Pavement ME faulting predictions using the current and the RMS calibrate reliability models (95% reliability) for (a) 15 ft JPCP and (b) 20 ft. JPCP.....	47
Figure 27 – Pavement ME faulting predictions using the current and the RMS calibrate reliability models for (a) 15 ft JPCP and (b) 20 ft JPCP considering rehabilitated sections.....	49
Figure 28 – Reliability models validation for the standard design of Design 1 (15 ft JPCP).....	50
Figure 29 – Reliability models validation for exceptions of the standard design of Design 1 (15 ft JPCP).....	51
Figure 30 – Reliability models validation for the standard design of Design 2 (20 ft JPCP).....	52

Figure 31– Reliability models validation for exceptions of the standard design of Design 2 (20 ft JPCP).....	53
Figure 32 – Faulting prediction (95% reliability) using the current and the modified faulting models.....	58
Figure 33 – Coefficient sensitivity analysis.....	59
Figure 34 – C9 sensitivity analysis.....	60
Figure 35 – Iteration result to equalize faulting predictions between current and modified model considering intercept model.....	60
Figure 36 – Faulting predictions using different model calibrations for (a) 50% and (b) 95% reliability.....	62
Figure 37 – Modified model validation for the standard design of Design 1 (15 ft JPCP).....	63
Figure 38 – Modified model validation for exceptions of the standard design of Design 1 (15 ft JPCP).....	64
Figure 39 – Modified model validation for the standard design of Design 2 (20 ft JPCP).....	65
Figure 40 – Modified model validation for exceptions of the standard design of Design 2 (20 ft JPCP).....	66
Figure 41 – Modified model faulting prediction for different levels of traffic.....	67
Figure 42 – Modified model faulting prediction for different slab thicknesses and dowel bar diameter.....	67
Figure 43 – Modified model faulting prediction for different joint spacing.....	68
Figure 44 – Modified model faulting prediction for different pavement bases.....	68
Figure 45 – Comparative COTE ( $10^{-6}$ ) sensitivity analysis of Pavement ME and Modified Model faulting predictions (95% reliability).....	69
Figure 46 – Comparative excessively high COTE analysis of Pavement ME and Modified Model faulting predictions (95% reliability) using ATPB.....	70
Figure 47 – Design comparison of Pavement ME and Modified Model faulting predictions (95% reliability) using ATPB.....	70
Figure 48 – Comparative lane width analysis of Pavement ME and Modified Model faulting predictions (95% reliability) using (a) 1.25 in and (b) 1.5 in dowels.....	71
Figure 49 – LTPP data for JPCP constructed with (a) conventional lane width (10 to 12 ft), and (b) widened lanes (13 and 14 ft).....	72
Figure 50 - Faulting predictions for Design 1 using Pavement ME (PA calibration) with dowel diameter input of (a) 1.25 in and (b) 1.5 in.....	74
Figure 51 - Faulting predictions for Design 1 using the modified model.....	75
Figure 52 - Comparative faulting predictions for Design 2 with two dowel diameters.....	75
Figure 53 – Comparative faulting predictions for Design 3.....	76
Figure 54 – Comparative faulting predictions for Design 4 using different dowel diameters.....	76
Figure 55 – Model configuration.....	79
Figure 56 – Debonded region at the interface for the 8-slab system (PCC depth only).....	80
Figure 57 – Axle configuration.....	82
Figure 58 – Model validation.....	85
Figure 59 – Deflection basin definition.....	87
Figure 60 - Faulting due to pumping of the different layers.....	90
Figure 61 – Basins for 8-slab model (joint activates only through PCC).....	93
Figure 62 – Corner deflections for 8-slab model (joint activates only through PCC).....	93



Figure 63 – Corner deflections due to temperature for 8-slab model (joint activates only through PCC).....	94
Figure 64 – Basins for 8-slab model (joint activation is full-depth).....	94
Figure 65 – Corner deflections for 8-slab model (joint activation is full-depth).....	95
Figure 66 – Corner deflections due to temperature for 8-slab model (joint activation is full-depth).....	95
Figure 67 – Basins for 4-slab model (joint activation is full-depth).....	96
Figure 68 – Corner deflections for 4-slab model (joint activation is full depth).....	96
Figure 69 – Corner deflections due to temperature for 4-slab model (joint activation is full-depth).....	97
Figure 70 – Validation of ANNs.....	99
Figure 71 – Parameters for the sensitivity analysis of the ANNs: single axle – layer thicknesses.....	101
Figure 72 – ANNs sensitivity analysis: tandem axle – layer thicknesses.....	103
Figure 73 – ANNs sensitivity analysis: modulus of subgrade reaction.....	105
Figure 74 – ANNs sensitivity analysis: presence of dowels.....	107
Figure 75 – ANNs sensitivity analysis: temperature difference – PCC thickness.....	109
Figure 76 – ANNs sensitivity analysis: temperature difference – asphalt thickness.....	111
Figure 77 – ANNs sensitivity analysis: temperature difference – modulus of subgrade reaction.....	113
Figure 78 – Faulting model framework.....	115
Figure 79– Predictive faulting model framework.....	115
Figure 80 – Predictive faulting incremental analysis.....	123
Figure 81 - Measured vs predicted faulting.....	133
Figure 82 - Reliability models for joint activation through (a) PCC only and (b) both PCC and HMA.....	135
Figure 83 - Predicted and measured faulting as a function of ESALs for MnROAD sections: (a)-(c) show faulting in sections with joint activation through both the PCC and asphalt, while (d)-(f) through the PCC only.....	136

## List of Tables

Table 1 – Statistical comparison between design features effect on critical joint faulting.....	31
Table 2 – Input parameters for Pavement ME faulting prediction .....	32
Table 3 – Faulting coefficients from previous Pavement ME calibrations .....	34
Table 4 - National and State calibrated coefficients for faulting reliability model .....	37
Table 5 – Basic statistical parameters for predicted faulting groups .....	41
Table 6 – Probability of Potential rehabilitated observations in each group .....	41
Table 7 – Database organization example (G5).....	42
Table 8 – National and PA reliability calibrations in comparison to the proposed calibration ....	45
Table 9 – Prediction performance evaluation of the faulting model using the current and RMS calibrated reliability models.....	55
Table 10 - Modification of transverse joint load transfer efficiencies for .....	57
Table 11 – Faulting model calibration coefficients .....	61
Table 12 – Range of parameters for calibration sections.....	78
Table 13 – Mesh convergence study parameters. ....	83
Table 14 – Pavement parameters for validation sections.....	84
Table 15 – Overall design matrix.....	88
Table 16 – Predictability of ANNs .....	92
Table 17 –Parameters for the sensitivity analysis of the ANNs: single axle – layer thicknesses	100
Table 18 – Parameters for the sensitivity analysis of the ANNs : tandem axle – layer thicknesses. .....	102
Table 19 – Parameters for the sensitivity analysis of the ANNs : modulus of subgrade reaction .....	104
Table 20 – Parameters for the sensitivity analysis of the ANNs: presence of dowels.....	106
Table 21 – Parameters for the sensitivity analysis of the ANNs : temperature difference – PCC thickness.....	108
Table 22 – Parameters for the sensitivity analysis of the ANNs: temperature difference – asphalt thickness.....	110
Table 23 – Parameters for the sensitivity analysis of the ANNs: temperature difference – modulus of subgrade reaction. ....	112
Table 24 – Hourly truck traffic distributions from Pavement ME [1].....	118
Table 25 – Function used in computing/forecasting truck traffic over time.....	119
Table 26 – Lane distribution factors for multiple-lane highways [1]. ....	119
Table 27 – Axles per 1000 trucks for different road categories. Source: “Design of Concrete Pavement for City Streets” [45].....	120
Table 28 – ADTT given for different road categories and classifications [45]. ....	122
Table 29 – Examples of (a) an input text file and (b) an asphalt stiffness text file. ....	124
Table 30 – <i>LTEbase</i> for different base types [1].....	125
Table 31 – PCC set temperature for cement content and mean temperature during month of paving (°F). ....	126
Table 32 – PCC overlay drying shrinkage strain relationship [1]. ....	126
Table 33 – Erodibility classification (adopted from [1]). ....	128
Table 34 - Calibrations sections for joint activation through PCC only.....	131
Table 35 - Calibrations sections for joint activation through both PCC and HMA.....	132
Table 36 - Calibration coefficients .....	133

Table 37 - Reliability and corresponding standardized normal deviate. ....	134
Table 38 – BCOA-ME webtool with faulting calculation.....	137

# 1 INTRODUCTION

Transverse joint faulting is a deterioration mechanism that can substantially impact ride quality in jointed concrete pavements. This presents major negative implications regarding pavement life cycle and vehicle costs. Generally, joint faulting is defined as the difference in elevation between adjacent, transverse joints. This difference is measured approximately 1 ft from the slab edge, meaning from the longitudinal joint for a conventional lane width or from the right-most lane paint stripe for a widened slab. Joint faulting, usually, is developed under a combination of different underlying distresses, design, and loading parameters such as poor load transfer across a joint or crack, heavy axle loads, free moisture beneath the pavement, and erosion in the supporting layers. Therefore, comprehensive models for joint faulting prediction that account for different parameters are essential for a successful pavement design. Such models must present coherent prediction results when compared to existing joint faulting field data. If the model fails to represent field data adequately, a reevaluation and improvement of faulting models to increase accuracy in joint faulting predictions is needed.

The AASHTOWare Pavement ME, developed from the Mechanistic-Empirical Pavement Design Guide (MEPDG), presents one of the most modern examples of faulting prediction models. However, as encouraged by the MEPDG, the model must be tested and evaluated with field data from different states and areas around the country. Any discrepancies between faulting predictions and field performance should be addressed by a careful recalibration or modification of the model. For Pennsylvania conditions, the Pennsylvania Department of Transportation (PennDOT) identified issues when using Pavement ME regarding overprediction of faulting for some design parameters, especially for concrete with high levels of coefficient of thermal expansion (CTE). Underprediction was identified when designing widened lanes.

PennDOT also observed faulting as a distress that develops in Bonded Concrete Overlays on Asphalt (BCOA). Currently, faulting is not accounted for in the design procedures for BCOA. Even though faulting in BCOAs present similarities to faulting in JPCP, the pumping mechanism for the BCOA is dictated by the depth of joint propagation. This means that pumping can develop at either the bottom of the overlay slab within the asphalt layer or below the asphalt in the granular layer. In addition, JPCPs are typically thicker ( $> 8$  in) than a BCOA ( $\leq 6$  in) and have longer joint spacings (conventional joint spacings are 15 – 20 ft) than BCOAs (typically 6 – 12 ft). Therefore, in accordance with good practices for proper design, the mechanistic-empirical design for BCOA (BCOA-ME) should have its own faulting model that accounts for these particular characteristics, and that is calibrated and validated with BCOA data.

Concerning these issues with the faulting modeling for JPCP and BCOA, the research project was divided into four main tasks. Chapters 1 and 2 regard the review and improvement of the current Pavement ME faulting model for JPCP. The focus of Chapter 3 is on the development of a faulting model unique for BCOA and the incorporation of this model into the BCOA-ME.

## **2 CHAPTER 1: EVALUATION OF THE FAULTING MODEL FOR PENNSYLVANIA CONDITIONS**

The main objective of this chapter is to provide information and field data to perform model improvements in the next steps of the project. This chapter presents an evaluation of the AASHTOWare Pavement ME transverse joint faulting model for jointed plain concrete pavements (JPCP, developed from the Mechanistic-Empirical Pavement Design Guide (MEPDG) [1], regarding Pennsylvania field data. First, a literature review on the most known available faulting models is presented. Transverse joint faulting data was collected from the Long-Term Pavement Performance (LTPP) program database for Pennsylvania and neighboring states and from PennDOT road management system (RMS). A statistical analysis was performed for the PennDOT RMS data and results were compared to Pavement ME faulting predictions. Results clearly indicate a need for a recalibration of the Pavement ME faulting model regarding Pennsylvania conditions.

### **2.1 Literature Review of Faulting Models**

Joint and crack faulting is a major distress in jointed concrete pavements that results in a loss of serviceability. Faulting is the differential vertical displacement of the slab edge across a transverse joint. Faulting is developed when excessive corner deflections at the joint lead to erosion and migration of fines from beneath the slab. Fines' deposition under the approach slab corner causes the approach slab to rise. Faulting is developing under the following conditions [2]:

- Heavy axle load applications;
- Presence of erodible base and subgrade;
- Highly saturated base and subgrade;
- Poor load transfer.

Significant faulting impacts the life cycle cost of the pavement through early rehabilitation and vehicle operating costs. Performance related faulting models that follow the pavement design guide can be used to predict and analyze faulting distress in a concrete pavement. There are currently several mechanistic-empirical faulting models that simulate future distress in pavements, each with their own advantages and limitations.

#### **2.1.1 Mechanistic-Empirical Faulting Models**

##### *2.1.1.1 FHWA PAVESPEC 3.0 Faulting Model*

One of the first mechanistic-empirical faulting models was developed under the FHWA-sponsored study and implemented in the PAVESPEC 3.0 software. The faulting model is based on the differential energy of subgrade deformation [3]. The FHWA PAVESPEC 3.0 faulting model relates differential energy of subgrade deformation to faulting development. Differential energy is a generalization of the concept of deformation energy that had been used to simulate pumping in concrete pavements due to traffic loading [4-6]. The relationship between the density of subgrade elastic deformation, the PCC slab corner deflection, and the coefficient of subgrade has the following form:

$$E = \frac{k\delta^2}{2} \quad (1)$$

where:

$E$  is the density of elastic deformation which means the energy of subgrade deformation of a unit subgrade surface area;  
 $\delta$  is the slab's deflection;  
 $k$  is the modulus of subgrade reaction.

The differential energy of subgrade deformation is defined as the energy difference in the elastic subgrade deformation under the leave slab (loaded) and approach slab (unloaded):

$$DE = E_L - E_{UL} = \frac{k\delta_L^2}{2} - \frac{k\delta_{UL}^2}{2} \quad (2)$$

where:

$DE$  is differential energy of subgrade deformation;  
 $E_L$  is energy of subgrade deformation under the loaded slab corner;  
 $E_{UL}$  is energy of subgrade deformation under the unloaded slab corner;  
 $\delta_L$  is the corner deflection under the loaded slab;  
 $\delta_{UL}$  is the corner deflection under the unload slab.

Equation 2 can be re-written in the following form (Equation 3):

$$DE = E_L - E_{UL} = \frac{k}{2}(\delta_L - \delta_{UL})(\delta_L + \delta_{UL}) \quad (3)$$

The term  $(\delta_L + \delta_{UL})$  is equal to the free corner deflection while the term  $(\delta_L - \delta_{UL})$  is the differential corner deflection between loaded and unload slabs. The former characterizes total flexibility of the slab and the latter quantifies relative vertical movement between the loaded and unloaded sides of the joint. Higher slabs' flexibility and differential differences increase the differential energy and joint faulting potential. The differential corner deflection depends on free corner deflection and deflection load transfer efficiency (LTE) defined as:

$$LTE = \frac{\delta_{UL}}{\delta_L} 100\% \quad (4)$$

The differential energy can be expressed as a function of joint LTE:

$$DE = \frac{k}{2}(\delta_L + \delta_{UL}) \frac{1 - \frac{LTE}{100}}{1 + \frac{LTE}{100}} \quad (5)$$

PAVESPEC 3.0 accounts for several parameters in the faulting prediction such as traffic volume, dowel diameter, Portland cement concrete (PCC) slab and base properties, subgrade support, and climatic conditions. Nonetheless, the model presents significant limitations. It assumes that pavement properties do not vary over time. It disregards seasonal and environmental effects on faulting development and does not take into account joint LTE deterioration as well as change in PCC slab stiffness over time. This drawback is addressed in the MEPDG faulting model.

### 2.1.1.2 MEPDG Faulting Model

The Mechanistic-Empirical Pavement Design Guide (MEPDG) faulting model implemented in the AASHTOWare Pavement ME software is an improvement of the FHWA PAVESPEC 3.0 faulting model. Pavement ME faulting model uses a monthly incremental approach [3]. This model also uses differential energy of subgrade deformation to predict faulting, but dowel damage, loss of shear capacity, and faulting increments are calculated at the end of every month and summed for the cumulative faulting for the life of the pavement.

Joint deterioration reduces joint LTE, increases the magnitude of differential PCC slab deflection across the joint increasing the magnitude of differential energy of subgrade deformation for the same traffic level and faulting development.

For transverse joints, the total deflection LTE includes the contribution of three major mechanisms of load transfer: (1) by PCC aggregates, (2) by joint dowels (if used), and (3) by base/subgrade. The combined LTE can be determined with Equation 6:

$$LTE_{joint} = 100 \left( 1 - (1 - LTE_{dowel} / 100)(1 - LTE_{agg} / 100)(1 - LTE_{base} / 100) \right) \quad (6)$$

where:

$LTE_{joint}$  is total joint LTE, percent;

$LTE_{dowel}$  is joint LTE if dowels are the only mechanism of load transfer, percent;

$LTE_{base}$  is joint LTE if the base is the only mechanism of load transfer, percent;

$LTE_{agg}$  is joint LTE if aggregate interlock is the only mechanism of load transfer, percent.

### Aggregate Interlock Joint Load Transfer

The Zollinger et al. aggregate interlock model was adapted for the MEPDG faulting predictions [7]. This model relates the non-dimensional stiffness of an aggregate joint with the load shear capacity, S.

$$\text{Log}(J_{AGG}) = -3.19626 + 16.09737 * e^{-e^{-\left(\frac{S-e}{f}\right)}} \quad (7)$$

where:

$J_{AGG}$  (Agg/kl) is joint stiffness of the transverse joint for current increment;

e is constant equal to 0.35;

f is constant equal to 0.38;

S is joint shear capacity.

The joint shear capacity depends on the joint width and past damage and is defined as follows:

$$S = 0.05 * h_{PCC} * e^{-0.028jw} - \Delta S_{tot}^b \quad (8)$$

where:

$S$  is dimensionless aggregate joint shear capacity;

$jw$  is joint opening, mils (0.001 in);

$h_{pcc}$  is PCC slab thickness, in;

$\Delta s_{tot}^b$  is cumulative loss of shear capacity at the beginning of the current month equal to sum of loss of shear capacity from every axle load application.

The MEPDG faulting mode computes joint width for each month based on PCC zero-stress temperature, PCC shrinkage, and PCC mean nighttime monthly temperature using Equation 9:

$$jw = \text{Max}(12000 * JTSpace * \beta * (\alpha_{PCC} * (T_{constr} - T_{mean}) + \varepsilon_{sh,mean}), 0) \quad (9)$$

where:

$\varepsilon_{sh,mean}$  is PCC slab mean shrinkage strain;

$\alpha_{PCC}$  is PCC coefficient of thermal expansion, in/in/ $^{\circ}\text{F}$ ;

$JTSpace$  is joint spacing, ft;

$\beta$  is joint open/close coefficient assumed equal to 0.85 for a stabilized base and 0.65 for an unbound granular base;

$T_{mean}$  is mean monthly nighttime mid-depth temperature,  $^{\circ}\text{F}$ ;

$T_{constr}$  is PCC zero-stress temperature at set,  $^{\circ}\text{F}$ , defined as the temperature (after placement and during the curing process) at which the PCC layer exhibits zero thermal stress.

The MEPDG faulting model computes loss of joint shear capacity a monthly basis. Each axle load application contributes toward joint deterioration and the cumulative loss of shear in the beginning of the next design month is determined as follows:

$$\Delta s_{tot}^{end} = \Delta s_{tot}^b - \sum_i n_i \Delta s_i \quad (10)$$

where:

$\Delta s_{tot}^b$  is cumulative loss of shear capacity at the end of the current month equal to sum of loss of shear capacity form every axle load application.

$n_i$  is the number of applications of axle load  $i$ .

$\Delta s_i$  is loss of capacity shear due to single application of an axle load  $i$  defined as follows:

$$\Delta s_i = \begin{cases} 0 & \text{if } \frac{jw}{h_{PCC}} < 0.001 \\ \frac{0.005 * 10^{-6}}{1.0 + (jw / h_{PCC})^{-5.7}} \left( \frac{\tau_i}{\tau_{ref}} \right) & \text{if } 0.001 < \frac{jw}{h_{PCC}} < 3.8 \\ \frac{0.068 * 10^{-6}}{1.0 + 6.0 * (jw / h_{PCC} - 3)^{-1.98}} \left( \frac{\tau_i}{\tau_{ref}} \right) & \text{if } \frac{jw}{h_{PCC}} > 3.8 \end{cases} \quad (11)$$

where:

$\tau_i$  is shear stress on the transverse joint surface from the response model for the load



group i, psi;  
 $\tau_{ref}$  is reference shear stress derived from the PCA test results, psi;  
 jw is joint opening, mils;  
 $h_{PCC}$  is PCC slab thickness, in.

### Doweled Joint Load Transfer

The MEPDG faulting prediction model characterizes dowel joint stiffness using nondimensional parameters proposed by Ioannides and Korovesis [8]:

$$J_D = \frac{D}{DowelSpace k \ell} \quad (12)$$

where:

$J_D$  is non-dimensional stiffnesses of doweled joints;  
 D is shear stiffness of a single dowel (including dowel-PCC interaction), lb/in;  
 $\ell$  is the PCC slab radius of relative stiffness, in;

*DowelSpace* is the space between adjacent dowels in the wheel path, in.

The following model was adopted for non-dimensional dowel joint stiffness deterioration:

$$J_d = J_d^* + (J_0 - J_d^*) \exp(-DAM_{dowels}) \quad (13)$$

where:

$J_d$  is non-dimensional dowel stiffness;  
 $J_0$  is initial non-dimensional dowel stiffness;  
 $J_d^*$  is critical non-dimensional dowel stiffness;  
 $DAM_{dowels}$  is damage accumulated by doweled joints due to past traffic.

The initial and long-term non-dimensional doweled stiffness depend on the ratio of the area of dowel cross-section to PCC thickness as presented in Equation 14:

$$J_0 = \frac{152.8A_d}{h_{PCC}} \quad (14)$$

$$J_d^* = \begin{cases} 118, & \text{if } \frac{A_d}{h_{PCC}} > 0.656 \\ 210.0845 \frac{A_d}{h_{PCC}} - 19.8, & \text{if } 0.009615 \leq \frac{A_d}{h_{PCC}} \leq 0.656 \\ 0.4, & \text{if } \frac{A_d}{h_{PCC}} < 0.009615 \end{cases} \quad (15)$$

where:

$J_0$  is initial non-dimensional dowel stiffness;  
 $J_d^*$  is critical non-dimensional dowel stiffness;  
 $A_d$  is area of dowel cross-section:

$$A_d = \frac{\pi d^2}{4} \quad (16)$$

where:

$d$  is the dowel diameter, in;  
 $h_{pcc}$  is PCC slab thickness, in.

Dowel joint damage accumulated from an individual axle repetition is determined using the following equation:

$$\Delta DOWDAM_i = C_8 * \frac{F_{j,A}}{d f_c^*} \quad (17)$$

where:

$\Delta DOWDAM$  is dowel damage increment from an individual axle application;  
 $f_c^*$  is PCC compressive stress, psi;  
 $C_8$  is calibration constant;  
 $F$  is effective dowel shear force induced by an axle and defined as follows:

$$F = J_d * (\delta_L - \delta_U) * DowelSpace \quad (18)$$

where:

$J_d$  is non-dimensional dowel stiffness at the time of load application;  
 $\delta_L$  is deflection at the corner of the loaded slab induced by the axle;  
 $\delta_U$  is deflection at the corner of the unloaded slab induced by the axle;  
DowelSpace is the space between adjacent dowels in the wheel path, in.

### Base Load Transfer

A certain portion of load is transferred from the loaded to unloaded slab through the base, subbase, and subgrade pavement layers. In the MEPDG, this effect is considered by assigning a percentage of load transfer efficiency of the base layer,  $LTE_{base}$ , depending on the base layer type. The MEPDG assumes that a properly designed stabilized layer provides a better LTE than a granular base. In this way the procedure assumes LTE values of 20, 30, and 40% for aggregate bases, asphalt or cement treated bases, and lean concrete bases, respectively.

In colder temperatures, the aggregate portion of load transfer is lower than in warm weather because joints are more open. However, if the pavement system is frozen, the LTE of joints actually increases. It is assumed that this increase in LTE comes from the rise in base layer LTE. In order to consider this effect, the AASHTOWare Pavement ME estimates the mean monthly mid-depth PCC temperatures. Whenever a month presents this temperature below than 32 °F, the  $LTE_{base}$  is assumed to be 90% for that month.

### Faulting Accumulation Process

The incremental design procedure requires thousands of deflection calculations to compute damage monthly (for different loads, joint stiffness, and equivalent temperature differences) over

a design period of many years. This process has been implemented in the Pavement ME software. The faulting at each month is determined as a sum of faulting increments from all previous months in the pavement life using the following model [3]:

$$Fault_m = \sum_{i=1}^m \Delta Fault_i \quad (19)$$

$$\Delta Fault_i = C_{34} \times (FAULTMAX_{i-1} - Fault_{i-1})^2 \times DE_i \quad (20)$$

$$FAULTMAX_i = FAULTMAX_0 + C_7 \times \sum_{j=1}^m DE_j \times \text{Log}(1 + C_5 \times 5.0^{EROD})^{C_6} \quad (21)$$

$$FAULTMAX_0 = C_{12} \cdot \delta_{curling} \cdot \left[ \text{Log}(1 + C_5 \times 5.0^{EROD}) \times \text{Log}\left(\frac{P_{200} \text{WetDays}}{P_s}\right) \right]^{C_6} \quad (22)$$

where:

$Fault_m$  is the mean joint faulting at the end of month  $m$ , in.;

$\Delta Fault_i$  is the incremental change (monthly) in mean transverse joint faulting during month  $i$ , in.;

$FAULTMAX_i$  is the maximum mean transverse joint faulting for month  $i$ , in.;

$FAULTMAX_0$  is the initial maximum mean transverse joint faulting, in.;

$EROD$  is the base/subbase erodibility factor;

$DE_i$  is the differential density of energy of subgrade deformation accumulated during month  $i$ , calculated by DE regression model;

$\delta_{curling}$  is the maximum mean monthly slab corner upward deflection PCC due to temperature curling and moisture warping;

$P_s$  is the overburden on subgrade, lb;

$P_{200}$  is the percent subgrade material passing #200 sieve;

$WetDays$  is the average annual number of wet days (greater than 0.1 in. rainfall);

$C_{1,2,3,4,5,6,7,12,34}$  are calibration constants.

The last two calibration constants,  $C_{12}$  and  $C_{34}$  can be calculated by the following equations [3]:

$$C_{12} = C_1 + C_2 \times FR^{0.25} \quad (23)$$

$$C_{34} = C_3 + C_4 \times FR^{0.25} \quad (24)$$

where:

$FR$  is the base freezing index defined as percentage of time the top base temperature is below freezing (32°F) temperature.

### 2.1.1.3 MEPDG Faulting Reliability Analysis

The faulting model process described above allows for predicting faulting at a reliability level of 50%. After 50% reliability is predicted for each year, faulting at the specified reliability level is predicted using MEPDG recommendations:

$$Fault_{Pi} = Fault_i + STD_{Fi} \cdot Z_p \quad (25)$$

where:

$Fault_{Pi}$  is the predicted faulting at the reliability level P for year  $i$ , in.;  $STD_{Fi}$  is the standard deviation of faulting at the predicted level of mean faulting for year  $i$ , in.

The AASHTOWare Pavement ME recommends the following form for the standard deviation of faulting:

$$STD_{Fi} = a \times Fault_i^b + c \quad (26)$$

#### 2.1.1.4 PittRigid-ME

PittRigid-ME is a design software created at the University of Pittsburgh. This software is primarily used for pavement design but also models cracking to predict fatigue damage and uses differential energy to predict faulting. The calculation processes for PittRigid are similar but simplified compared to Pavement ME. PittRigid-ME does not have as many input requirements, lowering potential for user error.

This model is a localized design tool specific to Pennsylvania. PittRigid-ME makes general climatic assumptions based on project location and removes certain variables that do not significantly change between projects in Pennsylvania. This allows designers to reduce the required information for a project without reducing design quality or performance prediction accuracy.

## 2.3 Pavement ME Sensitivity Analysis

A sensitivity analysis was conducted to further analyze Pavement ME faulting prediction model with respect to the effect of several design parameters regarding Pennsylvania conditions. Pavement ME faulting prediction was analyzed for different design parameters at a reliability of 90% for a case located in Pittsburgh, PA. The base for the analysis was composed of a dowelled, (1.5 in diameter) 10 in thick concrete slab (coefficient of thermal expansion set at  $5 \times 10^{-6} / ^\circ\text{F}$ ) over a permeable asphalt treated base with tied concrete shoulders subjected to an average annual daily truck traffic (AADTT) of 4000 (bidirectional). The slab geometry for the base case was 12 ft slab width with 15 ft joint spacing. Several parameters were varied based on the collected field data.

As expected, Figure 1 shows that an increase in traffic levels (AADTT) causes an increase in the predicted average faulting. For high traffic levels, the average faulting threshold of 0.15 in. is reached in approximately 19 years for an AADTT of 20,000 and in 31 years for 10,000 AADTT. For slab thickness (Figure 2), an increase in slab thickness results in a slight reduction of predicted faulting. A more significant reduction is observed when changing dowel diameter from 1.25 to 1.5 in.

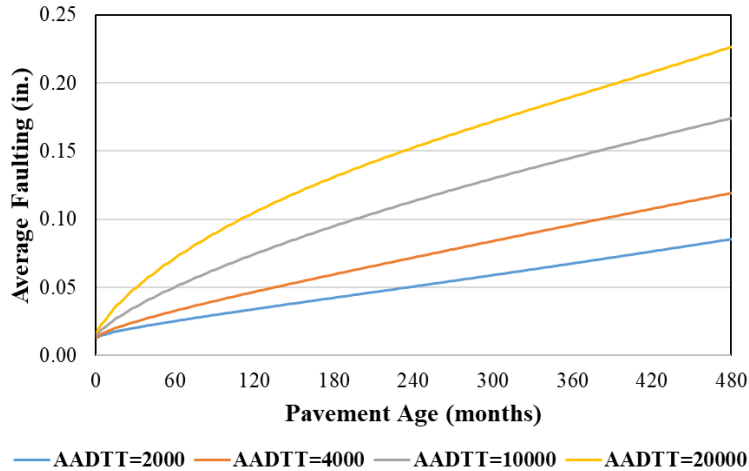


Figure 1 – Pavement ME faulting prediction for different levels of traffic

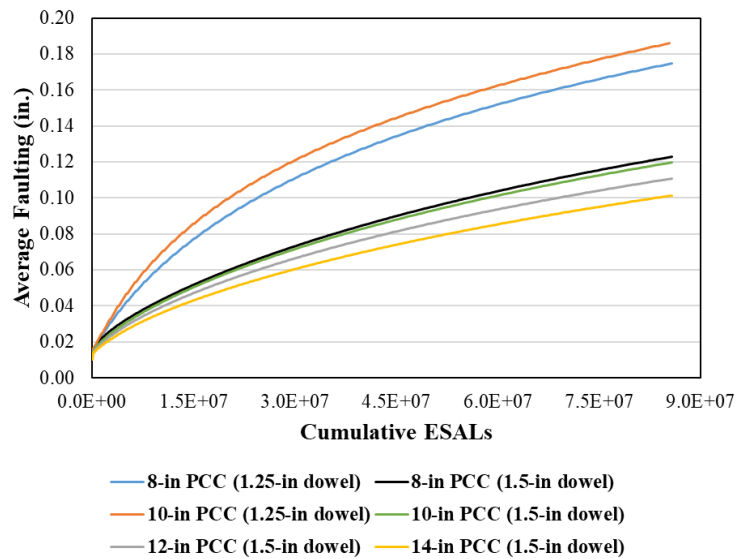


Figure 2 – Pavement ME faulting prediction for different slab thicknesses and dowel bar diameters

Again, as anticipated, an increase in the concrete coefficient of thermal expansion (CTE) results in a significant increase of predicted faulting (Figure 3). In the same way, Figure 4 indicates that higher levels of faulting are expected in pavements with larger joint spacing. Conversely, a larger dimension in the slab width decreases predicted faulting substantially (Figure 5).

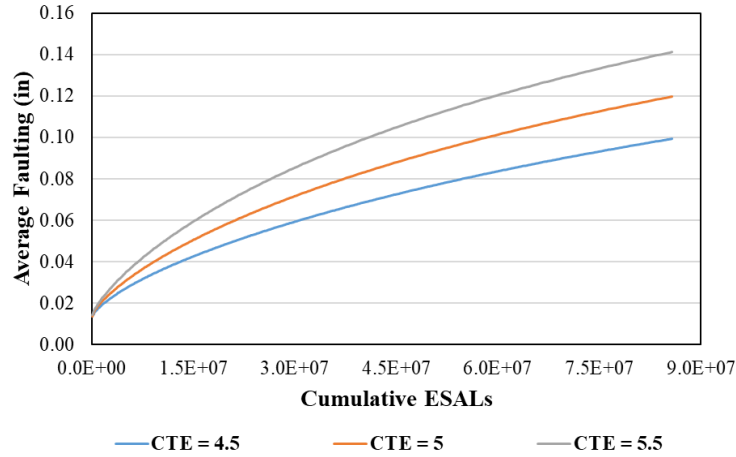


Figure 3 – Pavement ME faulting prediction for different coefficients of thermal expansion (CTE x 10<sup>-6</sup>/°F)

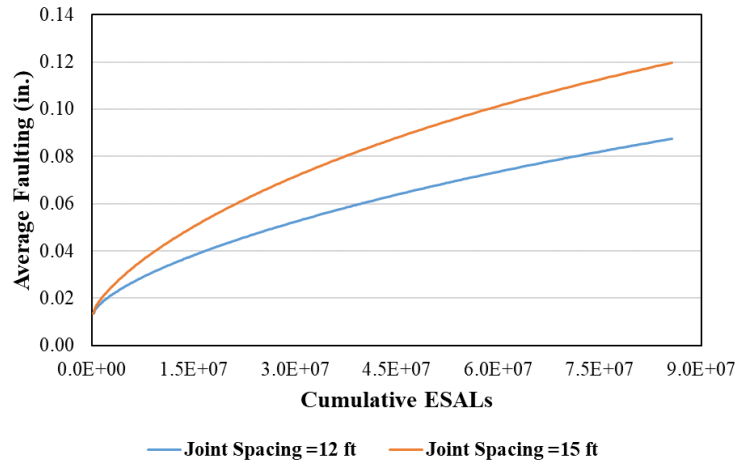


Figure 4 – Pavement ME faulting prediction for different joint spacing

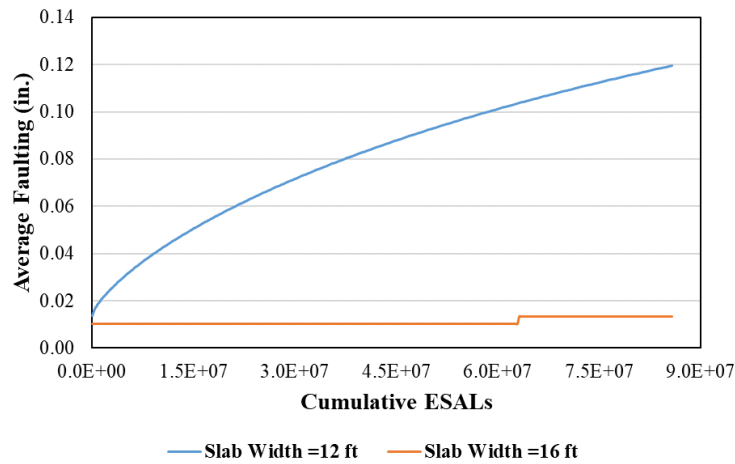


Figure 5 – Pavement ME faulting prediction for different slab widths

Figure 6 shows that the use of tied PCC shoulders showed a slight improvement in predicted faulting when compared to other non-tied shoulder types. Stabilized bases result in smaller levels of predicted faulting than unbounded aggregate bases (Figure 7). Pavement ME prediction indicates a very similar faulting performance for pavements with cement (CTPB) and asphalt (ATPB) treated permeable bases.

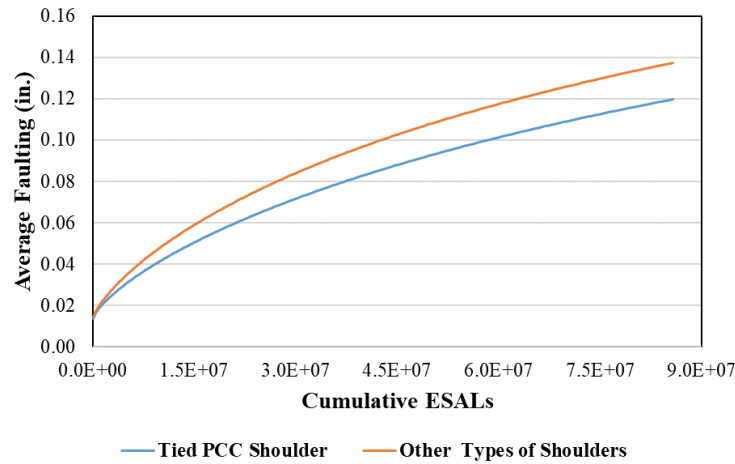


Figure 6 – Pavement ME faulting prediction for different tied PCC shoulders and other types of shoulders

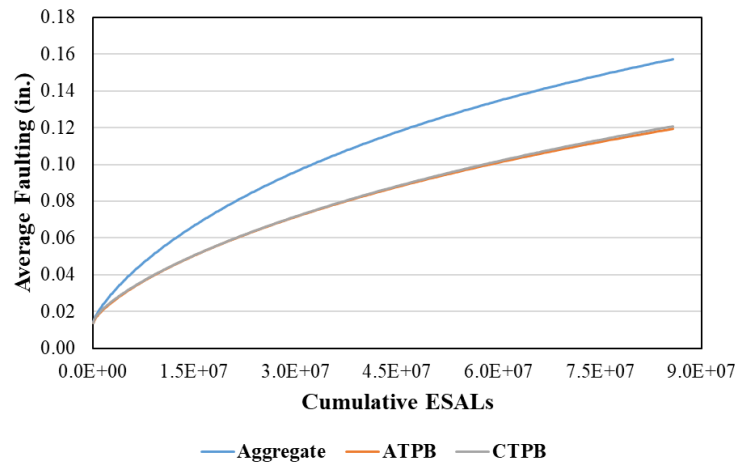


Figure 7 – Pavement ME faulting prediction for different pavement bases

## 2.4 Faulting Field Data Collection and Processing

Historical faulting data from the Long-Term Pavement Program (LTPP) for sections in Pennsylvania and Ohio were processed. Faulting data was also collected, filtered, and analyzed for PennDOT RMS National Highway System (NHS) for years 2017 and 2018.

### 2.4.1 LTPP Faulting Data

LTPP transverse joint faulting data for JPCP was collected for Pennsylvania and neighboring states. Only faulting data from original construction (construction number 1) was considered for analysis. Unfortunately, only three sections of JPCP in Pennsylvania were available on the LTPP database. From these sections, only eight historical datasets were obtained. Of the neighboring states, only Ohio had data for JPCP faulting (31 sections with 151 historical datasets). Figure 8 and Figure 9 present the LTPP faulting data preliminary analysis for Pennsylvania and Ohio, respectively.

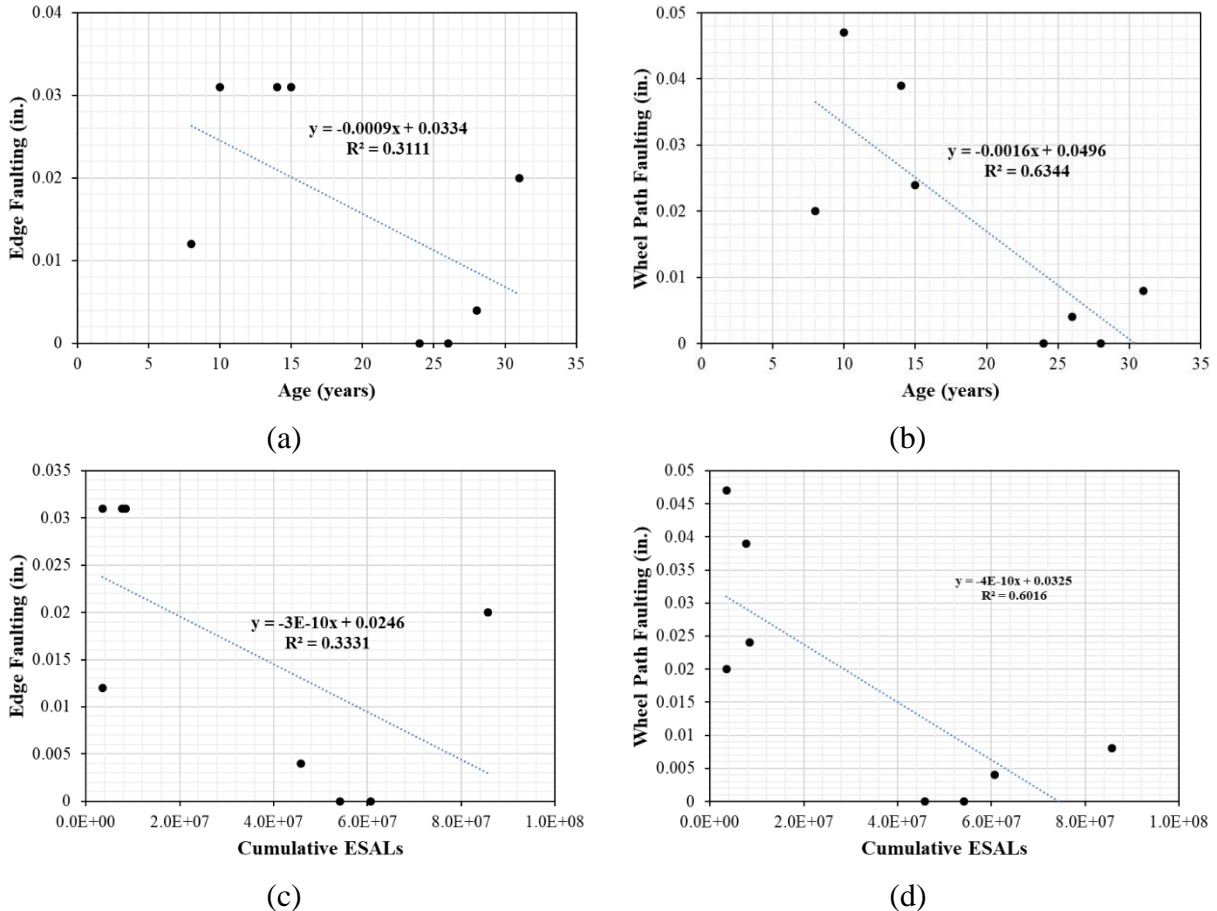


Figure 8 – LTPP edge and wheel path faulting versus pavement age (a and b) and traffic (c and d) for Pennsylvania

For Pennsylvania sections, the small number of observations led to counterintuitive results such as faulting decreasing with pavement age and cumulative traffic. For Ohio sections (greater number of observations), traffic had no apparent effect on faulting; however, pavement age presented more reliable results besides the lower correlation. It must be considered that pavements presenting high faulting were rehabilitated and therefore excluded from the analysis (change in construction) may be affecting these results.



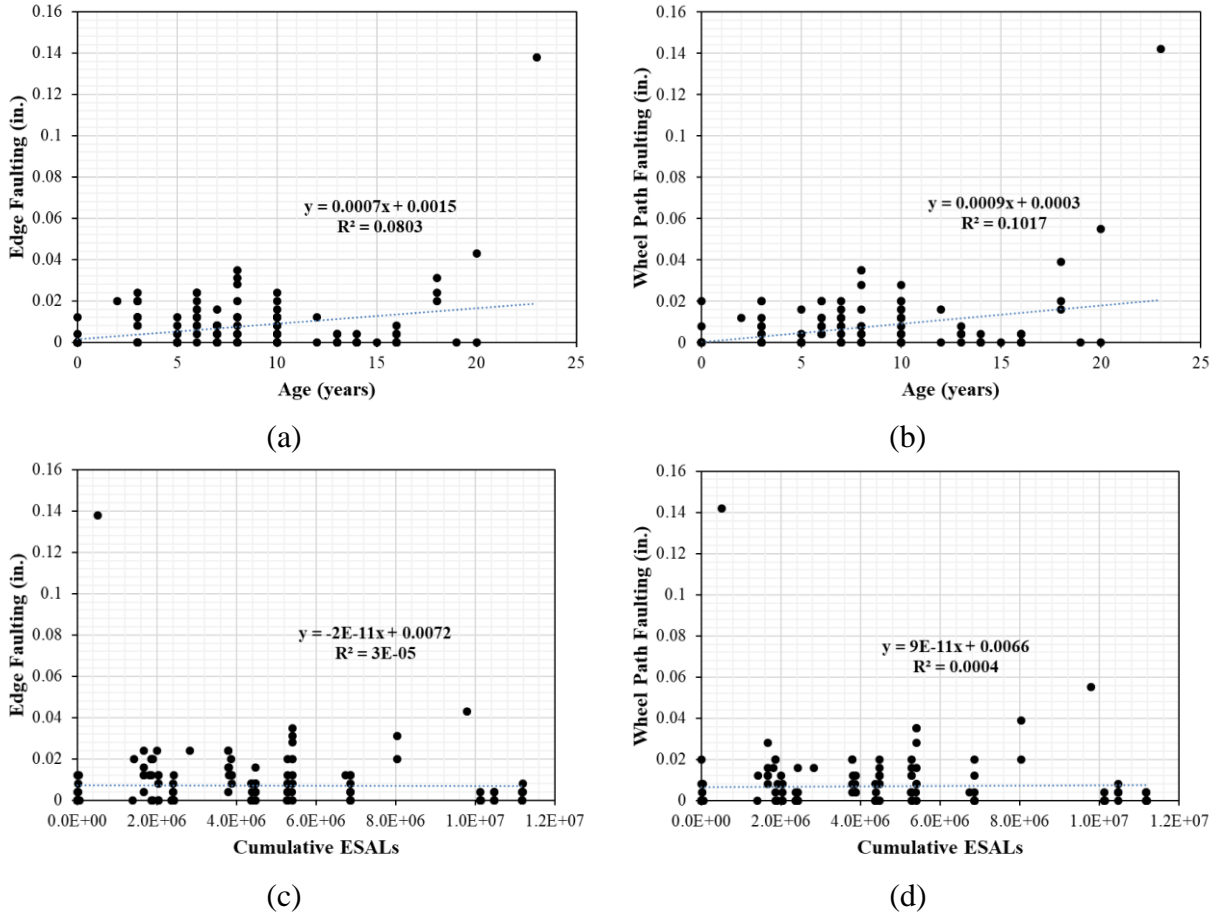


Figure 9 – LTPP edge and wheel path faulting versus pavement age (a and b) and traffic (c and d) for Ohio

Due to the small number of faulting data from the selected LTPP segments, the remaining analysis will be focused on the PennDOT RMS faulting data.

## 2.4.2 PennDOT RMS Faulting Data Processing

Over 15,000 and 20,000 Portland cement concrete (PCC) pavement condition sets of data were provided for NHS sections in years 2017 and 2018, respectively. The datasets were processed and filtered in two steps. The selection was performed to firstly eliminate irrelevant, erroneous, or missing data (step 1) and then to filter questionable data (step 2). The remaining data was used in the preliminary and statistical analysis.

### 2.4.2.1 Permanently Excluded Data

For step one, data was disregarded from further analysis based on the following criteria:

- 1) Surface Type: analysis was focused on RMS surface types 71 (jointed plain Portland cement concrete - JPCP); all other surfaces types were disregarded;
- 2) Missing Data: observations presenting no test date or distress data;
- 3) International Roughness Index (IRI): observations presenting no IRI data or code “INT”;

- 4) Transverse Joints: observations with joint count equals to zero;
- 5) Concrete Pavement Rehabilitation (CPR): segments presenting the surface layer as “CPR”;
- 6) Layer 1 (Surface) Type: plain (undowelled) and reinforced concrete surface types were disregarded from further analysis;
- 7) Layer 1 (Surface) Thickness: surface layer (PCC slab) with less than 8 in thick were eliminated;
- 8) Traffic: segments with equivalent single rigid axle (ESRL) equal to zero;
- 9) Lane Width: segments presenting lane width below 11 ft or higher than 16 ft.

#### 2.4.2.2 Questionable Data

The remaining data (after step one) was analyzed for average IRI and faulting based on a PCC pavement performance report [9]. This research analyzed common characteristics of pavement presenting good or poor performance. Average IRI and faulting were qualified based on Equations 27 and 28, respectively.

$$\text{Good Performance: } IRI < 0.631 + 0.0631 * AGE \quad (27)$$

$$\text{Poor Performance: } IRI > 1.263 + 0.0947 * AGE$$

$$\text{Good Performance: } FAULT < 2 * \left( \frac{AGE}{20} \right)^{0.25} \quad (28)$$

$$\text{Poor Performance: } FAULT > 4 * \left( \frac{AGE}{20} \right)^{0.25}$$

where:

IRI is the average International Roughness Index,

FAULT is the average joint faulting,

AGE is the number of years that the section is open to traffic.

In step two, questionable data was sequentially singled out and tentatively removed from further analysis based on the following criteria:

- 1) Performance Predictions: based on the analysis described above, observations presenting “good” IRI and “poor” faulting as well as the opposite (“poor” IRI and “good” faulting) were singled out and tentatively removed from further analysis;
- 2) Age: sections presenting ages higher than 40 years;
- 3) Surveyed Length: observation with surveyed lengths smaller than 250 ft;
- 4) Transverse Joints Spacing: data presenting unreliable joint spacing was also singled out; reliable joint spacing thresholds were set from 13 to 21 ft;
- 5) Average Rutting: observations presenting average rutting on the right or left wheel path greater than 2 in.;
- 6) Average Faulting: observations presenting excessive average faulting (greater than 0.15 in.);
- 7) Traffic: segments presenting rigid ESALs smaller than 1000;
- 8) Joint Spacing and Surface Layer: segments with contradicting information on the surface layer description regarding joint spacing and actual computed joint spacing.

The final number of datasets was over 5800 observations for both 2017 and 2018 years. Both years were combined in a single dataset by removing observations from the same segments from the 2017 dataset. This resulted in a single dataset containing over 3800 observations. Figure 10 presents the age and faulting distribution for the resulting dataset. The majority of the observations are 11 to 25 years old. The average faulting distribution shows an overall good pavement performance as around 50% of the analyzed segments present no faulting with a very small percentage presenting faulting greater than 0.04 in.

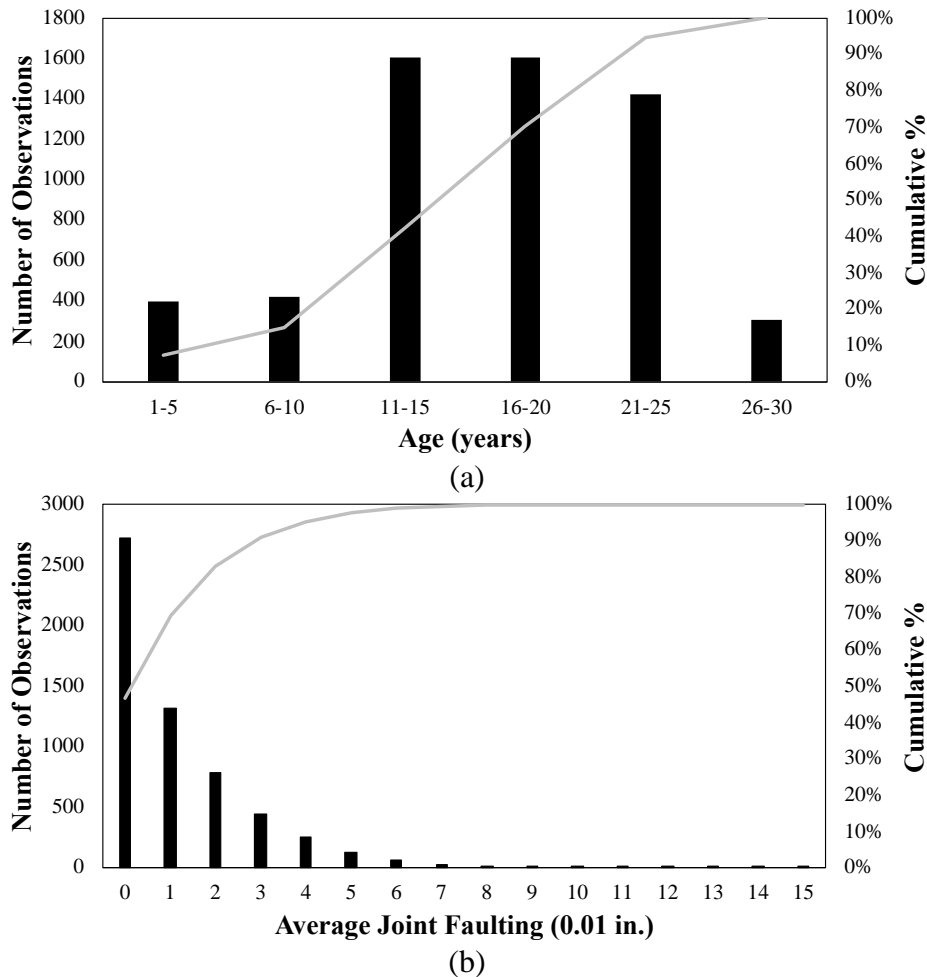


Figure 10 – Observations distribution regarding (a) pavement age and (b) average joint faulting

## 2.5 Faulting Data Statistical Analysis

For the preliminary analysis of the dataset, a basic linear regression was applied considering faulting versus pavement age, cumulative traffic, and IRI. Figure 11a presents faulting data versus age. Performance prediction lines based on the report by Khazanovich et al. (1998) are also displayed [9]. The great majority of observations are placed in the “good” performance area of the plot indicating, as mentioned before, a satisfactory performance of Pennsylvania JPCP regarding faulting. As can be seen, correlation ( $R^2$ ) between average faulting and pavement age is poor and can be explained by the large number of observations (more than half) presenting no faulting.

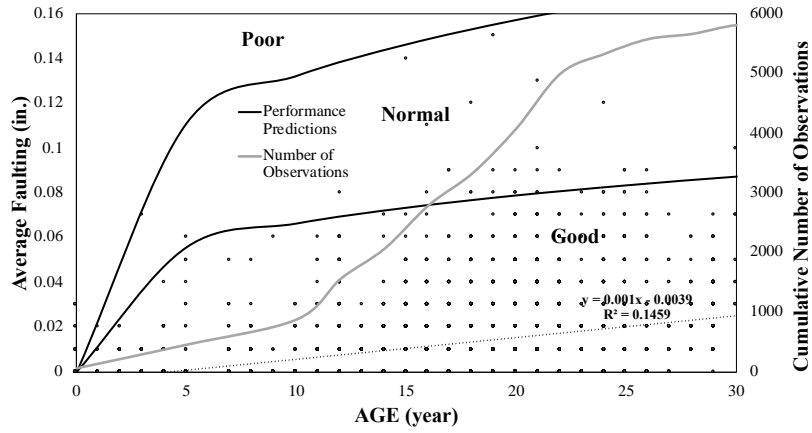
However, it must be considered that pavements presenting high faulting were rehabilitated and therefore are not included in the final dataset (survival issue). PennDOT informs that, for NHS sections, if 21 to 30% of joints present medium severity faulting, a slab stabilization with diamond grinding will be performed; if there is high severity faulting in 6 to 10 % of joints, a concrete patch rehabilitation is triggered. Only two observations in the filtered NHS datasets presented a higher than 6% number of faulted joints with high severity faulting, indicating a great possibility that sections that presented high levels of faulting were indeed rehabilitated and, consequently, excluded from the analysis according to the criteria previously described. Since the traffic data obtained from PennDOT RMS presented the ESALs for a single year (usually dating within the last 5 years), the data was backcasted to the year the pavement was opened to traffic and then forecasted to the year of the faulting survey in order to estimate cumulative traffic. A conservative compound growth of 3% was assumed for all sections. Equation 29 was used to calculate the traffic at the opening year for a given section. The same compound growth of 3% was assumed to calculate cumulative traffic at the time of the faulting survey using Equation 30.

$$ESAL_0 = \frac{ESAL_y}{(1+0.03)^{(T_y-T_0)-1}} \quad (29)$$

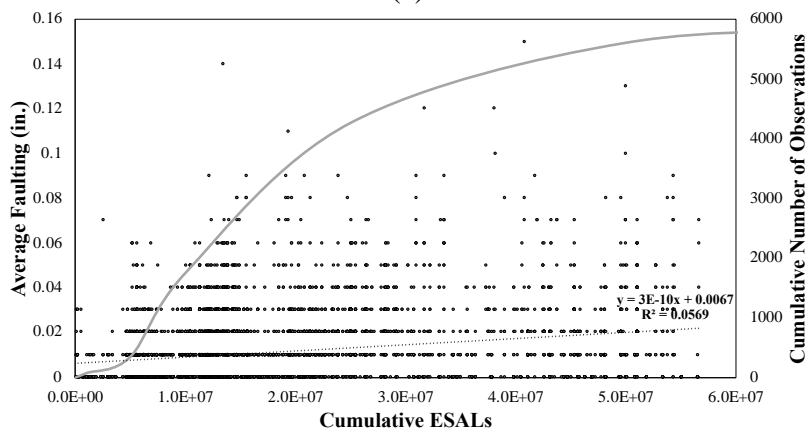
$$CESAL = ESAL_0 * \left[ \frac{(1+0.03)^{(T_y-T_0)-1}}{0.03} \right] + 0.98 * ESAL_0 * days \quad (30)$$

Where  $ESAL_0$  is the estimated annual ESALs for the first full year ( $T_0$ ) since traffic opening;  $ESAL_y$  is the annual ESALs for the last available year ( $T_y$ ) with traffic recorded; days are the number of days since traffic opening to the end of the traffic opening year, converted to a fraction of the year.

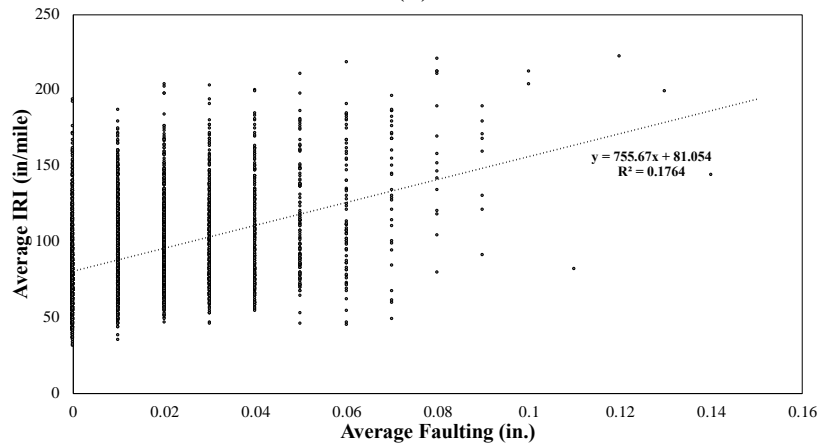
Analysis of average faulting versus cumulative ESALs (Figure 11b) also resulted in counterintuitive correlations with a range of faulting values for every traffic level. Less poor but far from satisfactory correlations are presented when comparing average faulting to average IRI (Figure 11c). Khazanovich et al. (1998) looking at LTPP sections, found an  $R^2$  of 0.42 between IRI and faulting [9]. Since joint faulting is a major indicator of a rougher pavement surface, it was expected that observations presenting IRI greater than 150 would also show some level of joint faulting. PennDOT performs diamond grinding with transverse joint seal for NHS expressways and non-expressways when IRI reaches 151 and 171, respectively. However, for every level of faulting there seems to be a varying number of IRIs going from very low to moderately high roughness.



(a)



(b)



(c)

Figure 11 – Average joint faulting versus (a) pavement age, (b) cumulative ESALs and (c) average IRI

### 2.5.1 Critical Faulting Per Traffic Level

In order to mitigate the “survival issue” effect on the analysis of RMS faulting data, an analysis of the critical faulting (top 10%) was performed. The faulting data was divided based on traffic level (Figure 12) and only segments presenting faulting higher than the 90<sup>th</sup> percentile. The updated general database contains 385 observations. Figure 13 shows the updated faulting versus cumulative traffic. The results show a much more coherent performance of joint faulting with traffic accumulation.

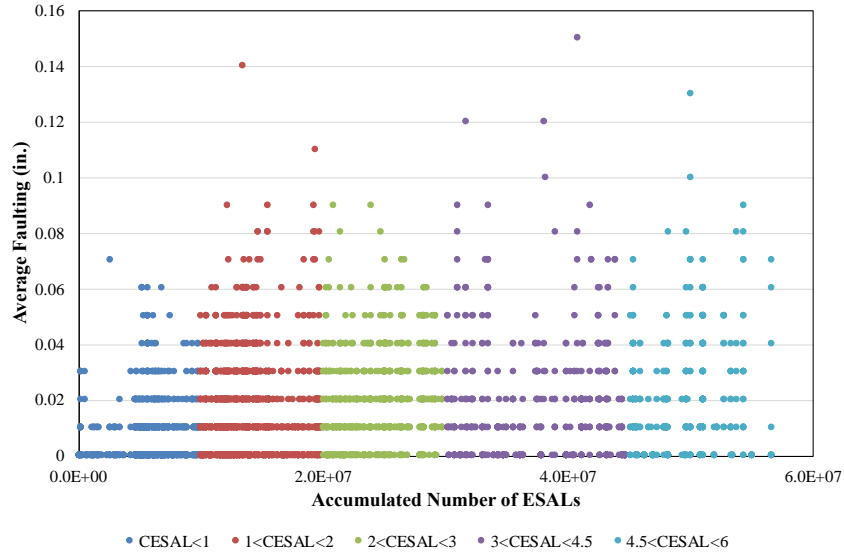


Figure 12 – Average joint faulting per traffic levels (ESAL x10<sup>7</sup>)

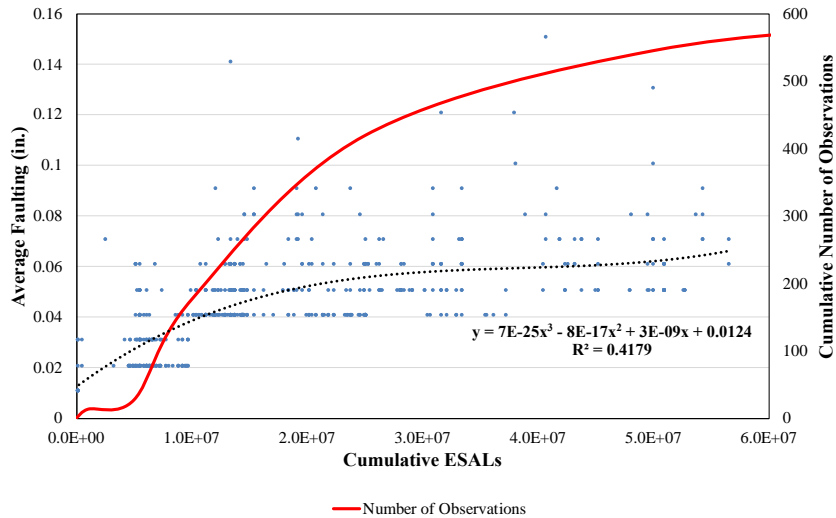


Figure 13 – Critical average faulting (90% reliability) versus cumulative traffic

The same critical faulting analysis was used to perform a comparative statistical analysis of different design parameters available in the RMS database. A faulting analysis was conducted using a series of two-sample t-tests. The purpose of the t-tests was to study whether the two-sample

means were significantly different based on a 95% confidence interval. Table 1 shows the results of the t-test.

Regarding slab geometry, joint spacing showed a significant effect on joint faulting as expected. On average, sections with greater joint spacing (20 ft) presented almost double the faulting that sections with 15 ft joint spacing. Conversely, the comparison of widened lanes with conventional lane width (12 ft) was deemed insignificant and showed counterintuitive results. It is expected smaller joint faulting in section with wider lanes. However, the small number of observations with wider lanes (only eight with critical faulting values per traffic level) is assumed to be the cause for the unreasonable results.

The effect of tied PCC shoulders in comparison with other types of shoulders was also not significant – even though the P-value was close to the 0.05 threshold. Again, the difference in the number of observations might be the cause for this result. For base types, treated bases (asphalt or cement) showed significantly less faulting than aggregate bases, as expected. When comparing both types of base stabilization, differently from the Pavement ME sensitivity analysis, asphalt treated bases showed a slight, but statistically significant, increase in performance.

The results of a study based on LTPP faulting corroborate these findings for joint spacing, shoulder type, and base types (treated versus aggregate). However, for lane width, the LTPP report found a significant effect of wider lanes on reducing joint faulting [10].

Table 1 – Statistical comparison between design features effect on critical joint faulting

Feature 1				Feature 2				Comparison		
Feature	N° Obsv.	Mean	STD	Feature	N° Obsv.	Mean	STD	One-Tail P-Value	Feature 2/1	Significant ?
Joint Spacing (15 ft)	190	0.026	0.017	Joint Spacing (20 ft)	199	0.049	0.016	0.0000	1.91	Yes
Widened Lane	6	0.045	0.018	Slab Width (12 ft.)	348	0.039	0.038	0.3556	0.86	No
Shoulder (Tied PCC)	328	0.039	0.018	Shoulder (Other)	61	0.044	0.023	0.0614	1.13	No
Base Type (Asphalt)	224	0.027	0.016	Base Type (Aggregate)	111	0.053	0.017	0.0000	1.95	Yes
Base Type (Cement)	57	0.035	0.017	Base Type (Aggregate)	111	0.053	0.017	0.0000	1.51	Yes
Base (Asphalt)	224	0.027	0.016	Base Type (Cement)	57	0.035	0.017	0.0011	1.29	Yes

## 2.6 Evaluation of Pavement ME Faulting Model Based on Pennsylvania Field Data

With the purpose to verify the accuracy of the Pavement ME faulting model in relation to PennDOT RMS data, two general example cases were developed using the top 10% faulting analysis described previously. Field data for the two cases were filtered based primarily on joint spacing. The remaining parameters were selected based on the number of observations available regarding joint spacing. Due to significant changes in predicted performance (small faulting) from sections presented in Erie County (District 1), observations from this area were not considered in this part of the analysis. Table 2 presents the main inputs from the Pavement ME faulting model for both cases. For both thicknesses and AADTT, the values represent the average results from the field data (top 10% faulting per traffic level) for each case.

Table 2 – Input parameters for Pavement ME faulting prediction

Parameter	Case 1		Case 2	
	Field Range	Pavement ME Input	Field Range	Pavement ME Input
PCC Thickness (in.)	9 - 12	10.80	10 - 13	10.9
Two-way AADTT (year 1)	900 - 4500	1900	1000 - 6600	2400
Joint Spacing (ft.)	15	15	20	20
Dowel Diameter	1.5	1.5	1.5	1.5
Slab Width (ft.)	12	12	12	12
Shoulder Type	Tied PCC	Tied PCC	Tied PCC	Tied PCC
CTE ( $10^{-6}$ /°F)	NA	4.5, 5.0, 5.5	NA	4.5, 5.0, 5.5
Base Type	Treated Base	Treated Base	Untreated Base	Untreated Base

### 2.6.1 General Case 1: Joint Spacing 15 ft.

Figure 14 presents the results for General Case 1. The selection process resulted in 214 observations with the design parameters established in Table 2. Since the field data showed in Figure 14 represents the highest faulting level (10%), results show that Pavement ME overpredicts faulting at a 90% reliability for all CTEs. Unfortunately, the traffic level experienced by these observations reaches only to approximately 20 million ESALs (around 13 million trucks). Observations for General Case 1 that surpass this traffic level present two main differences from the average data presented in Table 2, namely, the AADTT (average 9400) and concrete slab thickness (15 in.). Regarding this, a sub-case of General Case 1 (Sub-Case 1) was developed for these observations (18 total) and results are shown in Figure 15. For high traffic levels, results show a greater overprediction of average faulting.



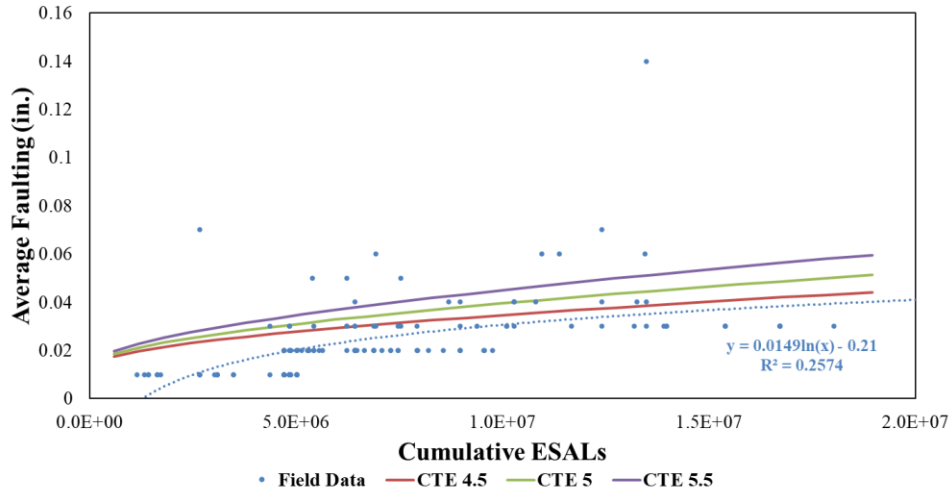


Figure 14 – Pavement ME faulting prediction versus field data: General Case 1

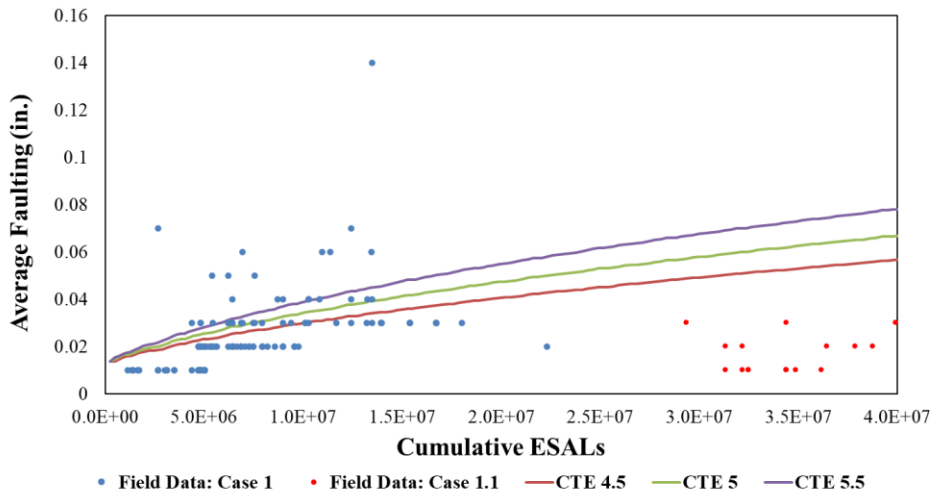


Figure 15 – Pavement ME faulting prediction versus field data: Sub-Case 1

### 2.6.2 General Case 2: Joint Spacing 20 ft.

For Case General 2, 221 field observations were selected, covering a more comprehensive traffic range (Figure 16). This time, the overprediction by Pavement ME is much more evident. The prediction results clearly do not capture the field performance.

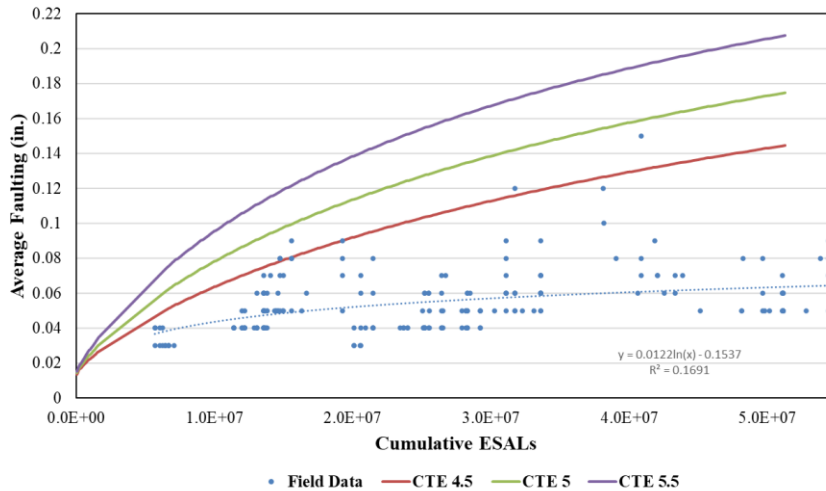


Figure 16 – Pavement ME faulting prediction versus field data: General Case 2

### 2.6.3 Comparison of Pavement ME Faulting Model with Other Models Regarding Field Data

Other versions of the Pavement ME faulting model were compared to the field data. Table 3 presents model coefficients resulting from previous calibrations. The models considered were:

- NCHRP 1-40D [11]
- NCHRP 20-07 [12]
- PennDOT local calibration [13]

Under the NCHRP 1-40D effort, the faulting model was re-calibrated using MEPDG v 0.9 software resulting in calibration coefficients similar to the original version. The remaining versions of the MEPDG software, including version 1.1, and early versions of Pavement ME use the coefficients estimated under the NCHRP 1-40D study.

Table 3 – Faulting coefficients from previous Pavement ME calibrations

	<b>NCHRP 01-40D</b>	<b>NCHRP 20-07</b>	<b>ARA/PennDOT</b>
C1	1.0184	0.595	0.595
C2	0.9165	1.636	1.636
C3	0.002185	0.00217	0.00147
C4	0.000884	0.00444	0.00444
C5	250	250	250
C6	0.4	0.47	0.4
C7	1.83312	7.3	7.3

For the NCHRP 20-07 study, the model was recalibrated using the Pavement ME version 2.21.24 software using a significantly different calibration database than the one used for the previous versions. This version was used to perform the sensitivity analysis presented in Section 3 of this chapter. The latest calibration of the Pavement ME procedure for PennDOT considering

Pennsylvania conditions was conducted by ARA, Inc resulting in calibration coefficients similar to the ones of NCHRP 20-07.

Figure 17 shows the comparison between the versions of the Pavement ME faulting model with the field data. General Case 1 input parameters were used for the models. All models overpredict average faulting, especially for the latest calibrations. The results indicate that it is possible to recalibrate the model to be more representative of the critical faulting per traffic level found in the field.

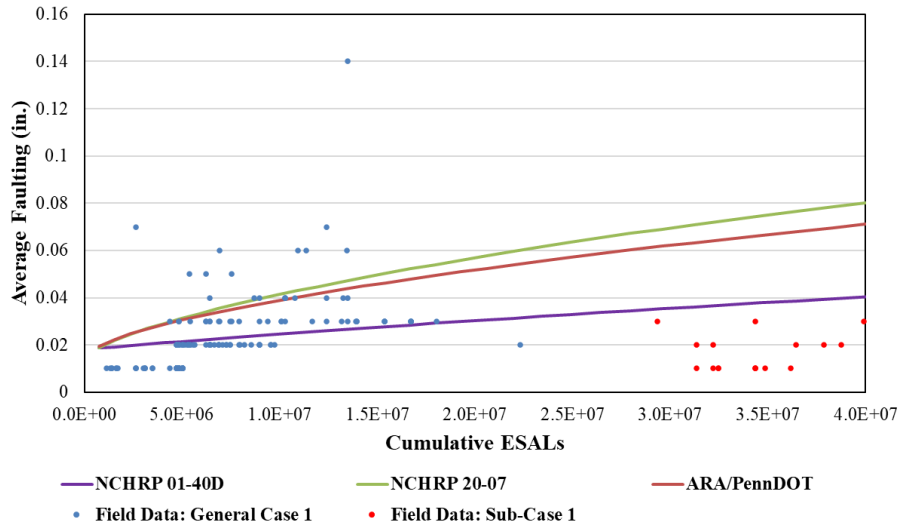


Figure 17 – Comparison of different versions of faulting models

### 3 CHAPTER 2: JPCP FAULTING MODEL IMPROVEMENT

This chapter presents the activities performed under the second task of the project entitled “Faulting Model Improvements for MEPDG”. The main objective of this task was to evaluate the current Pavement ME faulting model and, if necessary, recommend modifications.

The Mechanistic–Empirical Pavement Design Guide (MEPDG) recommends the following procedure for the evaluation and improvement of pavement performance models in two stages:

Stage 1. Comparison of performance predictions for 50% reliability with a small set of high-quality pavement performance data and, if necessary, recalibration or modification of the performance prediction model.

Stage 2. Updating the reliability model to account for discrepancies between the model predictions and the observed pavement performance.

Although this approach has been successfully implemented by several state transportation agencies, it has several drawbacks, including the following:

1. It requires high-quality information on the pavement design inputs, traffic characterization, etc.
2. Most of the efforts are devoted to improvement of performance predictions with 50% reliability.
3. Improvement of the reliability model requires a larger pavement performance database. However, even a comprehensive pavement performance database is biased toward either relatively young sections or older sections exhibiting better than average performance. Older sections with poor performance may be rehabilitated and their performance information may be unavailable. Therefore, the traditional approach may not improve predictions for higher (90-95%) reliability levels.

In this study, we proposed an alternative approach:

- First, the MEPDG faulting reliability model was evaluated using the PennDOT Roadway Management System (RMS) pavement performance data. A novel approach for modification, preliminary calibration, and validation of the reliability model was proposed. This approach accounts for lack of performance data for the rehabilitated sections. Based on the modified reliability analysis, recommendations for improvement of the faulting model were proposed.
- Second, the faulting model was modified based on recommendations from the modified reliability analysis. The modified model was validated, and a broad sensitivity analysis was presented. The effect of high levels of coefficient of thermal expansion (COTE) and widened lanes on faulting prediction the proposed modified model was compared with the current Pavement ME model predictions.
- Several design examples accounting for both cracking and faulting performance requirements were considered. It was demonstrated that the use of the modified faulting model leads to more realistic performance predictions.

### 3.1 Modification of the Faulting Reliability Model

This section describes a step-by step process for the modification of the faulting reliability model using RMS data. The MEPDG reliability procedure was modified to consider potential rehabilitated observations with an adaptation of the approach introduced by Darter *et al.* (2005) [14]. The validation of the RMS calibrated reliability model was conducted with field data with considerations on how to include rehabilitated sections into the validation process as well.

#### 3.1.1 Pavement ME Reliability Faulting Model

Reliability analysis is an important part of the MEPDG [14]. Design reliability (R) is defined as the probability (P) that each distress or ride quality will be less than a selected threshold over the design life. For faulting, design reliability is expressed as:

$$R = P(\mu F < C\mu F) \tag{31}$$

where:

- $\mu F$  is the mean joint faulting,
- $C\mu F$  is the critical mean joint faulting.

The faulting model predicts faulting at a reliability level of 50%. Faulting at a specified reliability level is predicted using the following equation:

$$Fault_{Ri} = Fault_i + STD_{Fi} \cdot Z_R \tag{32}$$

where:

- $Fault_{Ri}$  is the predicted faulting at the reliability level R for year i;
- $STD_{Fi}$  is the faulting standard deviation at the predicted level of mean faulting for year i;
- $Z_R$  is the standard normal deviate for reliability level R;
- $Fault_i$  is the predicted faulting at 50% reliability for year i.

Pavement ME recommends the following form for the standard deviation of faulting:

$$STD_{Fi} = a \times Fault_i^b + c \tag{33}$$

where a, b and c are calibration coefficients.

A compilation of Pavement ME faulting calibrations revealed that, of the seven states that performed JPCP calibrations, five (Iowa, Louisiana, Missouri, Ohio, and Washington) adopted the national calibration standard deviation coefficients [15]. Only Arizona and Colorado proposed different coefficients. The faulting model calibration performed for Pennsylvania also slightly modified the reliability coefficients as seen in Table 4.

Table 4 - National and State calibrated coefficients for faulting reliability model

	<b>NCHRP 20-07</b>	<b>PA</b>	<b>CO</b>	<b>AZ</b>
a	0.07162	0.08162	0.0831	0.037
b	0.368	0.3481	0.3426	0.6532
c	0.00806	0.008	0.00521	0.001

Figure 18 exemplifies the effect of various reliability models on faulting prediction. Using a single faulting model, NCHRP 20-07, but changing the reliability model alters the faulting predictions. PA and CO reliability model yield results similar to the NCHRP 20-07 model predictions. For these reliability models, as seen in Table 4, modifications to coefficients a, b, and c were minimal. Simulations using the AZ reliability model presented rather different coefficients in comparison with NCHRP 20-07. This resulted in much less conservative faulting predictions extending the design life (considering a 0.15 in faulting threshold) over an additional 10 years in comparison with the other models.

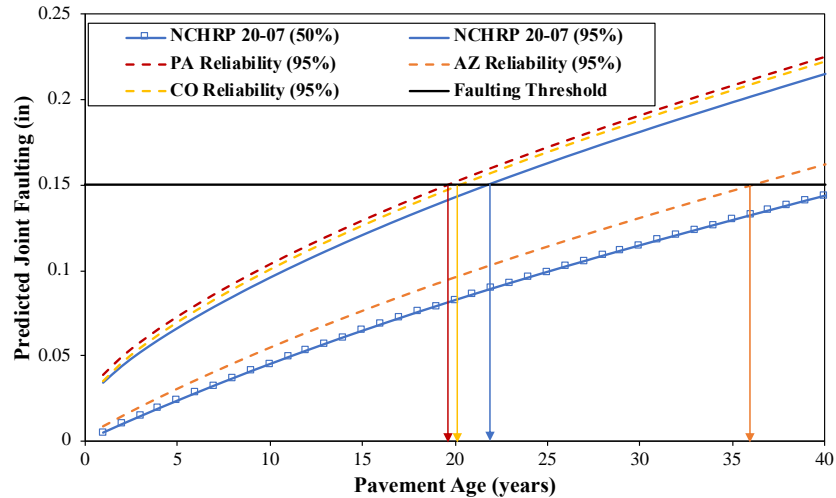


Figure 18 – Faulting predictions using a single model with different reliability models

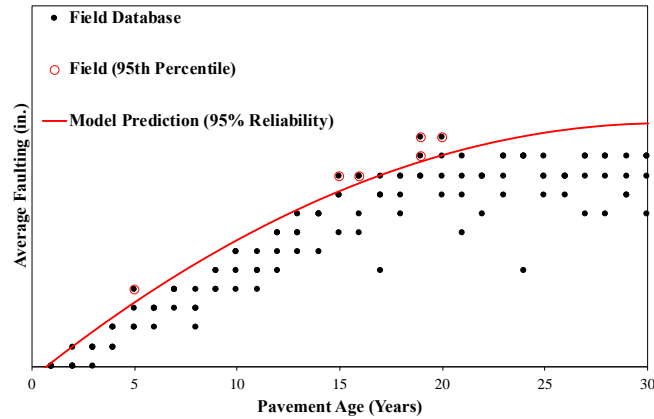
### 3.1.2 The “Survivals” Issue: Potential Rehabilitated Sections in the Faulting Database

The so-called “survival issue” aspect of field databases for full or partial model calibration and validation is usually ignored. Pavement model calibration and, subsequent validation, explores field data for a specific pavement design usually interested in age, traffic, and performance indicators (distress levels).

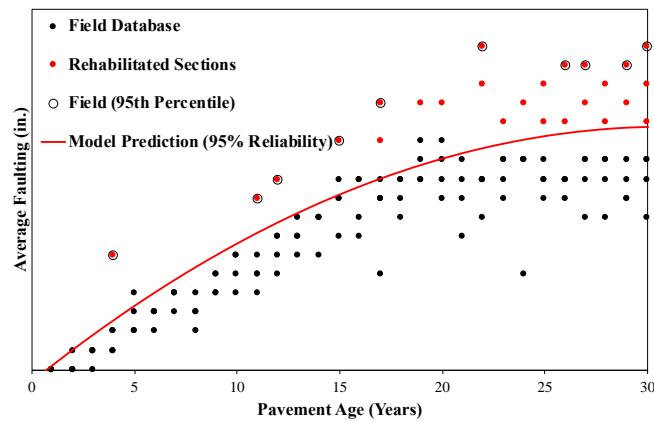
It is anticipated that the faulting database for the same design features would show an increase in the distress indicator (average faulting) for older sections that experienced more traffic as illustrated in Figure 19a. In this hypothetical case, the faulting model predictions seem to capture the field performance reasonably well; only 5% of the sections presents faulting higher than the 95% reliability prediction.

However, because poorly performing sections get rehabilitated when performance reaches critical level, their performance if they stay in service without rehabilitation is not available. Due to this a portion of observations with high faulting levels are left out of the calibration and validation processes. If these rehabilitated sections could be considered in the hypothetical validation case, the model calibrated based on the performance information for the in-service sections would be classified as underpredicting as illustrated in Figure 19b.

This problem of calibrating performance models using the information from the “surviving” sections has even greater effect when predictions should be made with a high reliability level. Even a small percentage of the removed due to rehabilitation or reconstruction sections would significantly affect the actual reliability level of performance prediction for a high distress level.



(a)



(b)

Figure 19 – Hypothetical performance model validation (a) using conventional field data collection, and (b) considering rehabilitated sections

To evaluate the extent of this problem, a database composed of layer information for most of PA JPCP was analysed to detect percentages of rehabilitated sections. Rehabilitated sections were identified by having one or more layers with a rehabilitation indicative title, like, CPR, diamond grinding, asphalt rehabilitation, surface treatments, etc., and a JPCP layer at some point of the sections’ existence. Information on why these particular sections were rehabilitated was unavailable.

Figure 20 shows the percentage of rehabilitated sections divided by pavement age. For pavements aged up to 15 years old, a small percentage of sections required rehabilitation measures. For pavements up to 25 years old, about a quarter of the sections are rehabilitated. For older pavements (age greater than 25 years old), the majority (60%) of sections receive some sort of rehabilitation. The same analysis was conducted for the RMS faulting database resulting in similar numbers. This

analysis indicates that for sections older than 15 years, there is a considerable number of rehabilitated sections that would generally be overlooked by model calibrations and validations.

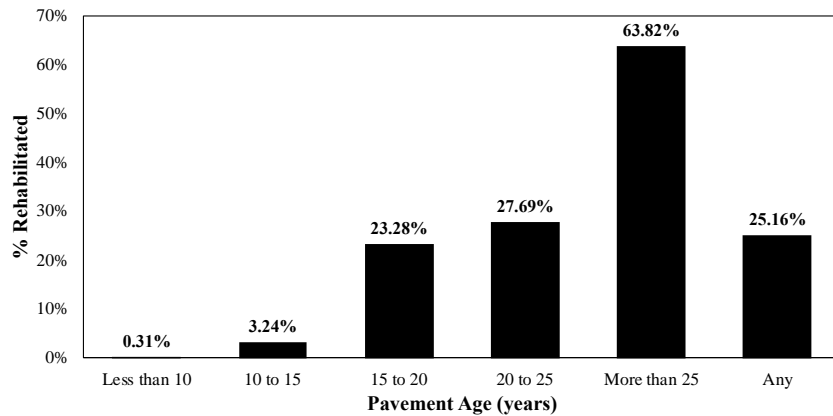


Figure 20 – PA JPCP rehabilitation probability in relation to pavement age

### 3.1.3 Step-by-Step Procedure for RMS Calibrated Reliability Model Considering Potential Rehabilitated Observations

Faulting performance with 50% reliability was simulated for the pavement sections using the design parameters reported in the PennDOT RMS database using Pavement ME software version 2.3.1 with the default inputs and calibration parameters recommended by ARA, Inc. [13]. PennDOT provided concrete COTE data for a number of sections (Appendix A). Unfortunately, the COTE data was not available for every section in the database. Since the average value of the COT for the reported section was equal to  $4.97 \times 10^{-6}/^{\circ}\text{F}$ , a COTE of  $5 \times 10^{-6}/^{\circ}\text{F}$  was assumed for all Pavement ME simulations. Then, the following steps were conducted:

#### 3.1.3.1 Step 1: Database Group Arrangement

The measured/predicted faulting data were divided according to predicted faulting ranges. Table 5 shows the average joint faulting for predicted and measured faulting according to the predicted faulting range (groups). Groups were roughly selected based on the analysis of the prediction variability (measured faulting minus predicted faulting) as seen in Figure 21. For higher levels of predicted faulting (Groups G4 and G5), predicted faulting is much higher than measured faulting.

Ideally, the average predicted and average measured level of distress would be roughly the same considering a 50% reliability prediction level. Diversions from this distribution could happen due to imprecise distress predictions and/or to incomplete field databases. Results show that for the smaller faulting levels (G1 and G2), the average predicted and measured faulting are more similar, i.e., the faulting model correctly predicts faulting. With this, the discrepancy for the higher predicted faulting levels is assumed to be caused – or strongly influenced – by rehabilitated sections with higher levels of faulting missing from the faulting database.



Table 5 – Basic statistical parameters for predicted faulting groups

Group	Range of Predicted Faulting (in)		No. of Observations	Avg. Faulting (in.)	
				Predicted	Measured
G1	0	0.005	518	0.004	0.004
G2	0.005	0.015	1560	0.008	0.005
G3	0.015	0.025	410	0.019	0.014
G4	0.025	0.055	1156	0.041	0.016
G5	0.055	0.1	351	0.066	0.018

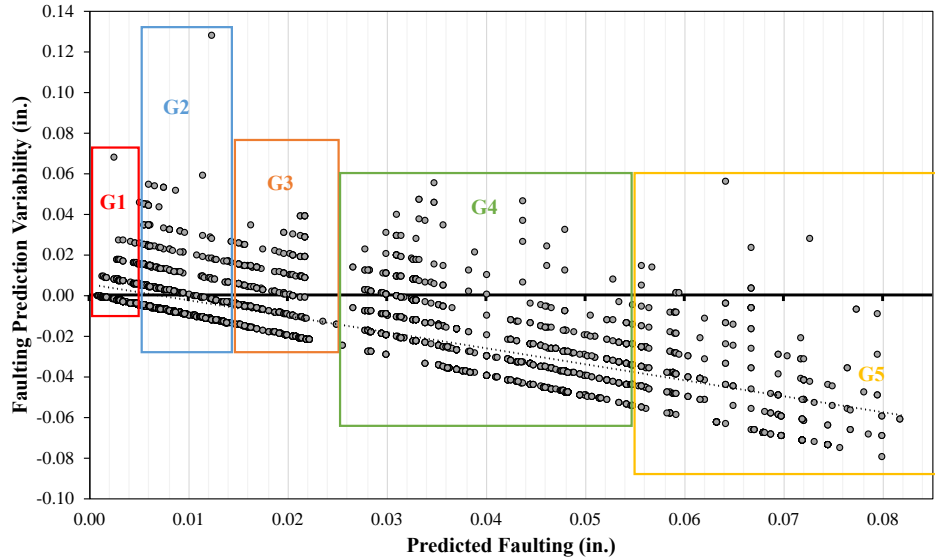


Figure 21 – Predicted faulting groups range selection

Based on the observations’ age in each group, the potential percentage of rehabilitated sections was determined (Table 6). As expected, the higher the level of faulting per group, the higher the probability of rehabilitated observations (older sections). Since there is no record of why these observations were rehabilitated and what level of faulting they had before rehabilitation, it is not possible to directly consider performance of these rehabilitated sections. However, one can assume that most of them would follow the behaviour trends exhibited by the existing “survivals” observations.

Table 6 – Probability of Potential rehabilitated observations in each group

Group	Range of Predicted Faulting (in)		No. of Observations	% Potential Rehabilitated
G1	0	0.005	518	9%
G2	0.005	0.015	1560	9%
G3	0.015	0.025	410	24%
G4	0.025	0.055	1156	39%
G5	0.055	0.1	351	44%

### 3.1.3.2 Step 2: Group Data Organization

To analyse the existing “survivals” observations behaviour, the faulting database must be rearranged regarding faulting prediction variability (measured faulting minus predicted faulting). For each group, the prediction variability was related to the standard normal deviate. Predicted and measured faulting data were filtered based on faulting variability for each group. The resulting database was assigned a proportional index based on the number of observations in each group. Finally, the standard normal deviate ( $Z$ ) was computed using the proportional index. Table 7 shows the process results for the upmost part of the G5 group.

Table 7 – Database organization example (G5)

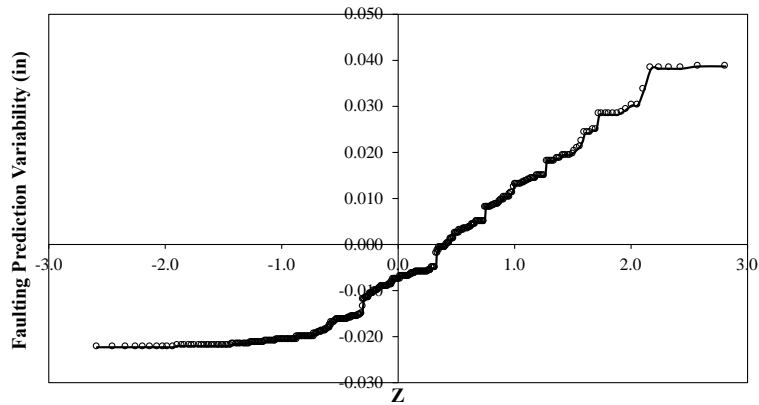
Index	Predicted Faulting (in)	Measured Faulting (in)	Prediction Variability (in)	Proportional Index	Z
1	0.064	0.12	0.056	99.72%	2.76
2	0.073	0.10	0.027	99.43%	2.53
3	0.067	0.09	0.023	99.15%	2.38
4	0.056	0.07	0.014	98.86%	2.28
5	0.057	0.07	0.013	98.58%	2.19
6	0.056	0.06	0.004	98.29%	2.12
7	0.067	0.07	0.003	98.01%	2.05
8	0.067	0.07	0.003	97.72%	2.00
9	0.067	0.07	0.003	97.44%	1.95
10	0.059	0.06	0.001	97.15%	1.90
11	0.059	0.06	0.001	96.87%	1.86
12	0.060	0.06	0.000	96.58%	1.82
13	0.064	0.06	-0.004	96.30%	1.79
14	0.064	0.06	-0.004	96.01%	1.75
15	0.064	0.06	-0.004	95.73%	1.72
16	0.056	0.05	-0.006	95.44%	1.69
17	0.056	0.05	-0.006	95.16%	1.66
18	0.067	0.06	-0.007	94.87%	1.63
19	0.067	0.06	-0.007	94.59%	1.61
20	0.067	0.06	-0.007	94.30%	1.58
.	.	.	.	.	.
.	.	.	.	.	.
.	.	.	.	.	.
n = 351					

### 3.1.3.3 Step 3: Distress Prediction Variability Analysis

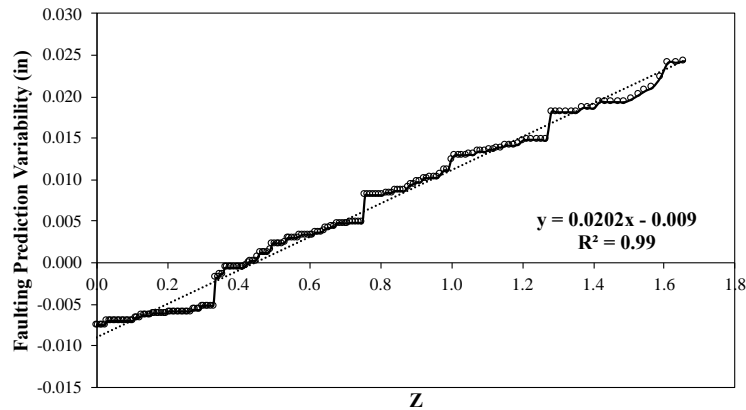
The “survivals” behaviour can be expressed as how faulting prediction variability relates to the standard normal deviate ( $Z$ ) for each groups’ database. As an example, Figure 22 presents this correlation for group G3. Ideally, the correlation would be represented by a linear line with a zero intercept, meaning that the average predicted faulting was equal to the average measured faulting. However, due to the high amount of measured faulting equal to zero and the previously discussed uncertainties with both the prediction model and the measured data, the actual relationship is

represented by a more complex curve. Nevertheless, the majority of the data (from Z equals -0.7 to 2.0) fits a quasi-linear line.

A reasonable assumption would be that the rehabilitated data missing from the distress database would be located along this line. Since the average predicted faulting is higher than the average measured faulting, these potential rehabilitated sections are assumed to have higher levels of faulting. Therefore, the analysis was focused on the data ranging from 50% (Z=0) to 95% of the available data (Figure 22b). The remaining groups are displayed in Figure 23.



(a)



(b)

Figure 22 – Faulting prediction variability versus standard normal deviate (Z) for Group 3

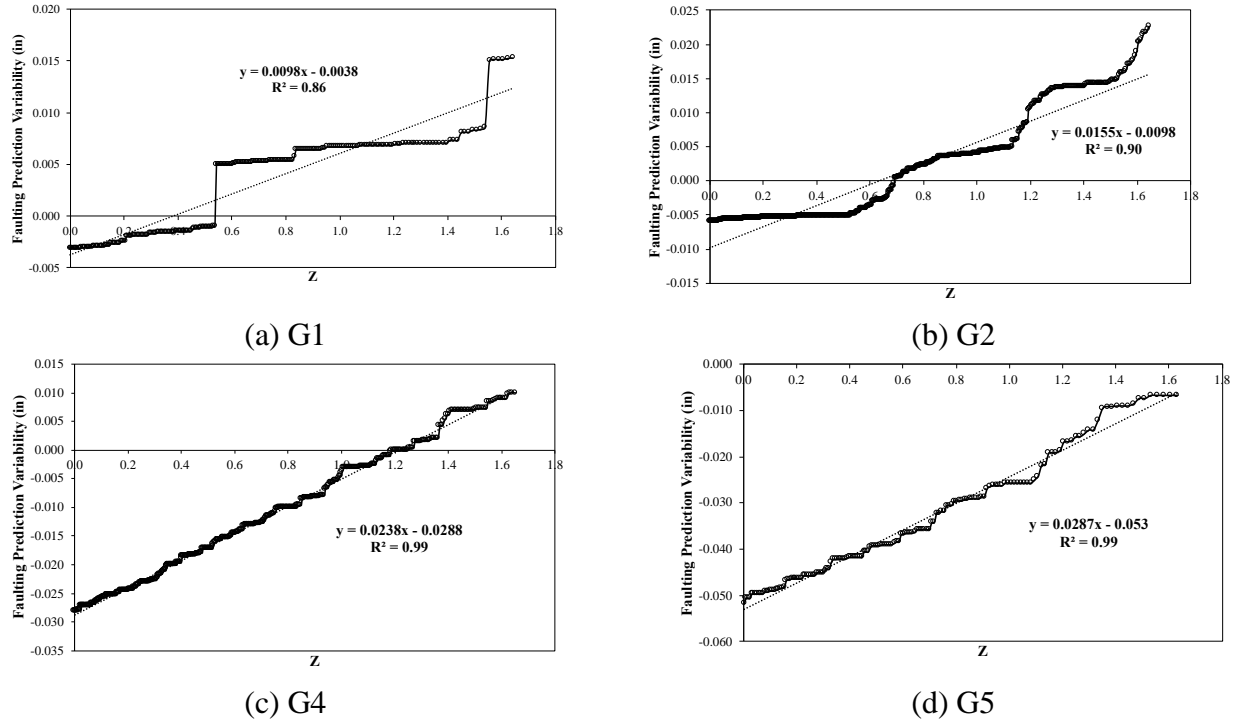


Figure 23 – Faulting prediction variability versus standard normal deviate (Z)

### 3.1.3.4 Step 4: Standard Deviation and Intercept Models

For calibration of the original reliability model in the MEPDG, the regression between each groups' standard deviation and average predicted faulting would be used to develop the calibrated standard deviation. For faulting reliability, the MEPDG indicates the following format [1,16]:

$$STD_{Pvi} = a \cdot Fault_{50\%i}^b + c \quad (34)$$

where:

- STD<sub>Pvi</sub> is the standard deviation of the faulting prediction variability,
- Fault<sub>50%i</sub> is the predicted faulting at 50% reliability,
- a, b and c are calibration coefficients.

Due to the uncertainties with the field data (zero faulting and potential rehabilitated sections), adopting the statistical values for the whole group is inappropriate for the reliability calibration using a RMS database. The data provided in Figure 22 and Figure 23 (regression slopes, i.e., standard deviation of the data range) is more adequate to represent the groups' standard deviation taking into account potential rehabilitated sections. Using data from Table 5 (average predicted distress) it is possible to establish a new standard deviation equation (Figure 24a):

$$STD_{Pvi} = 0.07602 \times Fault_{50\%i}^{0.35027} \quad (35)$$

As can be seen in Table 8, the coefficients for the RMS calibrated standard deviation are slightly lower than the current PA calibration.

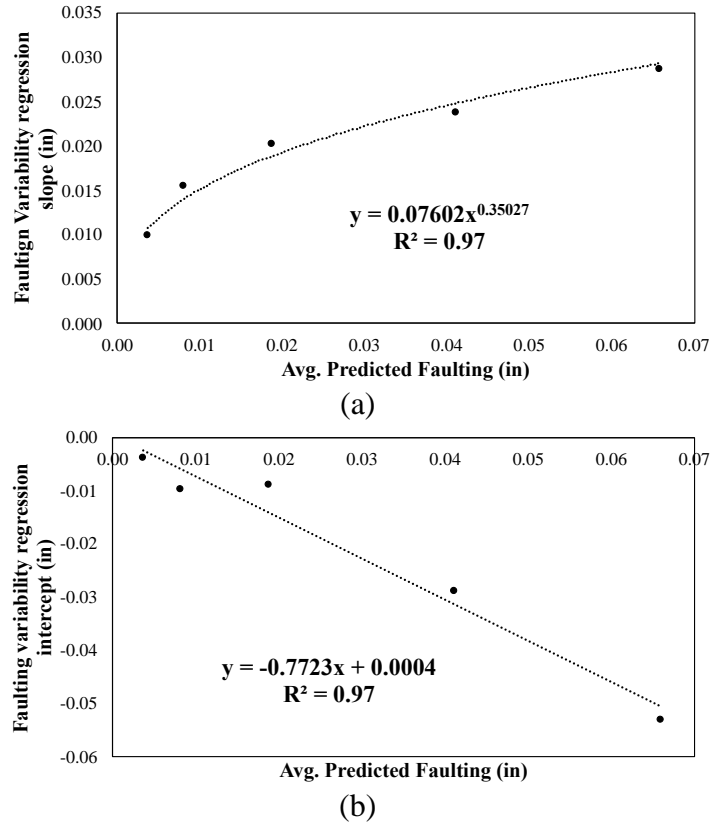


Figure 24 – Faulting variability regression (a) slope and (b) intercept versus average predicted faulting

Table 8 – National and PA reliability calibrations in comparison to the proposed calibration

	NCHRP 20-07	PA (current)	PA (RMS calibrated)
a	0.07162	0.08162	<b>0.07602</b>
b	0.368	0.3481	<b>0.35027</b>
c	0.00806	0.008	<b>0</b>

The standard deviation model is incorporated into Equation 32 to predicted faulting for different reliability levels. By incorporating Equations 34 and 35 into Equation 32, the current and the RMS calibrated reliability model are expressed, respectively, as follows:

**Current:**

$$Fault_{Ri} = Fault_{50\%i} + a \cdot Fault_{50\%i}^b \cdot Z_R + c \cdot Z_R \quad (36)$$

**RMS Calibrated:**

$$Fault_{Ri} = Fault_{50\%i} + a \cdot Fault_{50\%i}^b \cdot Z_R \quad (37)$$

where:

$Fault_{Ri}$  is the predicted average joint faulting at the reliability level R for year i.

The major difference between the two models is the lack of the c coefficient in the RMS calibrated rehabilitation model. In the current model, coefficient c is used along with the standard normal

deviate ( $Z_R$ ) to express unknown variabilities in both the predicted and measured faulting. This project proposes the use of the intercept model (Figure 24b) as a different approach to account for variability that is more related to potential rehabilitated sections.

The MEPDG reliability model calibration procedure requires that for each group the averaged measured and predicted distress indicators should be roughly the same. As previously discussed, the RMS faulting database fails to meet this requirement due to a significant potential number of rehabilitated sections. If the rehabilitated sections' information was available – and assuming that they present higher than average faulting levels – incorporating them into the database and groups would make the averaged predicted and measured faulting more equivalent. In this case, the regressions presented in Figure 22b and Figure 23 would have an intercept closer to zero.

Therefore, to indirectly consider the rehabilitated sections in the prediction variability, it is necessary to include the effect of the intercept model as well as the standard deviation. The intercept variation per each group versus average predicted faulting is presented in Figure 24b. As expected, for higher levels of predicted faulting, the intercept is higher because these groups are assumed to have more rehabilitated observations. Incorporating the intercept from the distress predictions would alter Equation 38 into the final RMS calibrated reliability model:

$$Fault_{Ri} = Fault_{50\%i} + a \cdot Fault_{50\%i}^b \cdot Z_R + d \cdot D_{50\%i} + e \quad (38)$$

Where  $Fault_{Ri}$  is the predicted faulting level at the reliability level R for year i;  $Fault_{50\%i}$  is the predicted faulting level at 50% reliability for year i;  $Z_R$  is the standard normal deviate for reliability level R; a and b are coefficients of the standard deviation model; d and e are coefficients of the intercept model.

In general, the RMS calibrated reliability model produces much less conservative faulting predictions than the national calibration (NCHRP 20-07) as exemplified by the hypothetical design in Figure 25.

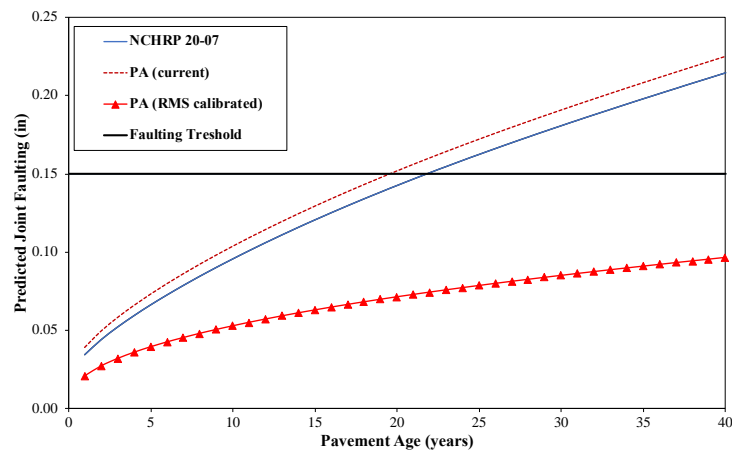


Figure 25 – Faulting predictions using a single faulting model (NCHRP 20-07 calibration) with different reliability models

### 3.2 Reliability Model Validation

The RMS calibrated reliability model was validated using RMS faulting observations with similar design parameters. The current PA faulting reliability model was also used in the simulations. Figure 26 present two cases of JPCP with different joint spacing (15 and 20 ft). For both cases, Pavement ME (PA calibration) was used with 95% reliability. Results of the simulations are compared to the field data, highlighting its 95<sup>th</sup> percentile in red. In a perfect simulation, the model curve would sit just below the 95<sup>th</sup> percentile field data for a 95% reliability prediction.

As can be seen, the current Pavement ME reliability model greatly overpredicts faulting for different sets of design features. The RMS calibrated reliability model decreases faulting predictions getting closer to the field data but still presenting a slightly conservative prediction.

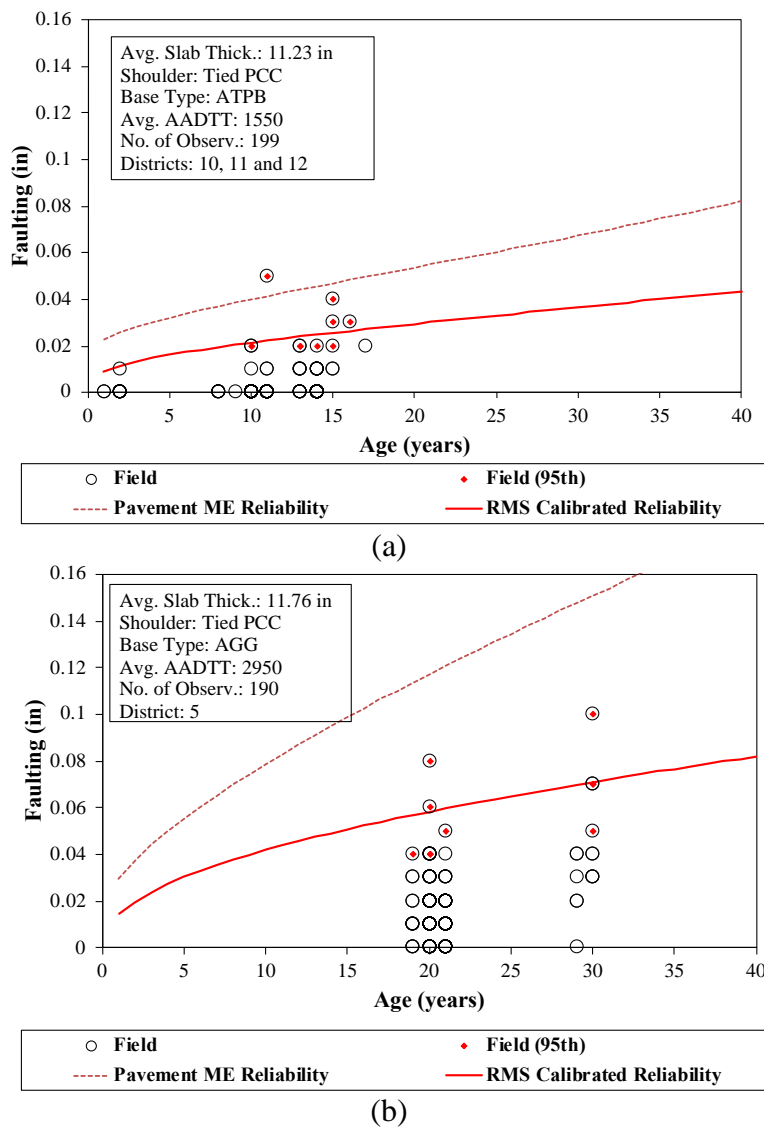


Figure 26 – Pavement ME faulting predictions using the current and the RMS calibrate reliability models (95% reliability) for (a) 15 ft JPCP and (b) 20 ft. JPCP

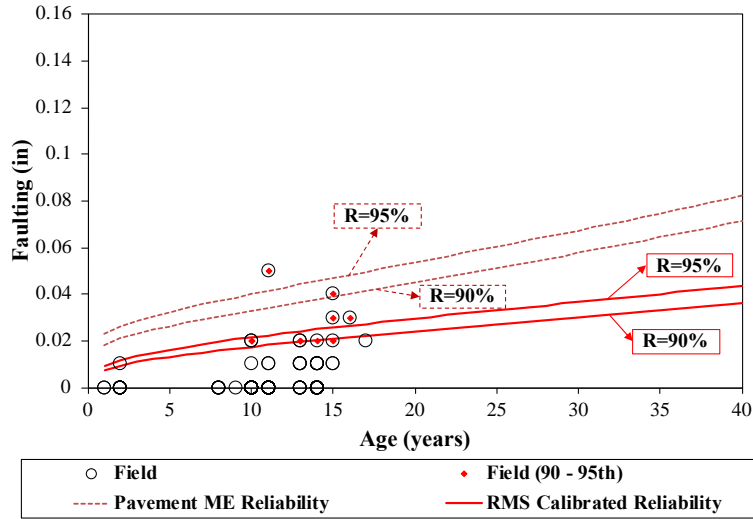
Similar to the calibration process, the model validation must also consider potential rehabilitated sections in the field. As an example, for data presented in Figure 26a, field sections were aged between 1 and 17 years old. Using the rehabilitation percentages presented in Figure 20, this means that based on 209 field observations available in the database, it is assumed that 10 observations were potentially rehabilitated and, for that, excluded from the distress database.

This means that the 95<sup>th</sup> critical faulting percentile can actually be the 90<sup>th</sup> percentile when considering a total of 209 observations (199 available plus 10 potential rehabilitations). However, not necessarily all rehabilitations were performed due to faulting. It is plausible that some sections were rehabilitated due to cracking or other type of distress. In this case, a prediction area using reliability levels between no rehabilitation due to faulting (95%) and all rehabilitations due to faulting (90%) is more suitable. Figure 27 shows prediction areas for two cases initially presented in Figure 26.

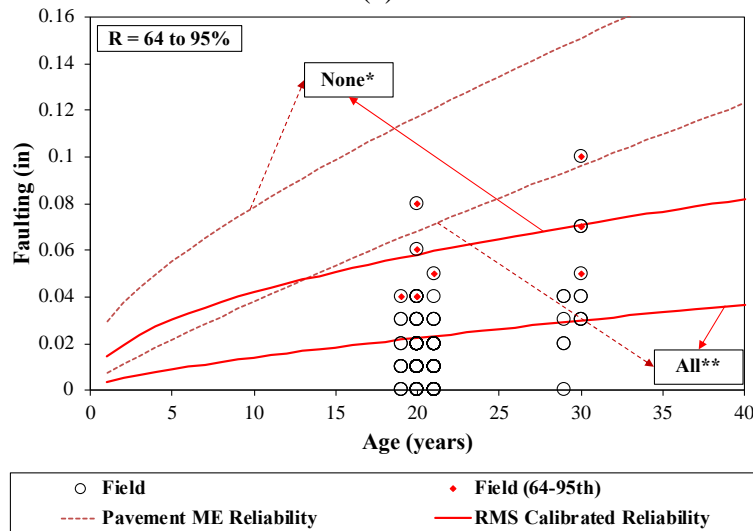
Using the potential rehabilitated data, the RMS calibrated reliability model predictions match the field performance better. For older sections (20 ft JPCP), the prediction area is much broader as there are more potential rehabilitated observations considered. For the case presented in Figure 27b, using only the available field database, the 95% reliability model was overpredicting field performance. Including the rehabilitated sections (additional 94 potential rehabilitated observations to the 190 observations in the original database) makes the field distress top percentile vary from 64<sup>th</sup> to 95<sup>th</sup>. For this particular case, it is possible to assume that about half of these rehabilitated observations were due to faulting.

Nevertheless, the use of potential rehabilitated sections is equally important for validation of the model as it is for calibration in order to avoid erroneous interpretations of the calibrated model prediction performance.





(a)



\* No rehabilitation was performed due to excessive faulting (R=95%)  
 \*\* All rehabilitations were performed due to excessive faulting (R=64%)

(b)

Figure 27 – Pavement ME faulting predictions using the current and the RMS calibrate reliability models for (a) 15 ft JPCP and (b) 20 ft JPCP considering rehabilitated sections

Figure 28 to Figure 31 present the validation for several field observations with matching design features for JPCP with 15 ft (Design 1) and 20 ft spaced joints (Design 2) according to the process previously described.

Figure 28 shows cases for the most common features for Design 1 (concrete slab thickness varying from 10 to 12 in, tied PCC shoulder, and asphalt permeable treated base - ATPB) under different levels of traffic. Figure 29 presents exceptions from the standard Design 1 features. In the same way, Design 2 standard design – same concrete thickness range and shoulder type but with aggregate bases (AGG) – are presented in Figure 30 and Figure 31 shows the exceptions for it.

As can be seen, using the RMS calibrated reliability model produces less conservative faulting predictions capturing more accurately the field behaviour when compared to the current reliability model. The full analysis of the validation is given in the next section.

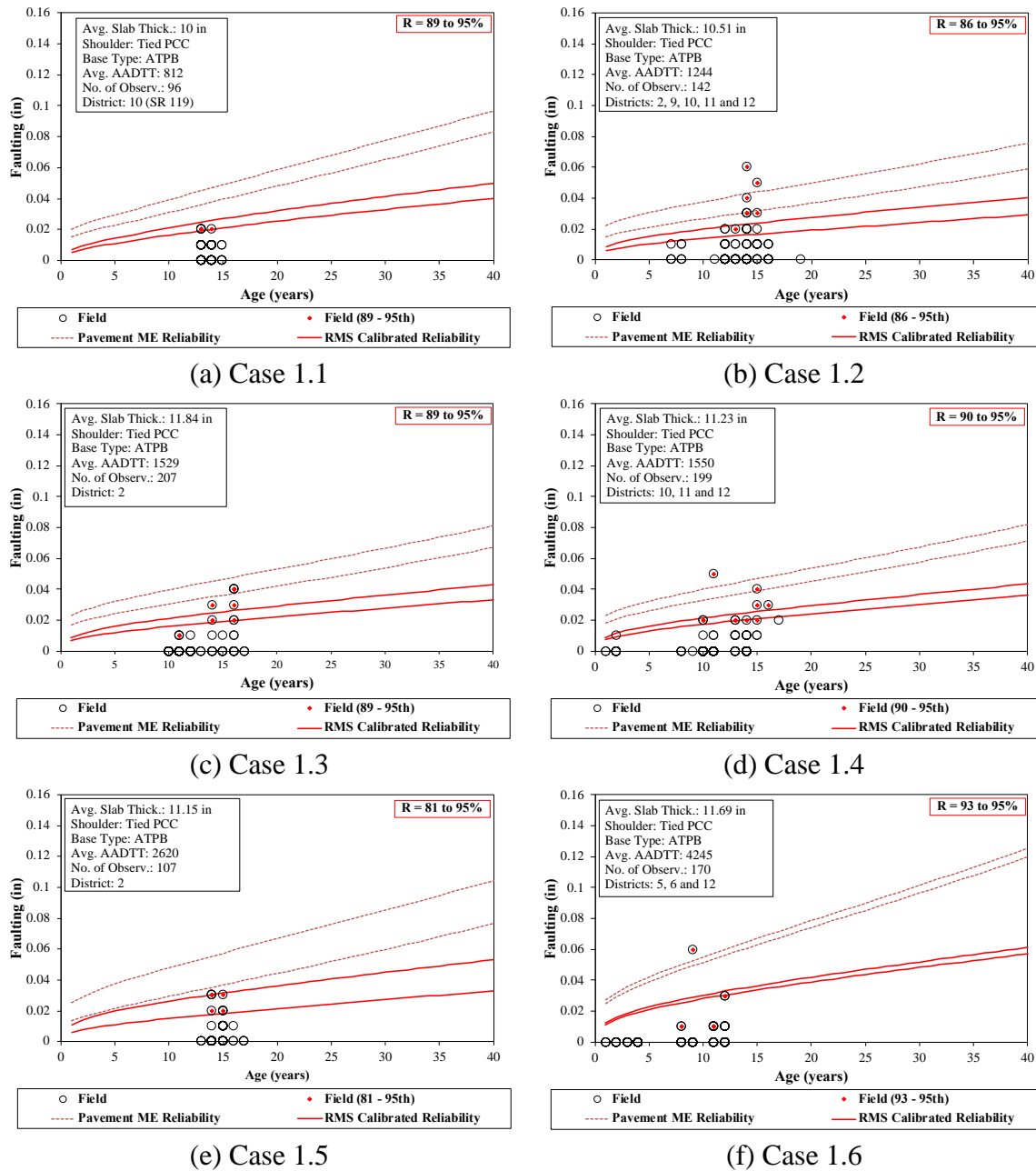
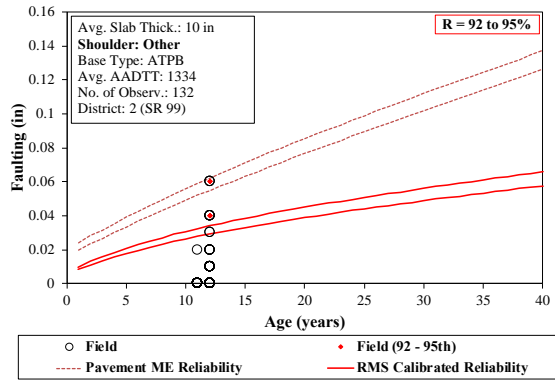
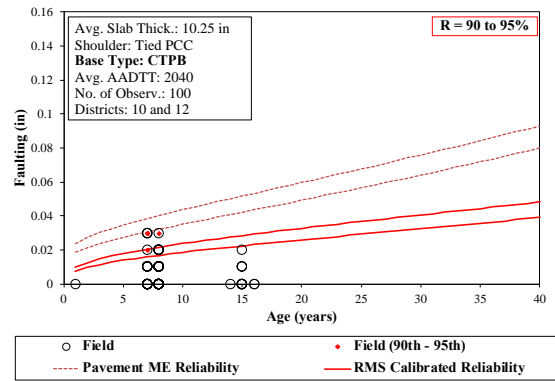


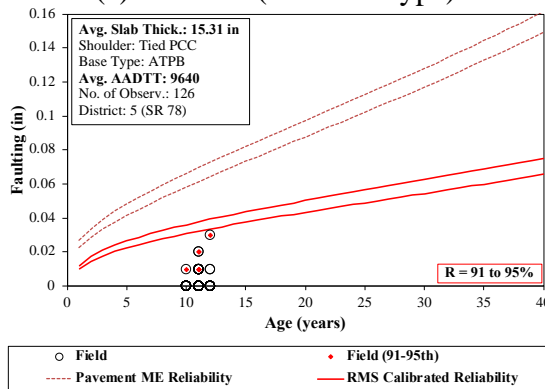
Figure 28 – Reliability models validation for the standard design of Design 1 (15 ft JPCP)



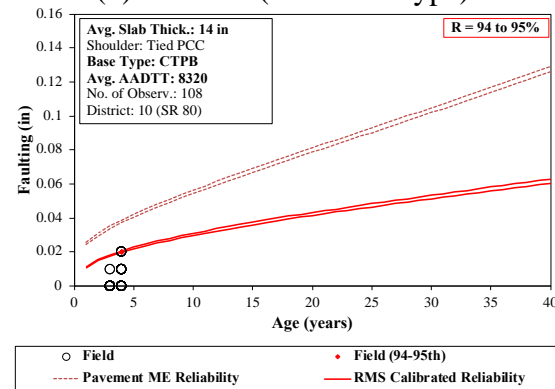
(a) Case 1.7 (Shoulder type)



(b) Case 1.8 (CTB base type)

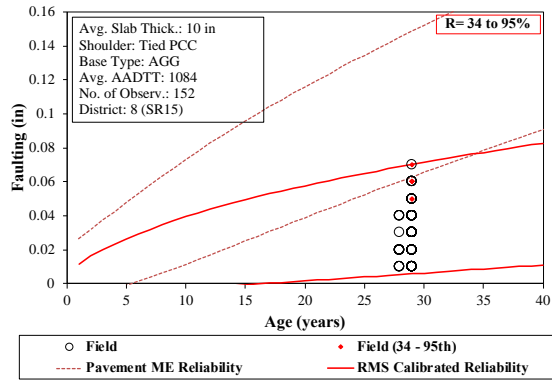


(c) Case 1.9 (High traffic)

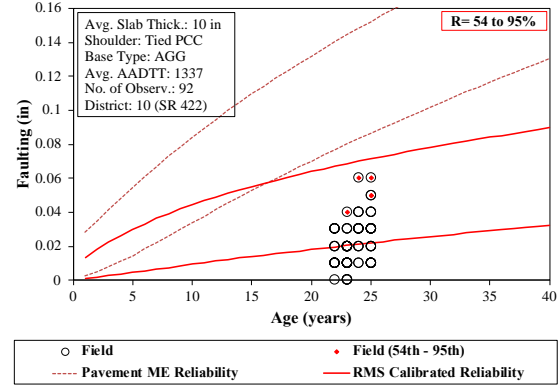


(c) Case 1.10 (CTB base type; high traffic)

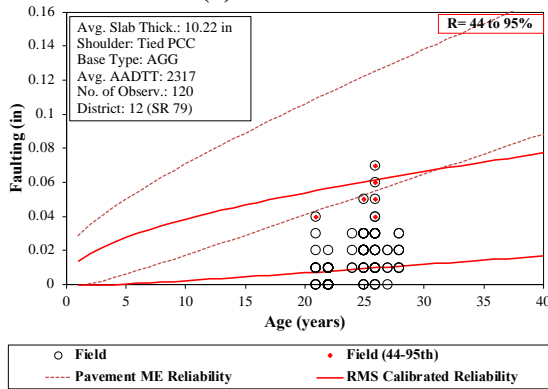
Figure 29 – Reliability models validation for exceptions of the standard design of Design 1 (15 ft JPCP)



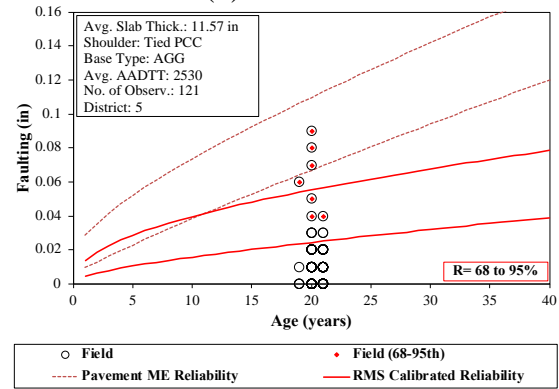
(a) Case 2.1



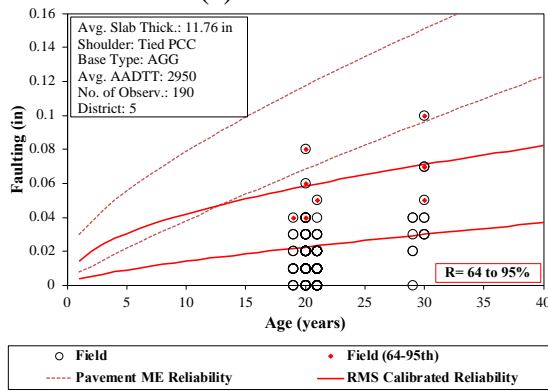
(b) Case 2.2



(c) Case 2.3



(d) Case 2.4



(e) Case 2.5

Figure 30 – Reliability models validation for the standard design of Design 2 (20 ft JPCP)

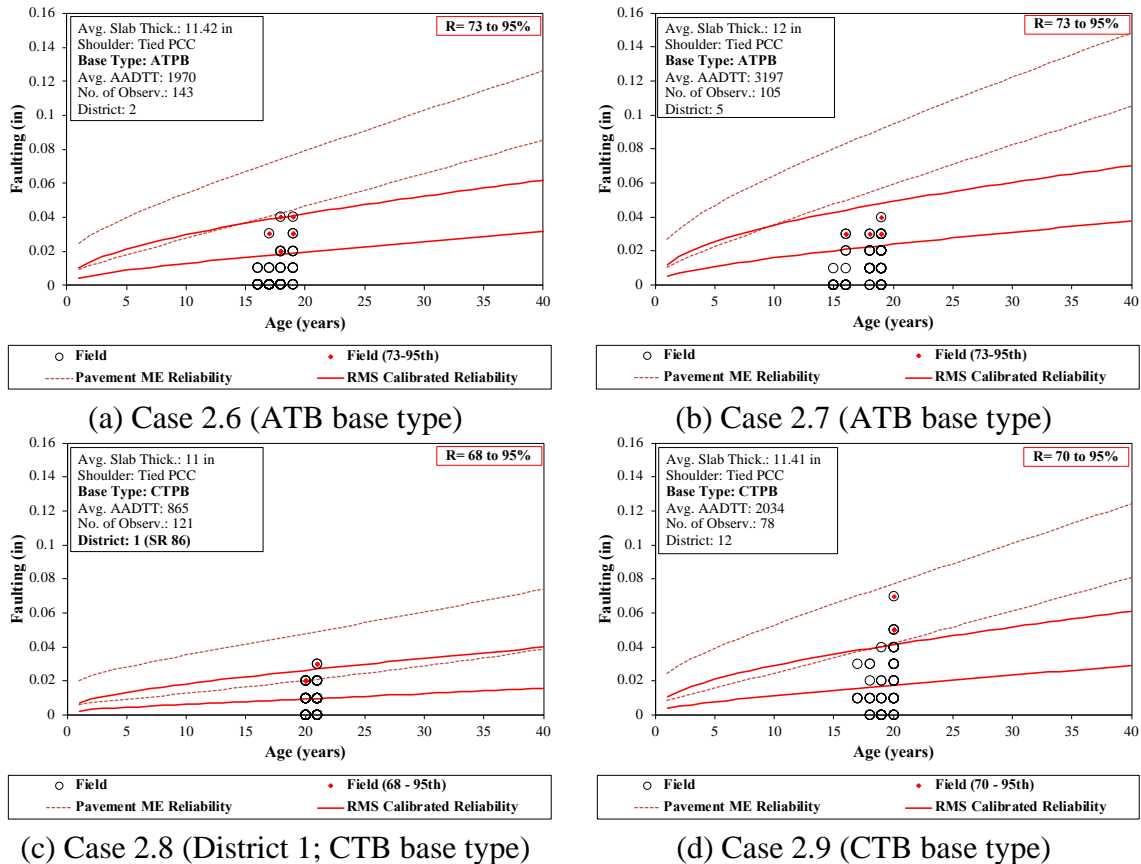


Figure 31– Reliability models validation for exceptions of the standard design of Design 2 (20 ft JPCP)

### 3.3 Faulting Model Modifications

The calibration of the reliability model presented above required an introduction of the intercept coefficient indicating the discrepancy between the estimated median faulting and Pavement ME faulting predictions. To address this discrepancy, the faulting model was modified to eliminate the need for this artificial term. In order to better identify the deficiencies of the current Pavement ME faulting model, the results of the validation displayed in Figure 28 to Figure 31 were evaluated.

As it was explained before, each of the Figure 28 through Figure 31 contains the following information:

- Faulting predictions for the 95% reliability level using the Pavement ME reliability model and the RMS-calibrated reliability model.
- Faulting predictions using the Pavement ME reliability model and the RMS-calibrated reliability model for the reliability level equal to 95% minus the percentage rehabilitated sections for this case.
- Measured faulting data. The observations corresponding to the top 5% faulting are marked with red dots at the centre of the circle.

An evaluation of the prediction accuracy was conducted for each case and each reliability model.

Model predictions for a certain case were classified as “Overprediction” if the top 5% faulting observations were located below the prediction of reliability level equal to 95% minus the percentage rehabilitated sections for this case. This indicates that even if it is assumed that all rehabilitated sections, if they had stayed in service, would exhibit faulting higher than the 95<sup>th</sup> percentile faulting, the predicted 95% reliability faulting is excessively conservative.

Model predictions for a certain case were classified as “Underprediction” if the top 5% faulting observations are located above the prediction for the 95% reliability level. This indicates that even if it is assumed that all the rehabilitated sections, if they had stayed in service, would exhibit faulting higher than the 95<sup>th</sup> percentile faulting, the predicted 95% reliability faulting is lower than faulting of the top 5% of the observations.

Finally, if the top 5% faulting observations are located below the prediction for the 95% reliability level but above the reliability level equal to 95% minus the percentage rehabilitated sections for a given case then the predictions were classified as “Accurate.” The only exception was made for Case 2.2 using the RMS-calibrated model. This case has one of the highest percentages of potential rehabilitated sections. Although it has to be formally classified “Accurate,” the top 5% of the faulting observations were much closer to the 95% reliability prediction than to the lower (54%) reliability level prediction. Since a large number of sections was assumed rehabilitated, there is a significant chance that some of them were rehabilitated due to high faulting level and would have faulting level higher than the faulting of the in-service sections. Because of this, Case 2.2 was classified as “Underprediction.”

The results of this analysis are presented in Table 9. Table 9 also presents the Average Annual Daily Truck Traffic (AADTT) with a colour scale, as follows: green for low traffic, yellow for moderate traffic, and red for high levels of traffic.

Based on Table 9, the following observations can be made on the performance of the faulting model using the Pavement ME reliability model:

- The model overpredicts faulting for cases.
- Cases ATPB present a higher degree of overprediction.
- As traffic increases, so does the degree of overprediction.
- For cases with Cement Treated Permeable Base (CTPB) and low to moderate level of traffic (Cases 1.8, 2.8, and 2.9) the model overpredicts in a lesser degree than for counterpart cases with similar traffic and ATPB.

These observations strongly indicate that the model incorrectly accounts for the base type as well as overpredicts faulting for high traffic levels.

Table 9 – Prediction performance evaluation of the faulting model using the current and RMS calibrated reliability models

Case	Design Features	AADTT	Pavement ME Reliability Model	RMS Calibrated Reliability Model
1.1	Standard	812	Overprediction	Accurate
1.2	Standard	1244	Overprediction	Accurate
1.3	Standard	1529	Overprediction	Accurate
1.4	Standard	1550	Overprediction	Accurate
1.5	Standard	2620	Overprediction	Accurate
1.6	Standard	4245	Overprediction	Overprediction
1.7	"Other" Shoulder	1334	Overprediction	Underprediction
1.8	CTPB Base	2040	Overprediction	Underprediction
1.9	High Traffic	9640	Overprediction	Overprediction
1.10	CTPB; High Traffic	8320	Overprediction	Accurate
2.1	Standard	1084	Overprediction	Underprediction
2.2	Standard	1337	Overprediction	Underprediction
2.3	Standard	2317	Overprediction	Accurate
2.4	Standard	2530	Overprediction	Accurate
2.5	Standard	2950	Overprediction	Accurate
2.6	ATB Base	1970	Overprediction	Accurate
2.7	ATB Base	3197	Overprediction	Accurate
2.8	District 1; CTPB Base	865	Overprediction	Accurate
2.9	CTPB Base	2034	Overprediction	Underprediction

Concerning the RMS-calibrated reliability predictions:

- Out of 19 cases, the model underpredicts 5 cases and overpredicts 2 cases.
- Overpredictions are related to higher levels of traffic (Cases 1.6 and 1.9).
- Underprediction tends to happen with CTPB bases (Cases 1.8 and 2.9). Expect for District 1 (Case 2.8) and higher levels of traffic (Case 1.10).
- Underprediction also happened for Cases 1.7 and 2.1.
- Case 1.7 is the only case presenting shoulder type “other” (not tied PCC). This can be explained by the low number of observations containing this design feature in the calibration database.
- Cases 2.1 and 2.2 (standard design for 20 ft JPCP) are composed of sections with age 22 and older subjected to low levels of traffic. These sections, obtained from a single SR, are expected to be composed of, as much as, 50% of “survivals”. Again, no information on why these sections were rehabilitated is available.

Again, these observations corroborate the presence of issues with the current model for ATPB base type and high traffic level. In addition, even though the RMS-calibrated reliability model leads to more realistic faulting predictions, the current faulting model must be modified. As seen in the Figure 28 to Figure 31, the faulting prediction curve should be less steep after five years. That can be achieved by decreasing the slope of mid-range and long-term faulting development.

### 3.3.1 Faulting Model Modification and Calibration

The current MEPDG model (described in detail in Chapter 2), incorporated in Pavement ME, determines faulting at each month as a sum of faulting increments from all previous months in the pavement life using the following model:

$$Fault_m = \sum_{i=1}^m \Delta Fault_i \quad (39)$$

$$\Delta Fault_i = C_{34} \times (FAULTMAX_{i-1} - Fault_{i-1})^2 \times DE_i \quad (40)$$

$$FAULTMAX_i = FAULTMAX_0 + C_7 \times \sum_{j=1}^m DE_j \times \text{Log}(1 + C_5 \times 5.0^{EROD})^{C_6} \quad (41)$$

$$FAULTMAX_0 = C_{12} \cdot \delta_{curling} \cdot \left[ \text{Log}(1 + C_5 \times 5.0^{EROD}) \times \text{Log} \left( \frac{P_{200} \text{WetDays}}{P_s} \right) \right]^{C_6} \quad (42)$$

where:

$Fault_m$  is the mean joint faulting at the end of month  $m$ , in.;

$\Delta Fault_i$  is the incremental change (monthly) in mean transverse joint faulting during month  $i$ , in.;

$FAULTMAX_i$  is the maximum mean transverse joint faulting for month  $i$ , in.;

$FAULTMAX_0$  is the initial maximum mean transverse joint faulting, in.;

$EROD$  is the base/subbase erodibility factor;

$DE_i$  is the differential density of energy of subgrade deformation accumulated during month  $i$ , calculated by DE regression model;

$\delta_{curling}$  is the maximum mean monthly slab corner upward deflection PCC due to temperature curling and moisture warping;

$P_s$  is the overburden on subgrade, lb;

$P_{200}$  is the percent subgrade material passing #200 sieve;

$WetDays$  is the average annual number of wet days (greater than 0.1 in. rainfall);

$C_{1,2,3,4,5,6,7,12,34}$  are calibration constants.

The last two calibration constants,  $C_{12}$  and  $C_{34}$  can be calculated by the following equations [13]:

$$C_{12} = C_1 + C_2 \times FR^{0.25} \quad (43)$$

$$C_{34} = C_3 + C_4 \times FR^{0.25} \quad (44)$$

where:

$FR$  is the base freezing index defined as percentage of time the top base temperature is below freezing (32°F) temperature.

Recent research conducted in Chile has proposed modifications to the model taking into more consideration the effect of adequate drainage and fine material content regarding the number of wet days [17]. The study concluded that the model ignores the effect of lateral drainage.

The Chilean researchers introduced a new calibration coefficient to account for the reduction in faulting due to drainage improvements. These recommendations were adapted in this study. A new calibration coefficient reducing the time of subgrade being exposed to a saturation condition due to the presence of a permeable base was introduced. The following faulting model is proposed:



$$Fault_m = \sum_{i=1}^m \Delta Fault_i \quad (45)$$

$$\Delta Fault_i = C_{34} \times (FAULTMAX_{i-1} - Fault_{i-1})^2 \times DE_i \quad (46)$$

$$FAULTMAX_i = FAULTMAX_0 + C_7 \times \sum_{j=1}^m DE_j \times \text{Log}(1 + C_5 \times 5.0^{EROD})^{C_6} \times \left[ \text{Log}(1 + C_5 \times 5.0^{EROD}) \times \text{Log} \left( \frac{P_{200}(C_9 \text{ WetDays})}{P_s} \right) \right]^{C_6} \quad (47)$$

$$FAULTMAX_0 = C_{12} \cdot \delta_{curling} \cdot \left[ \text{Log}(1 + C_5 \times 5.0^{EROD}) \times \text{Log} \left( \frac{P_{200}(C_9 \text{ WetDays})}{P_s} \right) \right]^{C_6} \quad (48)$$

where,

$C_9$  is a calibration constant.

If no permeable base is present, then the coefficient  $C_9$  is equal to 1. The presence of a permeable base can be accounted in the modified model by assigning the value of this coefficient less than 1.

Another modification of the faulting model is related to the default base load transfer efficiency. Table 7 presents the Pavement ME and the modified load transfer efficiencies for various base types.

Table 10 - Modification of transverse joint load transfer efficiencies for base contributions.

Base Type	LTE <sub>base</sub>	
	Pavement ME	Proposed Model
Aggregate base	20%	20%
Asphalt-treated permeable base	30%	40%
Cement-treated permeable base	40%	30%

Figure 32 exemplifies the difference in performance for a hypothetical case of JPCP design using the current and the modified model. Faulting predictions at 95% reliability were estimated using the current Pavement ME reliability model. There is a slight reduction in faulting prediction when introducing the modifications. An increase in 4 years of designed life is observed when using the modified model. For this simulation,  $C_9$  was set at 1. The next section will provide the calibration of  $C_9$  along with the other coefficients.

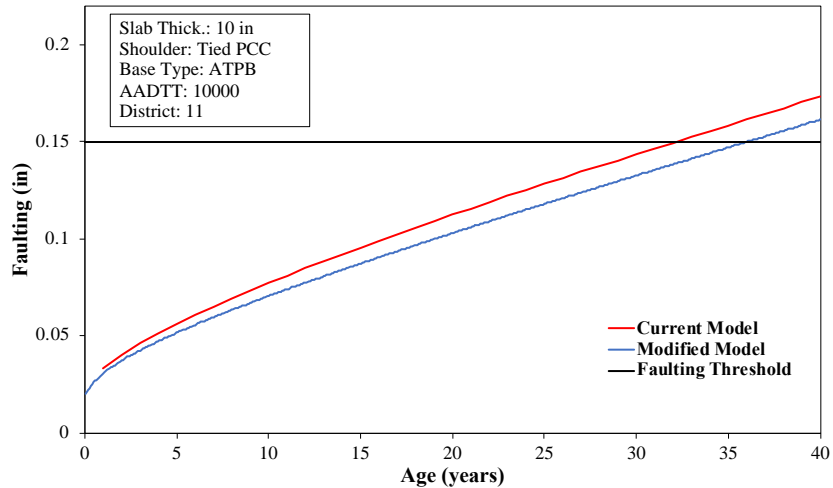


Figure 32 – Faulting prediction (95% reliability) using the current and the modified faulting models

### 3.3.1.1 Coefficients Calibration

According to the MEPDG, the model coefficients affect faulting generally in two ways:

- a) Coefficients that affect the shape of the faulting development curve over time (C1 to C4, and C7). C1 and C2 influence mid-range faulting development, while C3 and C4 impact its initial rate. C7 regulates the long-term faulting development.
- b) Coefficients that represent effects of design features and project conditions, such as dowel diameter and base erodibility (C5, C6, and C8). C5 is related to material erodibility and how that affects faulting development while C6 correlates faulting development to subgrade properties, percentage of fine material, and number of wet days. C8 represents the rate deterioration of doweled joints.

As mentioned before, the new coefficient (C9) characterizes the effect of permeable bases.

A sensitivity analysis was conducted for all calibration coefficients (Figure 33 and Figure 34) to identify which coefficients should be focused on to improve the faulting model. The hypothetical pavement was composed of 15 ft joint spaced JPCP with tied PCC shoulders, over an ATPB subjected to an AADTT of 2700 (average of field data cases). Faulting predictions are for 50% reliability.

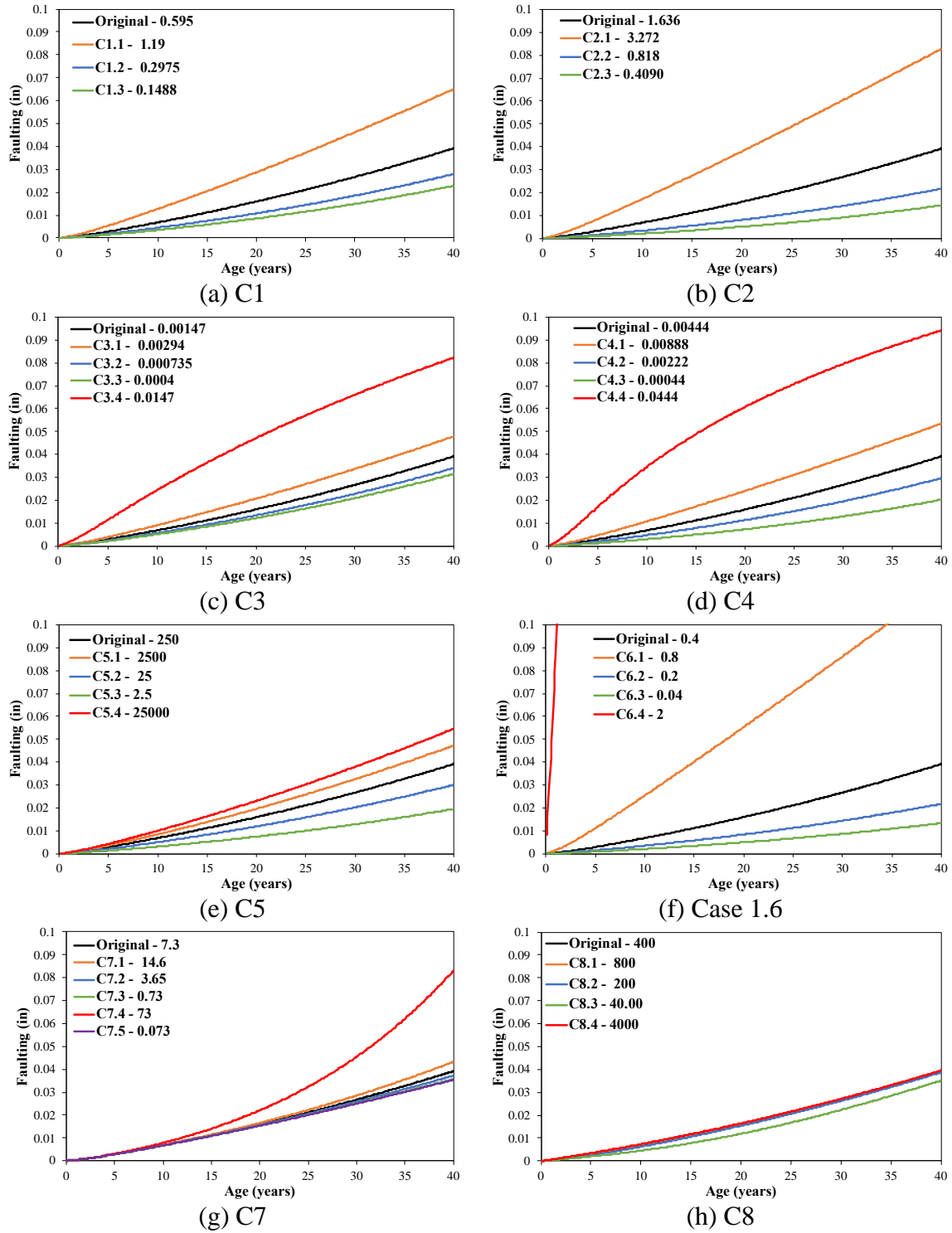


Figure 33 – Coefficient sensitivity analysis

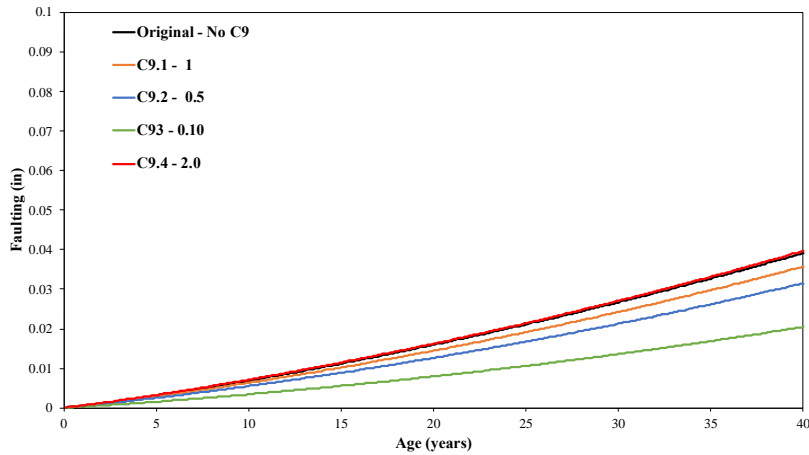


Figure 34 – C9 sensitivity analysis

Decrease of coefficients related to mid-range (C1 and C2) and long-term (C7) faulting development are of interest for this project since the objective is to make the faulting development curve less steep. However, that can significantly reduce initial faulting development. To counter this, C3 and C4 can be increased. C9 is expected to be lower for more permeable bases like ATPB and CTPB then for aggregate bases.

The reliability section of this chapter indicated that the current model mainly overpredicts faulting. When developing the RMS calibrated reliability model, the intercept model was used to correct this overprediction by adjusting predicted faulting in way that average measured and predicted faulting would be more equivalent for each group. The initial process for the calibration was determining coefficients that would approximately equalize faulting predictions of the modified model to the current model considering the intercept model in the latter. Some cases, with varying joint spacing, AADTT, and base type were selected for this process. Faulting predictions (50% reliability), selected for each case for the year where most field data are located, should be as close to 1 as possible. Figure 35 shows the result of the iteration.

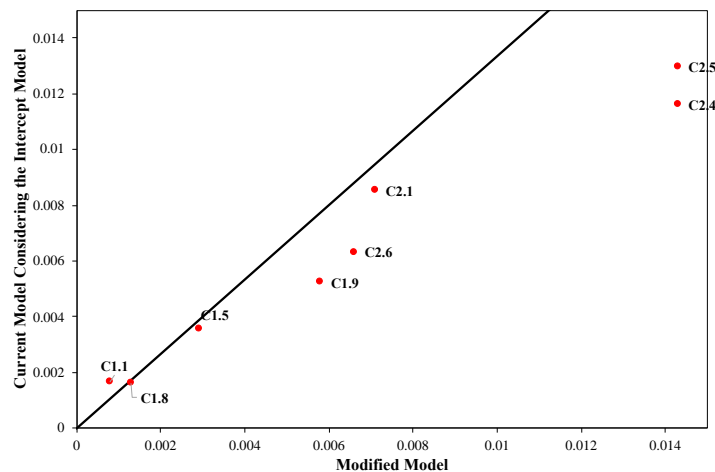


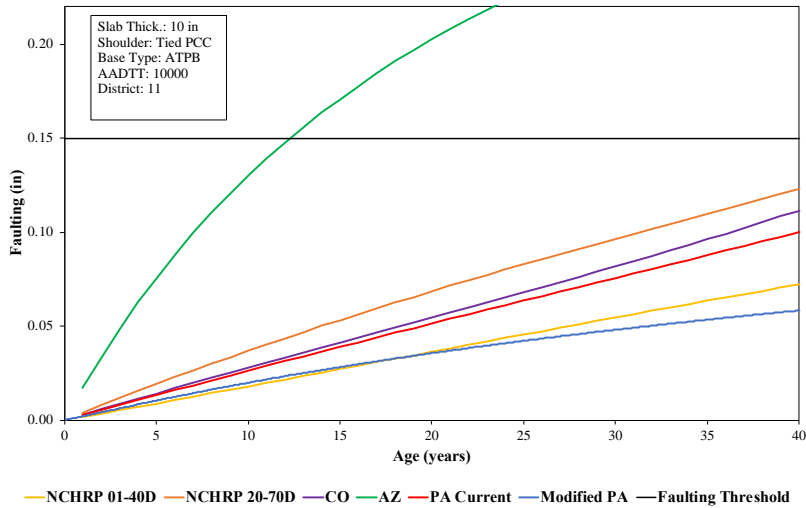
Figure 35 – Iteration result to equalize faulting predictions between current and modified model considering intercept model

However, as seen in Table 9, predictions considering the intercept model can underpredict some cases. Also, as mentioned before, RMS data presents high variability and uncertainties can lead to a less accurate model. With that, the coefficients were altered to present a slightly more conservative faulting predictions in comparison to the predictions considering the intercept model. The new coefficients are presented in Table 11 in contrast with past and current national coefficients and state calibrations.

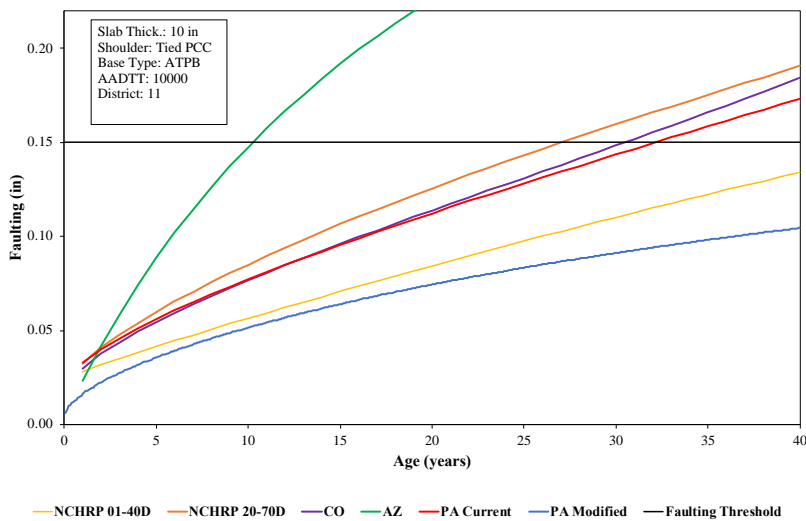
Table 11 – Faulting model calibration coefficients

	<b>NCHRP 01-40D</b>	<b>NCHRP 20-07</b>	<b>CO</b>	<b>AZ</b>	<b>PA Current</b>	<b>PA Modified</b>
Software Version	MEPDG 1.0	Pavement ME 2.3.1	MEPDG 1.0	Pavement ME 2.3.1	Pavement ME 2.3.1	Pavement ME 2.3.1
C1	1.0184	0.595	0.51	0.0355	0.595	0.4
C2	0.9165	1.636	0.00838	0.1147	1.636	1.1
C3	0.002185	0.00217	0.00147	0.00436	0.00147	0.0035
C4	0.000884	0.00444	0.00835	1.10E-07	0.00444	0.015
C5	250	250	5999	20000	250	250
C6	0.4	0.47	0.8404	2.0389	0.4	0.4
C7	1.83312	7.3	5.9293	0.189	7.3	2
C8	400	400	400	400	400	400
C9	N/A	N/A	N/A	N/A	N/A	ATPB = 0.3 CTPB = 0.3 AGG = 1.0

Figure 36 shows the comparison between models listed in Table 11 for 50% and 95% reliability. The modified PA model developed in this study presents much less conservative faulting predictions than the current PA model. The modified model predictions are closer to the original national calibration. Potentially the lack of consideration for rehabilitated sections in the calibration and validation databases used for the other models might explain the difference in predictions.



(a)



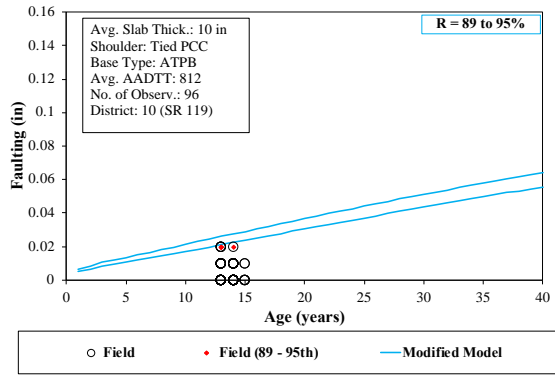
(b)

Figure 36 – Faulting predictions using different model calibrations for (a) 50% and (b) 95% reliability

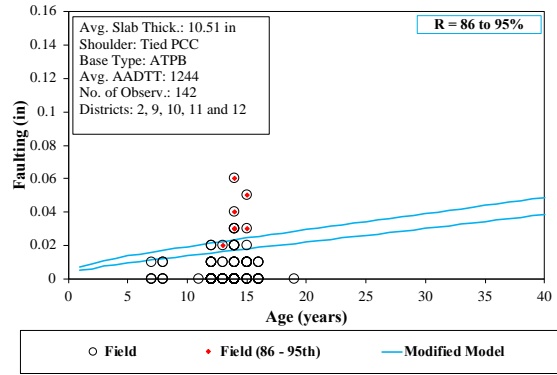
### 3.3.2 Modified Model Validation

The same cases used for validation of the reliability model as shown in Figure 28 to Figure 31 were used to validate the calibration of the full model. Figure 37 to Figure 40 present the results of the validation.

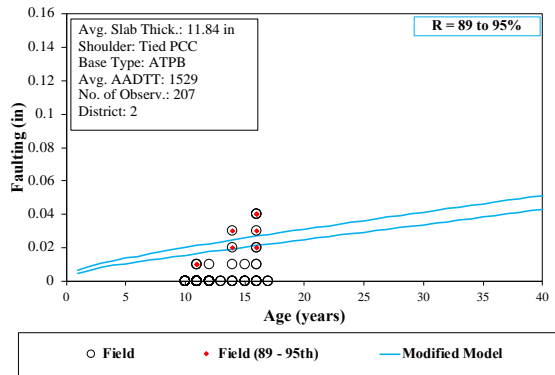
About half of the cases (10) could be placed in the “accurate” prediction category as established for Table 6. Although in a much lesser degree when compared to the current model, nine cases present overprediction of faulting. This is caused by the slightly more conservative approach in the coefficient calibration in contrast with the reliability study described in the previous section.



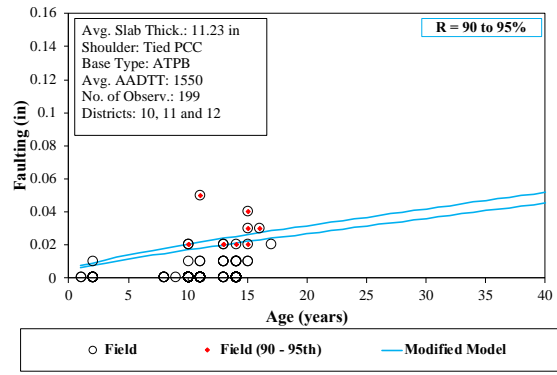
(a) Case 1.1



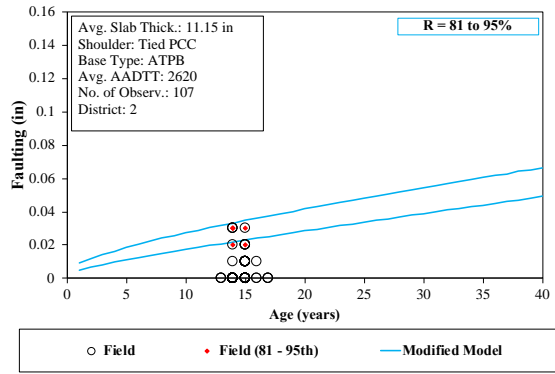
(b) Case 1.2



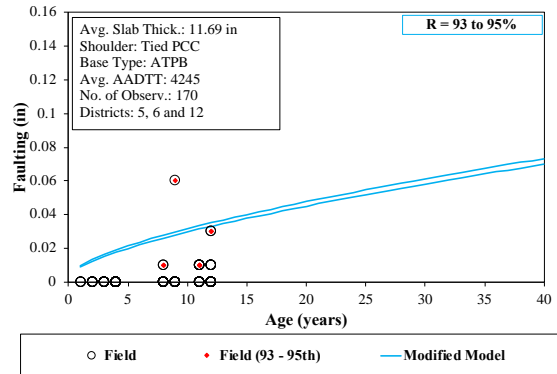
(c) Case 1.3



(d) Case 1.4

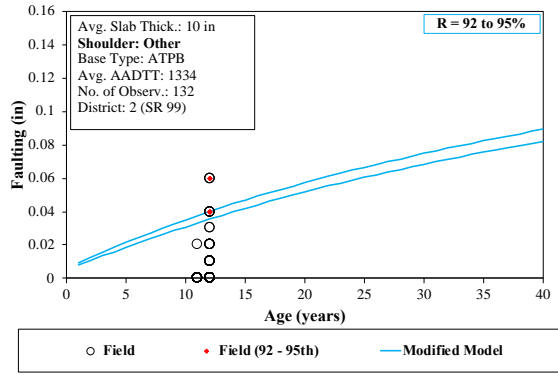


(e) Case 1.5

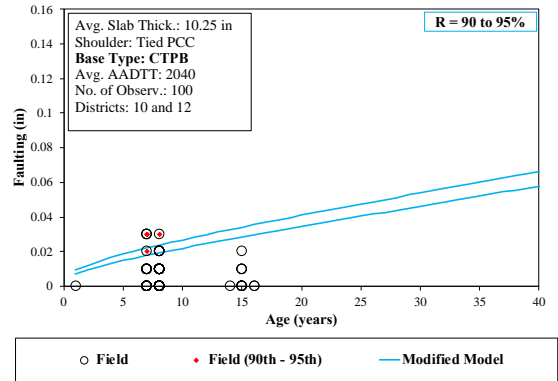


(f) Case 1.6

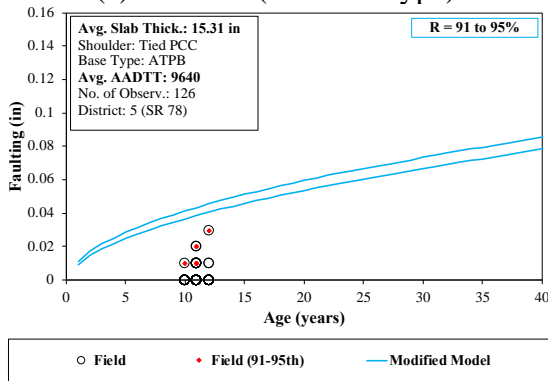
Figure 37 – Modified model validation for the standard design of Design 1 (15 ft JPCP)



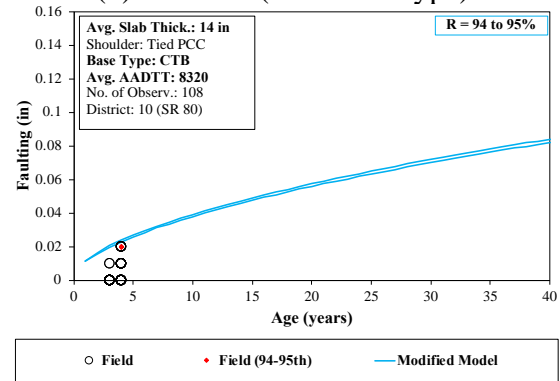
(a) Case 1.7 (Shoulder type)



(b) Case 1.8 (CTB base type)



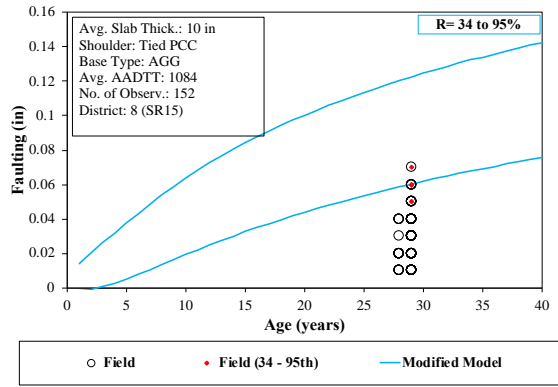
(c) Case 1.9 (High traffic)



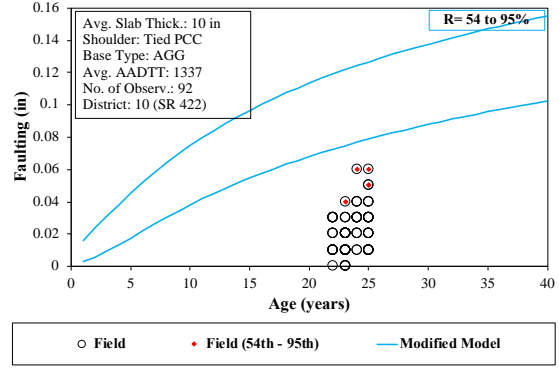
(c) Case 1.10 (CTB base type; high traffic)

Figure 38 – Modified model validation for exceptions of the standard design of Design 1 (15 ft JPCP)

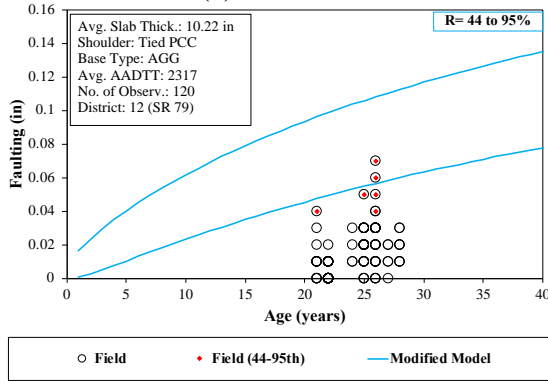




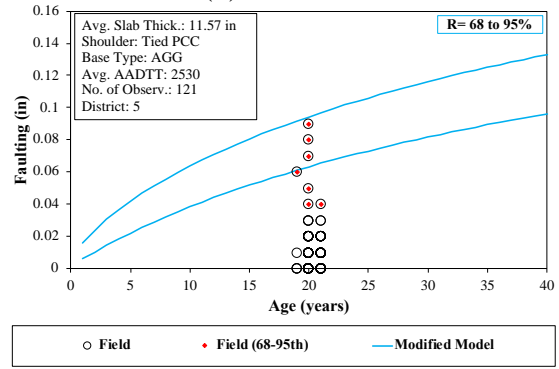
(a) Case 2.1



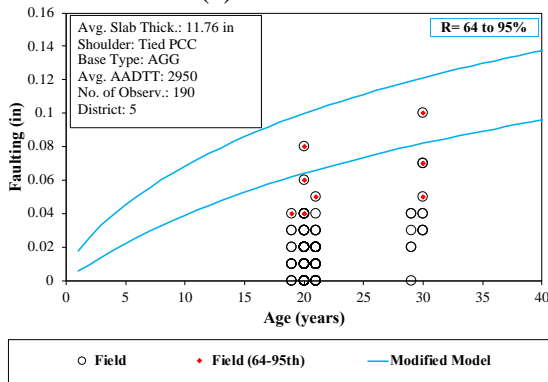
(b) Case 2.2



(c) Case 2.3



(d) Case 2.4



(e) Case 2.5

Figure 39 – Modified model validation for the standard design of Design 2 (20 ft JPCP)

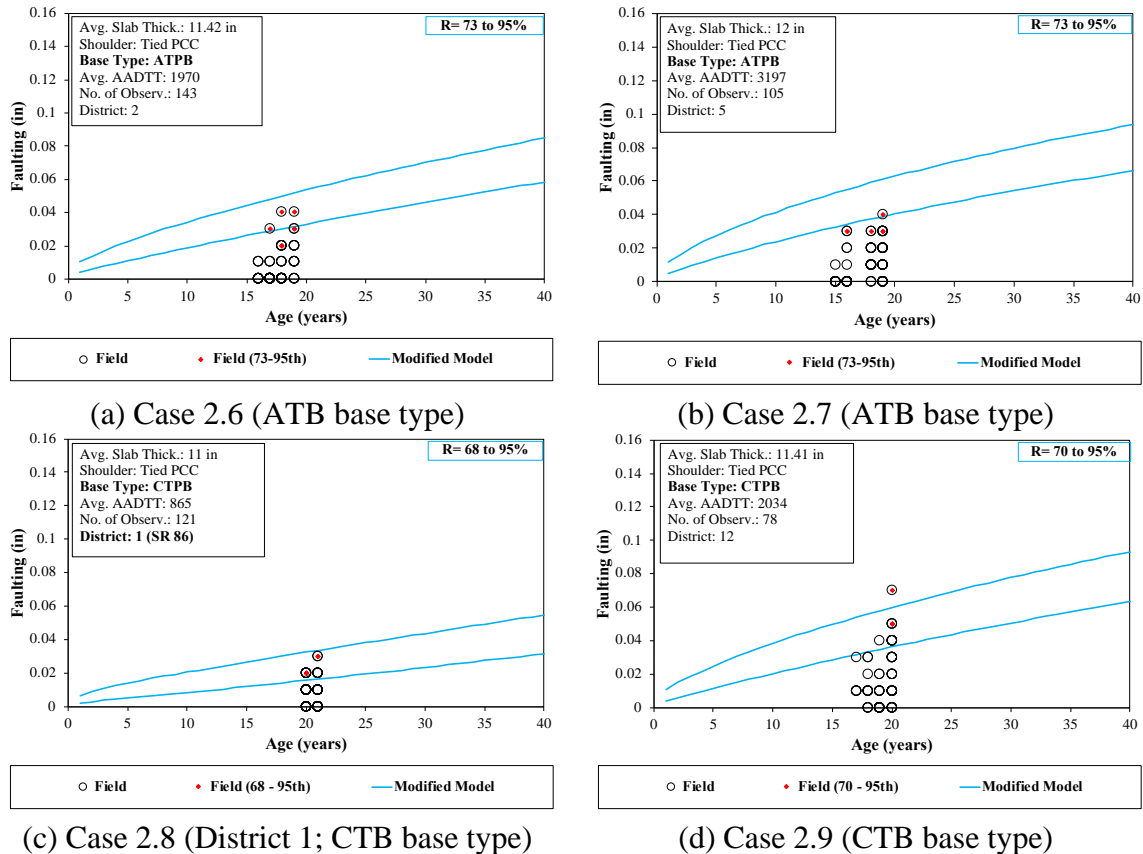


Figure 40 – Modified model validation for exceptions of the standard design of Design 2 (20 ft JPCP)

### 3.3.3 Modified Model Sensitivity Analysis

To facilitate faulting prediction using the new model, a program called PittFaultCompanion was developed as part of this study. PittFaultCompanion permits the user to select Pavement ME pavement projects folders and performs faulting predictions with the new model using the traffic, climate, and pavement structure information from the temporary files generated by Pavement ME.

A sensitivity analysis was conducted to further analyze the modified model faulting prediction model with respect to the effect of several design parameters. The base for the analysis was composed of a dowelled (1.5 in diameter) 10 in thick concrete slab (coefficient of thermal expansion set at  $5 \times 10^{-6} / ^\circ\text{F}$ ) over a ATPB with tied PCC shoulders subjected to an AADTT of 10,000 (bidirectional). The slab geometry for the base case was 12-ft slab width with 15-ft joint spacing. Several parameters were varied based on the collected field data. It should be noted that in this sensitivity analysis the requirements to meet the cracking performance criteria were ignored.

As expected, Figure 41 shows that an increase in traffic levels (AADTT) causes an increase in the predicted average faulting. For slab thickness (Figure 42), an increase in slab thickness results in a slight reduction of predicted faulting. A more significant reduction is observed when changing dowel diameter from 1.25 to 1.5 in.

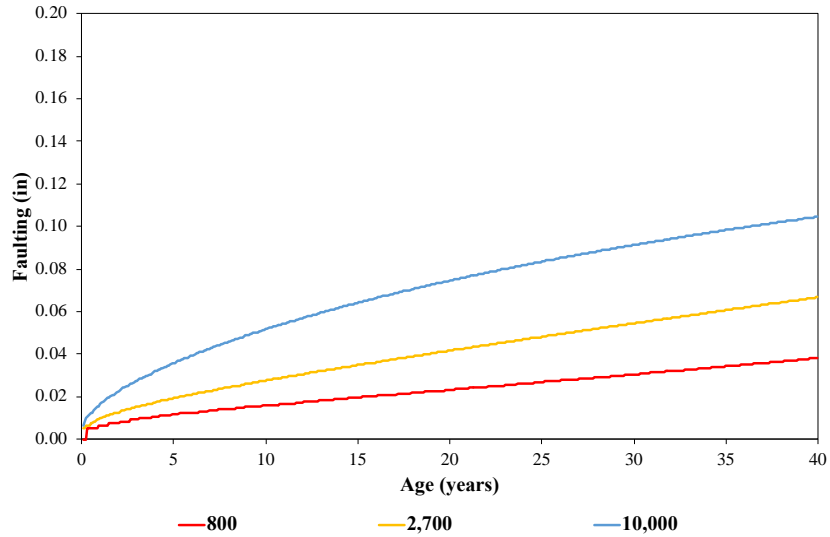


Figure 41 – Modified model faulting prediction for different levels of traffic

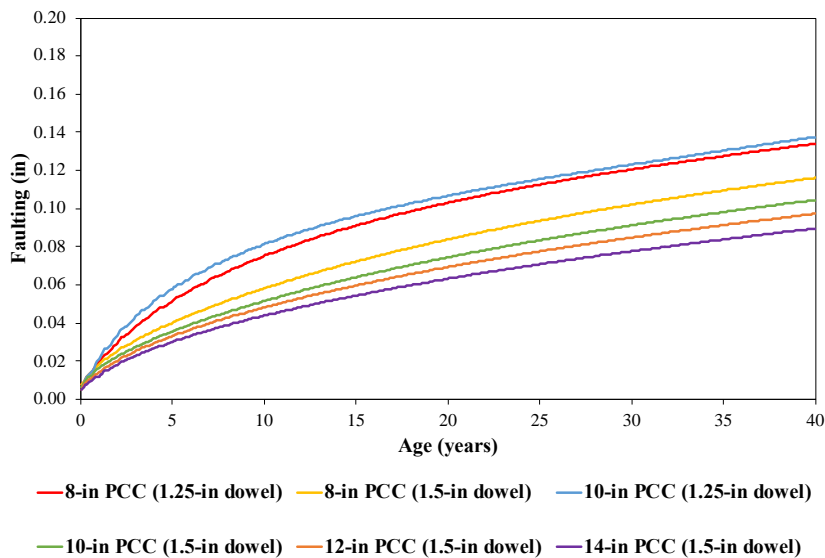


Figure 42 – Modified model faulting prediction for different slab thicknesses and dowel bar diameter

As anticipated, Figure 43 indicates that higher levels of faulting are expected in pavements with larger joint spacing. Stabilized bases results in smaller levels of predicted faulting than unbounded aggregate bases (Figure 44). The modified model predictions indicate a very similar faulting performance for pavements with CTPB and ATPB with a slight better performance of the latter.

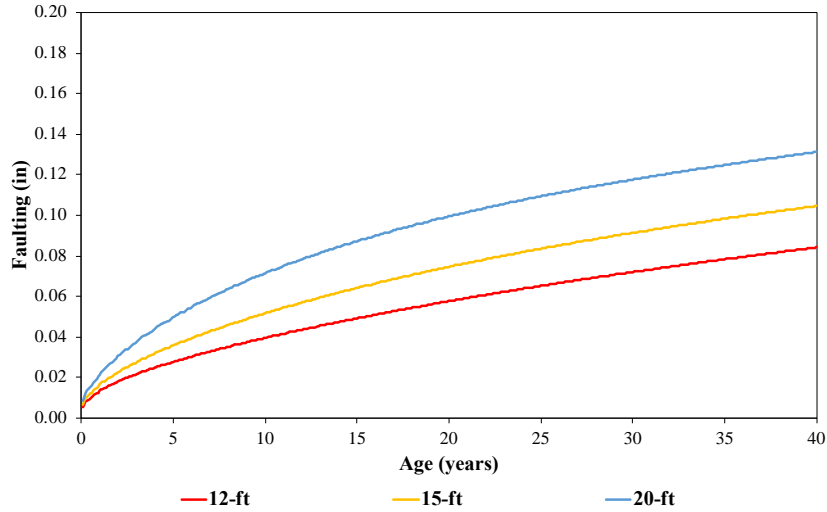


Figure 43 – Modified model faulting prediction for different joint spacing

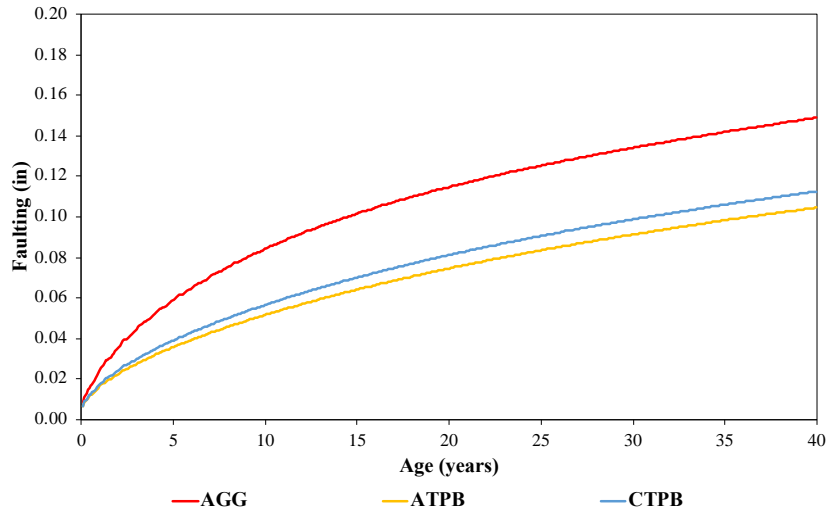


Figure 44 – Modified model faulting prediction for different pavement bases

### 3.3.3.1 Effect of high level of concrete coefficient of thermal expansion (COTE)

A sensitivity analysis was performed comparing faulting predictions using Pavement ME (PA Calibration coefficients) and the modified model developed under this research project. The faulting performance of 10-in thick JPCP with a 15-ft joint spacing, 1.5-in dowels, and an aggregate base was simulated. An AADTT of 5000 was assumed. Three levels of COTE were considered: low ( $4.5 \times 10^{-6}/^{\circ}\text{F}$ ), high ( $5.5 \times 10^{-6}/^{\circ}\text{F}$ ), and excessively high ( $6.5 \times 10^{-6}/^{\circ}\text{F}$ ). The results of the analysis are presented in Figure 45.

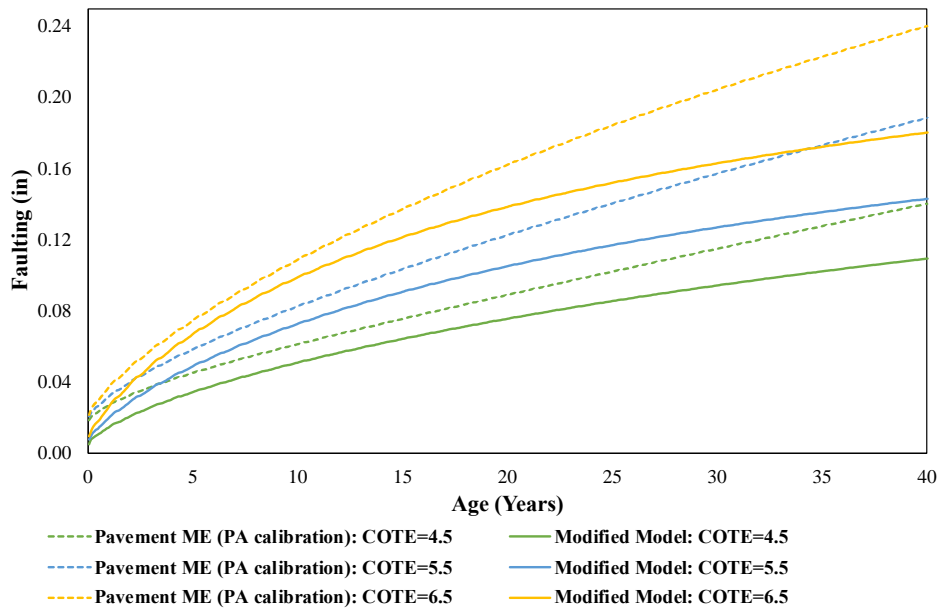


Figure 45 – Comparative COTE ( $10^{-6}$ ) sensitivity analysis of Pavement ME and Modified Model faulting predictions (95% reliability)

Although both Pavement ME and the modified faulting models predict an increase in the faulting level with an increase in the COTE, the modified model results in much less conservative faulting predictions than Pavement ME. The difference between the Pavement ME and modified faulting model predictions increases with an increase in pavement age. While the Pavement ME faulting model predicts unrealistically high faulting greater than 0.25 in after 40 years if the COTE is equal to  $6.5 \times 10^{-6}/^{\circ}\text{F}$ , the modified model predicts faulting less than 0.2 in for the same value of COTE. The same trend is observed for stabilized bases as shown in Figure 46. Therefore, it can be concluded that the modified model results in lower faulting predictions for JPCPs with a high COTE of concrete. Nevertheless, the model also indicates a higher risk of faulting development if concrete with high COTE is used.

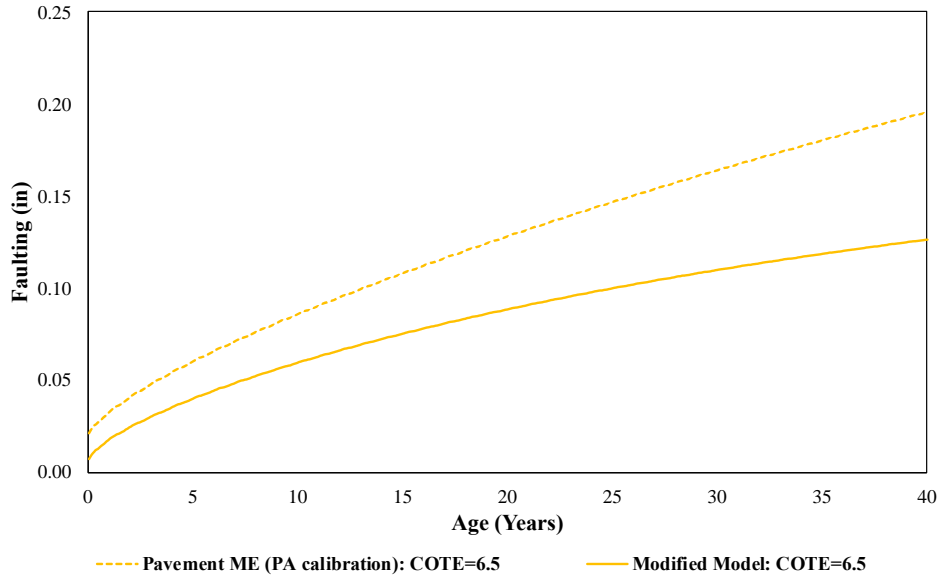


Figure 46 – Comparative excessively high COTE analysis of Pavement ME and Modified Model faulting predictions (95% reliability) using ATPB

It must be noticed that the hypothetical design above ignored cracking development. For a more realistic design, considering a 10 in thick slab (1.25 in dowels), the maximum allowable traffic so the project remains under a 10% cracked slab threshold (95% reliability) for 40 years would be 825 AADTT. As shown in Figure 47, the Pavement ME model design fails at around 32 years old considering an 0.12 in faulting threshold. This would require the designer to increase dowel diameter to 1.5 in dowel. PennDOT uses 1.25 in dowel diameter for 10 in thick JPCP slabs while Pavement ME recommends 1.5 in dowels for the same slab thickness. Using the modified model, the design is successful.

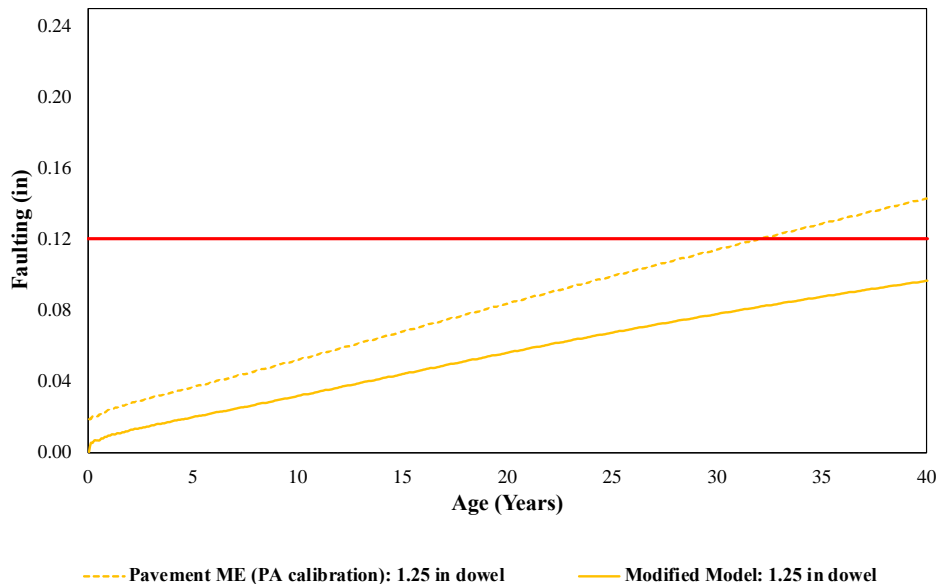


Figure 47 – Design comparison of Pavement ME and Modified Model faulting predictions (95% reliability) using ATPB

### 3.3.3.2 Effect of widened lanes

To evaluate the effect of the widened lane on the faulting models predictions, a comparison of faulting predictions for conventional (12 ft) and widened (14 ft) lanes was conducted. The analysis used two hypothetical cases composed of 10-in thick JPCP with a 15-ft joint spacing, and an aggregate base subjected to an Average Annual Daily Truck Traffic (AADTT) of 5000. Two dowel diameters were used: 1.25 in (PennDOT) and 1.5 in (Pavement ME). The COTE was assumed to be equal to  $5.5 \times 10^{-6}/^{\circ}\text{F}$ . The results of the predictions with the Pavement ME and modified model as shown in Figure 48. As expected, both Pavement ME and the modified model predicted much lower faulting for the widened lane. Predicted faulting for widened lanes pavements with 1.5 in dowels is minimal. Again, both hypothetical designs ignore cracking performance requirements.

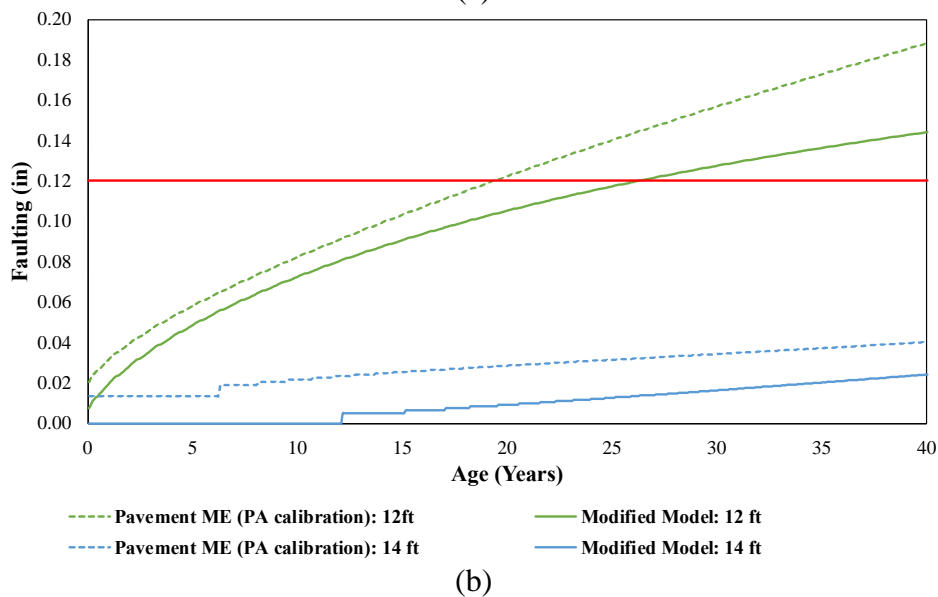
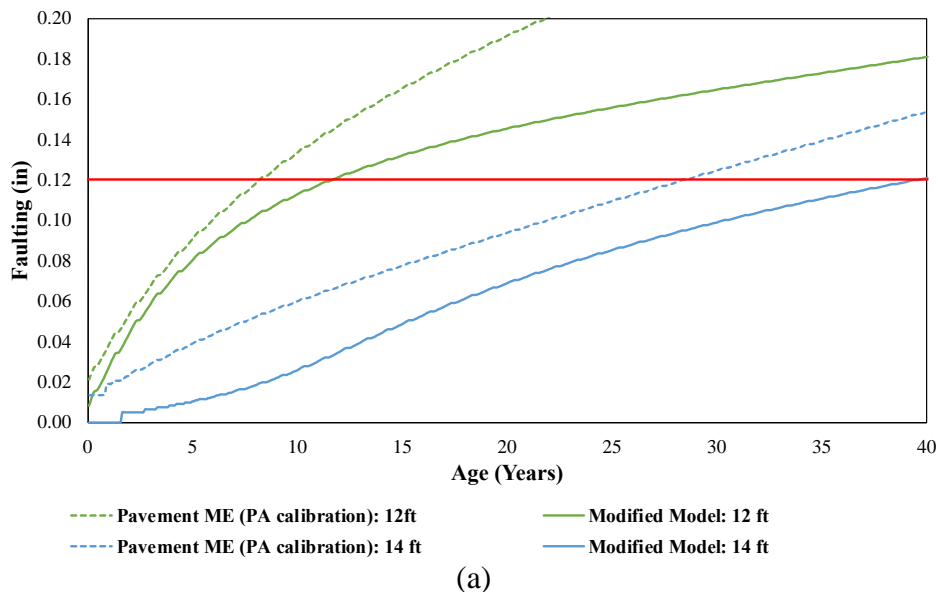
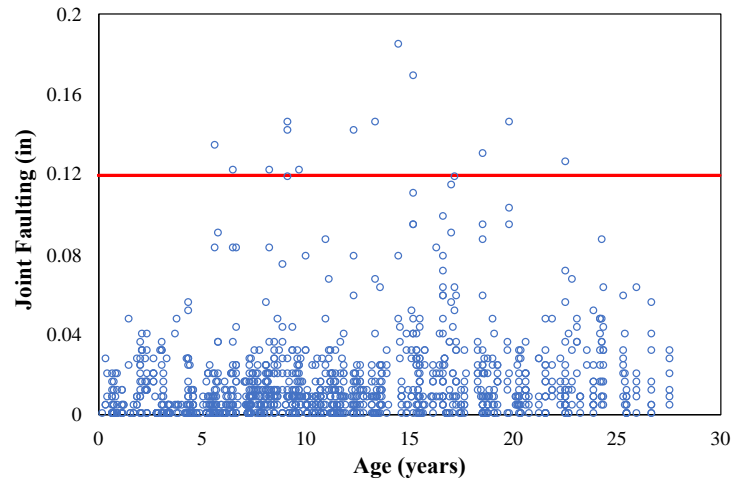


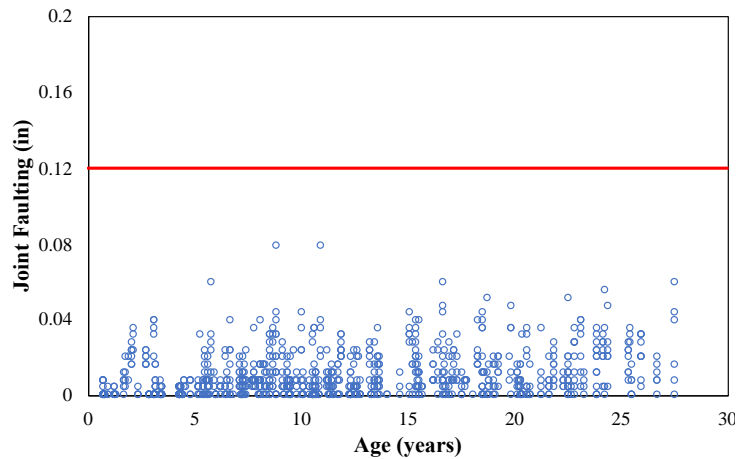
Figure 48 – Comparative lane width analysis of Pavement ME and Modified Model faulting predictions (95% reliability) using (a) 1.25 in and (b) 1.5 in dowels

From the 5800 faulting observations in the RMS database only 58 observations are attributed to sections with widened lanes and these sections have various design features, such as base types and traffic levels. Therefore, data was insufficient to perform model evaluation and modification considering this design feature. To address this limitation, we compared faulting performance of the doweled sections with and without widened lane using the FHWA Long Term Pavement Performance (LTPP) database.

Figure 49 shows faulting for LTPP sections from JPCP with various design features and site conditions. The presence of a widened lane significantly reduces a potential for faulting development. While several sections without a widened lane exhibited faulting greater than 0.12 in, the vast majority of the sections with a widened lane exhibited faulting of 0.05 in (1.25 mm) or less. This confirms the modified model prediction that the use of the widened lane and dowels leads to a low risk of reaching faulting level exceeding performance threshold of 0.12 in.



(a)



(b)

Figure 49 – LTPP data for JPCP constructed with (a) conventional lane width (10 to 12 ft), and (b) widened lanes (13 and 14 ft)



### 3.3.4 Design Examples

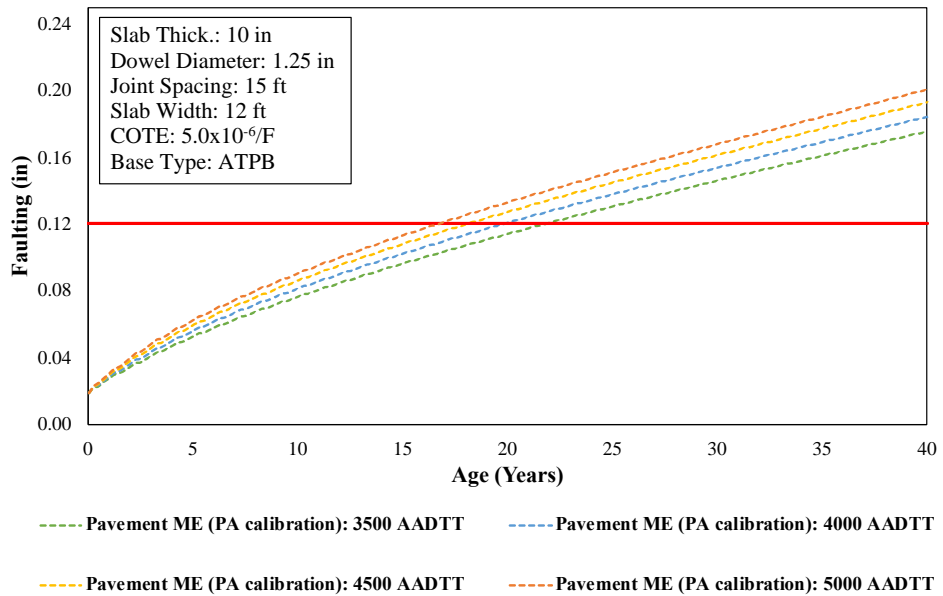
To demonstrate the main differences in faulting prediction between the current faulting model (Pavement ME – PA calibration) and the modified model, several design cases were analyzed. To provide more realistic design examples, the effect of cracking was also taken into account. The PCC slab thickness was designed so that the percentage of cracked slabs would remain below 10% with 95% reliability for the entire service life (40 years).

For conventional width (12 ft) JPCP, Figure 50 shows faulting development simulated using Pavement ME for several traffic levels (Design 1). For all these traffic levels, the cracking model resulted in the required slab thickness between 9.5 and 10 in, so the slab thickness was set to be 10 in. According to Pavement ME, if 1.25-in dowels are used, the project would fail before 20 years of service. Even with 1.5-in dowels, the project would barely meet the faulting performance requirement for the AADTT level of 4,000 trucks and cannot provide the required faulting performance for AADTTs of 4,500 and 5,000.

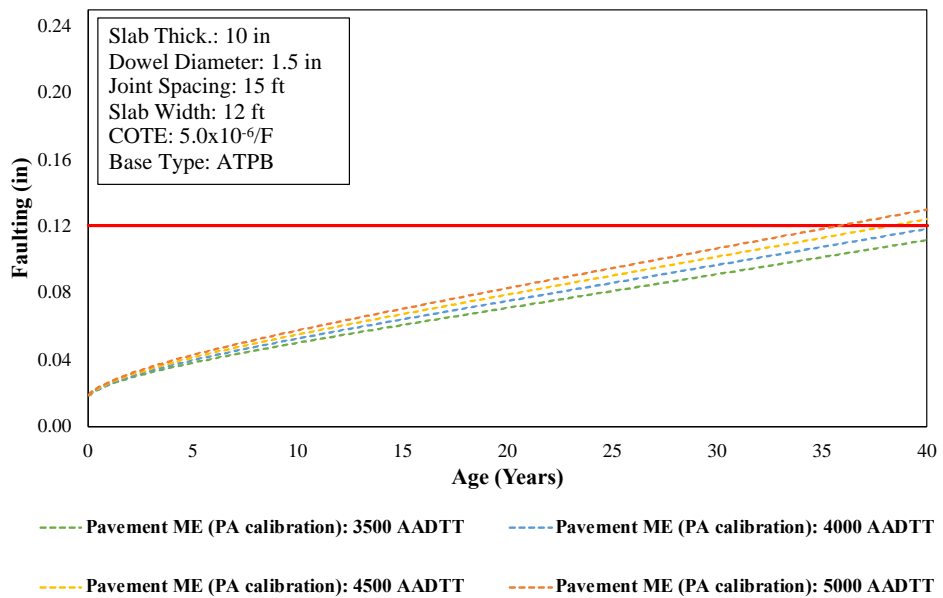
Conversely, using the modified model, the project is successful for all traffic levels with just 1.25 in dowels as shown in Figure 51. This example illustrates that the modified faulting model confirms that the current PennDOT dowel diameter practices – 1.25 in dowels for 10 in thick JPCP – are reasonable and may be used for the majority of designs. However, it is still important to conduct the performance prediction check and, if necessary, increase dowel diameter accordingly.

Another example, referred to as Design 2, has a moderate traffic level (2,000 AADTT, about 43 million total ESALs), higher COTE ( $5.5 \times 10^{-6}/^{\circ}\text{F}$ ), and an aggregate base. This design, with the use of 1.25-in dowels as specified by PennDOT for 10 in slabs, does not meet the faulting threshold criteria according to both Pavement ME and the modified (see Figure 52). Still, the modified model predicts that the project will reach the threshold level nine years later than it is predicted by Pavement ME. Increasing the dowel diameter to 1.5-in leads to satisfying the faulting threshold requirement according to the modified model. At the same time, according to Pavement ME, even 1.5-in dowels cannot provide an adequate performance with respect to faulting.

The differences in predictive performance are more evident for treated bases under a high traffic (8,000 AADTT – approximately 172 million ESALs total) which will be referred to as Design 3 (see Figure 53). In this case, an 11.5-in JPCP with 1.5-in dowels would fail after 22 years of service according to Pavement ME. The modified model predicts an adequate performance for more than 40 years.



(a)



(b)

Figure 50 - Faulting predictions for Design 1 using Pavement ME (PA calibration) with dowel diameter input of (a) 1.25 in and (b) 1.5 in

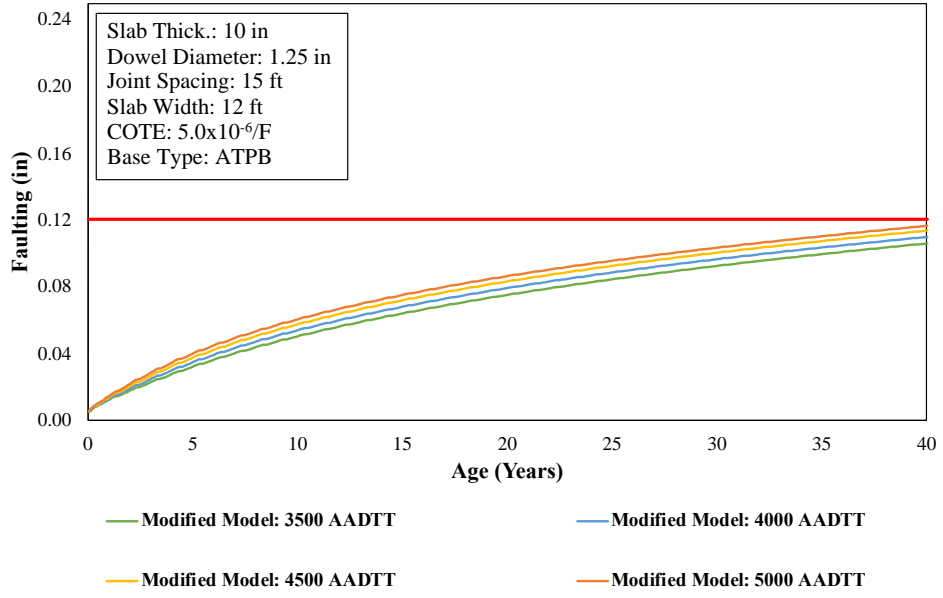


Figure 51 - Faulting predictions for Design 1 using the modified model

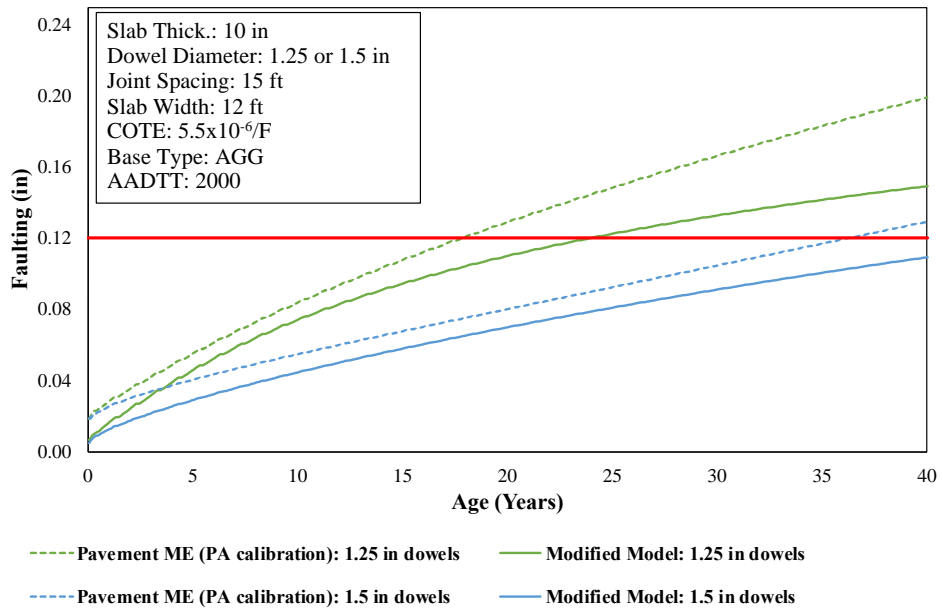


Figure 52 - Comparative faulting predictions for Design 2 with two dowel diameters

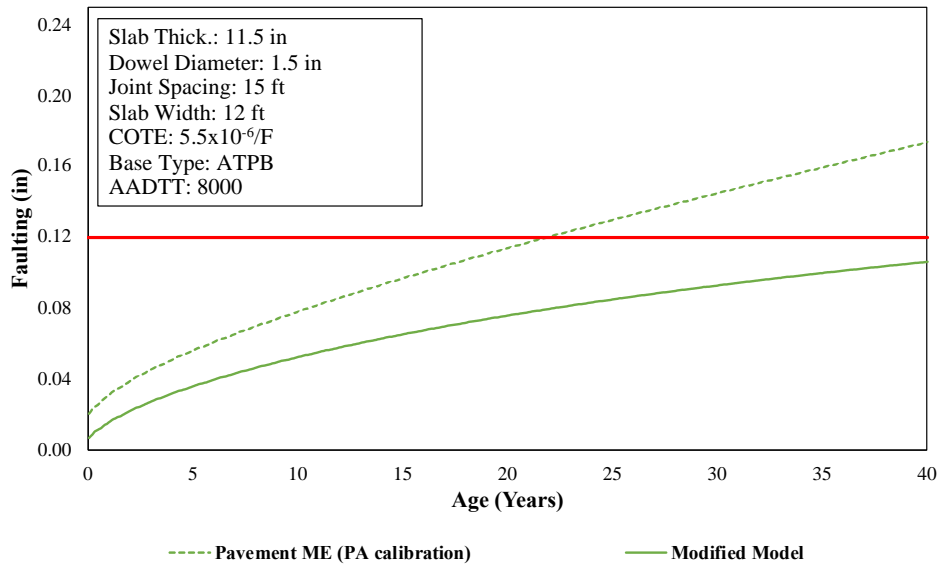


Figure 53 – Comparative faulting predictions for Design 3

Figure 54 presents performance prediction for a project with a widened lane subjected to high traffic (8,500 AADTT – approximately 182 million ESALs total) referred as Design 4. The use of 1.0-in dowels is insufficient to keep faulting below the 0.12-in threshold. Pavement ME predicts that if 1.25-in dowels are used then the project would reach the threshold in 39 years whereas the modified model predicts an adequate performance even after 40 years. Both models predict a very low faulting if 1.5-in dowels are used.

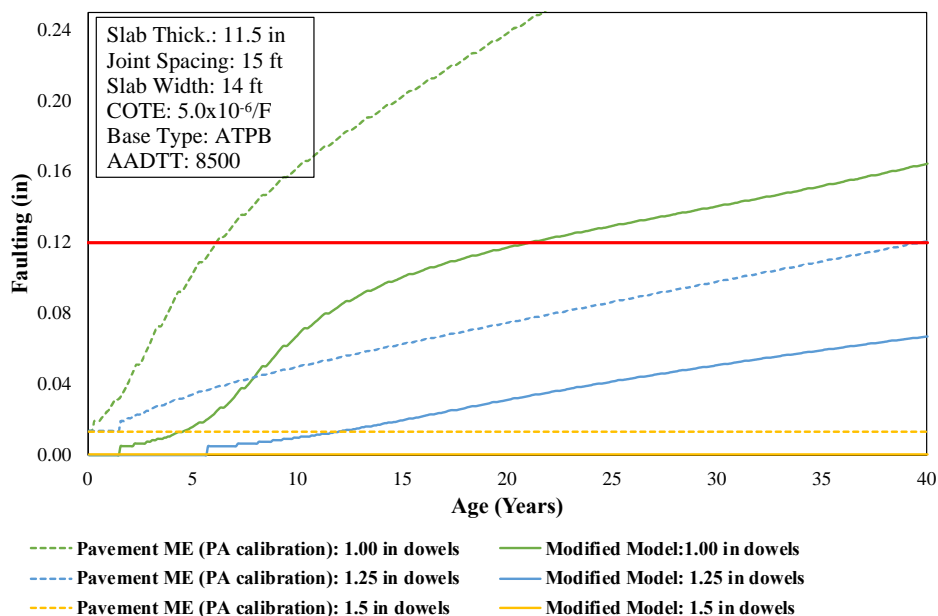


Figure 54 – Comparative faulting predictions for Design 4 using different dowel diameters

## **4 CHAPTER 3: FAULTING MODEL FOR BCOA**

This chapter provides a summary of the development of the faulting model for BCOA in four main steps: (a) assembly of a BCOA database, (b) development of the structural model, (c) development of the framework for the faulting prediction model, and finally (d) model calibration.

The evaluation of faulting in BCOA pavements is a two-step process. In the first step, a structural response model is used to estimate the response of the pavement (response for specified material properties and thicknesses) to traffic and environmental loading. In the present study, the response used is the difference in deflection basins between loaded and unloaded slabs. Damage is accumulated over time through the differential energy generated based on the difference between these deflection basins. The differential energy is then used in an empirical faulting prediction model. The parameters of this model are selected based on measured data from several field sections, as well as through engineering judgment. Finally, the predicted faulting is adjusted to account for uncertainty in the field. Thus, a comprehensive model to predict faulting in BCOA was developed. This chapter discusses each of these steps and presents results from the calibration.

### **4.1 Calibration Sections**

The calibration database used to calibrate the BCOA faulting model consists of 34 sections from five different states within the United States: Colorado, Illinois, Louisiana, Minnesota, and Missouri. The calibration sections are comprised of 18 sections at MnROAD, eight sections across the state of Minnesota, five sections in Colorado, and one section for each Illinois, Louisiana, and Missouri. Initially, the calibration was limited to only sections within the state of Minnesota due to limited performance data from other locations. However, an ongoing National Cooperative Highway Research Program (NCHRP) study 1-61, "Evaluation of Bonded Concrete Overlays on Asphalt Pavements," aided in supplementing the calibration database. Although these sections only included one measurement of faulting, it was important to be able to include sections within the calibration dataset from outside of Minnesota.

The calibration sections were divided into two sets. In one set, the depth of joint activation was through the PCC and in the other set the joint activated through both the PCC and asphalt layer. The depth of joint activation was established using an extensive amount of FWD data and the details can be found in DeSantis et al. [18]. For sections that developed both depths of joint activation, the joints that activated full-depth were separated from the joints that activated only through the PCC. This created two sections, one with joints activating only through the PCC and the other with joints activating full-depth. Two separate calibrations needed to be conducted in order to account for the different trends in faulting due to the different depths of joint activation. Table 12 presents a range of values in the calibration data set for the more sensitive parameters. Of the sections, 29 are undoweled while the rest are doweled. The dowel diameter for the doweled sections were all 1 in. If the pavement section has a random joint spacing, the mean joint spacing was used in the analysis. Considering the number of time series observations available, a total of 269 data points were available for calibration of the model.

The age of the sections ranged from approximately 3 to 27 years with an average of 10.4 years of age. In terms of ESALs, the traffic ranged from approximately 0.1 million to 20 million with an average of around 5 million ESALs. Detailed information for each calibration section can be found in Appendix A. Some available sections were removed from the calibration database due to performance related distress that influenced the magnitude of faulting. Cell 96 with full-depth joints was eliminated due to severe joint deterioration at these joints. In addition, if diamond grinding was performed on a given calibration section, the survey date and data prior to diamond grinding was used for calibration. Once diamond grinding was performed on a section, the remaining life and faulting data measurements were discarded from calibration.

Table 12 – Range of parameters for calibration sections.

<b>Parameter</b>	<b>Minimum</b>	<b>Maximum</b>	<b>Average</b>
Age, yrs.	3.0	27.0	10.4
Estimated ESALs	9.06E+04	1.91E+07	5.10E+06
Average joint spacing, ft	4	15	6
Overlay thickness, in	3	8	5
Overlay EMOD <sup>1</sup> , psi	3.60E+06	5.02E+06	4.40E+06
Overlay MOR <sup>2</sup> , psi	507	902	685
Overlay cement content, lbs.	400	650	500
Existing asphalt thickness, in	3	16	8

<sup>1</sup>EMOD is the elastic modulus of the PCC

<sup>2</sup>MOR is the modulus of rupture of the PCC

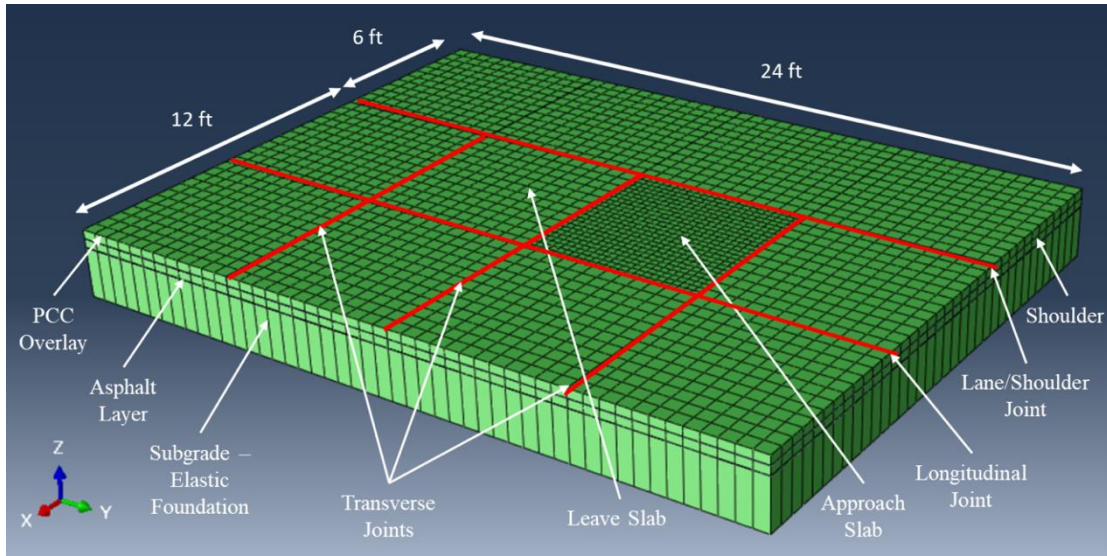
## 4.2 Develop Structural Model and Artificial Neural Networks

A new computational model was developed in the finite element modeling software, ABAQUS, that accurately predicts the displacement response of the BCOA to traffic and environmental loading conditions. The accuracy of this model was validated using FWD data collected from in-service BCOA structures. ABAQUS was selected as the FEM program because it is able to more accurately represent the response of a BCOA, specifically in the vicinity of the joint where the depth at which the joint will activate can vary. ABAQUS can model both a continuous asphalt layer as well as a discontinuous layer when the joint activates full-depth. In addition, a temperature gradient can be applied to quantify the effects of curling by applying a temperature difference to the top and bottom of the PCC layer, and achieving convergence is not problematic. The results from the ABAQUS analyses are used to populate a database of the critical response for both the loaded and unloaded side of the joint for a wide variety of BCOA structures. This database is then used to develop predictive models, consisting of systems of artificial neural networks, so the critical response for both the loaded and unloaded side of the joint can be determined in a rapid manner within the design process.

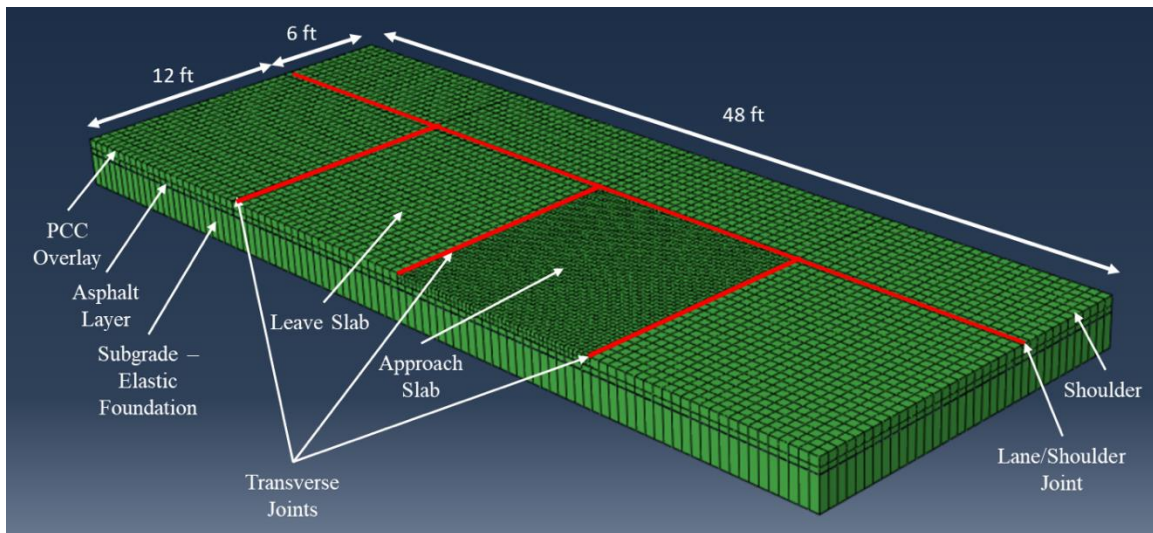
### 4.2.1 Computational Models

The computational models consist of at least one full lane width; an 8-slab system was used for partial lane width panels (6 ft by 6 ft and 8 ft by 8 ft) and a 4-slab system was used for full lane

width panels (12 ft by 12 ft and 10 ft by 10 ft). The 8-slab system consists of two adjacent panels in the transverse direction and 4 panels in the longitudinal direction. The 4-slab system consists of four full lane width panels in the longitudinal direction. The effects from the adjacent lane were negligible for the full lane width panels, due to the critical response location being the interior corner. Therefore, a single lane was used. Both slab systems include a shoulder that is 6 ft wide and is either tied PCC or asphalt. Figure 55 presents the 3-D FEM model.



a) 8-slab system: 6 by 6 ft panels



b) 4-slab system: 12 by 12 ft panels

Figure 55 – Model configuration

It may be noted that the structural model and subsequent faulting model were only developed for medium- and large-sized slabs. With short-sized slabs (joint spacing  $\leq 4.5$  ft), the wheelpath is typically very near or collinear with a longitudinal joint. This makes it more difficult to quantify

the effects of loads on the development of faulting without a significant amount of performance data specifically for sections with the smaller slabs. Since this data does not currently exist, the focus was to develop faulting prediction models for BCOA with medium and large slab sizes. Also, most of these smaller size slabs exist as part of an ultra-thin overlay constructed in areas with lower truck traffic. These types of structures most commonly fail as a result of fatigue cracking or the slabs shifting and not faulting.

#### 4.2.1.2 Interface Between Layers

The interface between the PCC (elastic solid) layer and the asphalt (elastic solid) layer was fully bonded. Composite action is essential for the performance of BCOA. This was achieved by using a “Tie” constraint, which treats adjacent nodes as rigidly connected to one another at the interface between the PCC and asphalt layers [19]. However, when a joint only activates through the PCC layer and the asphalt layer remains continuous beneath the joint, differential deflections between the approach and leave slabs are negligible. Therefore, the response of in-service BCOAs could be more accurately modeled by creating a debonded region near the joint when a joint only activates through the PCC layer. This debonded region facilitates the development of the differential deflections necessary for pumping, thus allowing faulting to develop. A 6-in region around the edges of both the approach and leave slab was modeled as unbonded, while the interior portion of the slabs maintained a full bond. The unbonded region was modeled using a tangential behavior interaction. This interaction uses a “Penalty – Friction” assignment and is defined such that no shear forces develop, and the contact surfaces are free to slide [19]. The debonded region can be seen in Figure 56. A dense liquid foundation beneath the asphalt was simulated using a “Linear” interface interaction with a rigid fully constrained body [19]. This allows the asphalt to become unsupported unlike the “Foundation” support interaction in ABAQUS [19]. The stiffness of the interaction is defined by a modulus of subgrade reaction, k-value (psi/in).

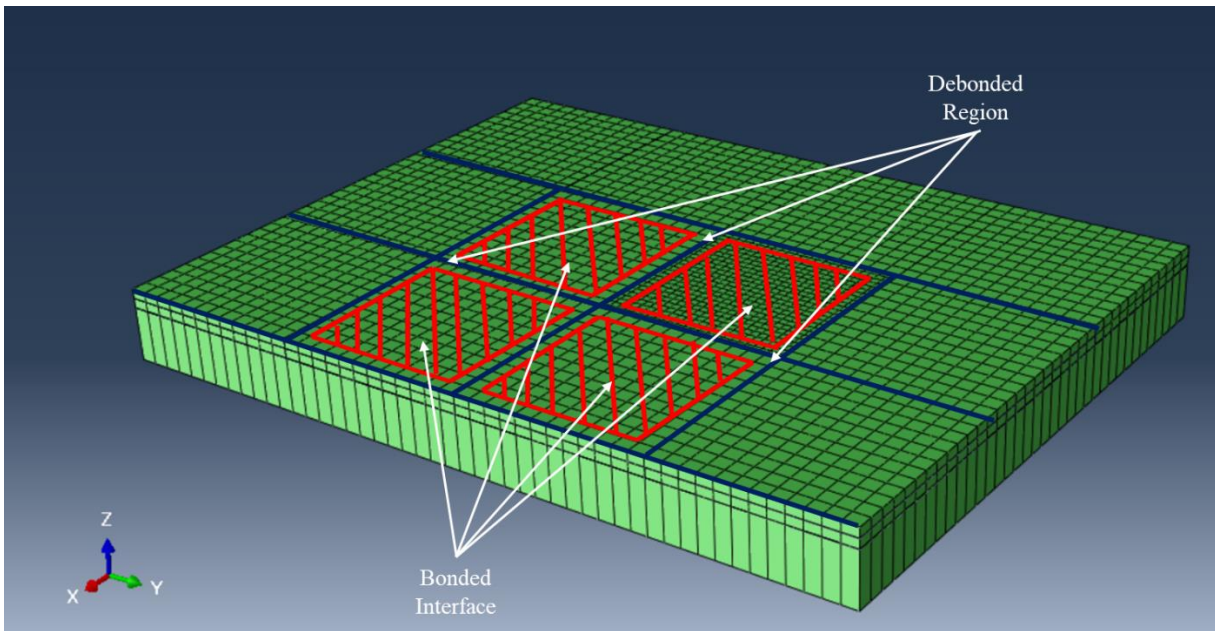


Figure 56 – Debonded region at the interface for the 8-slab system (PCC depth only)



#### 4.2.1.3 Joints

The joints are another important feature in the BCOA that must be accurately captured in the computational model. When joint activation through the asphalt is expected, the asphalt layer is discontinuous at the transverse joint and no interaction is assumed within the asphalt layer across adjacent slabs. When the joint activates only through the PCC layer for the 8-slab system, the asphalt is modeled as a continuous layer beneath all transverse joints. When the 8-slab system is used to model a full-depth joint, the central transverse joint is modeled to go through both the PCC and the asphalt layers but all other transverse joints are assumed to only activate through the PCC layer. For the 4-slab system, all transverse joints were modeled as full-depth joints. These joints are likely to activate full-depth because the 4-slab system is used for modeling BCOAs with longer panels that have larger joint width movement and thicker overlays with a high FSR. These assumptions on joint activation were based on an extensive study that was performed to better understand joint performance in BCOAs [20]. The asphalt remains continuous for both joint depths for all longitudinal joints within the driving lane. However, the asphalt layer is not continuous across the lane/shoulder joint.

Aggregate interlock across the PCC joints is addressed by using shear springs. The spring stiffness per unit area is calculated for a given LTE based on the following equation developed by Croveti [21].

$$AGG^* = \left( \frac{1}{\frac{LTE}{0.012} - 0.01} \right)^{-1/0.849} \quad (49)$$

where:

$AGG^*$  is the non-dimensional joint stiffness of the transverse joint;

$LTE$  is the corresponding LTE to the assigned joint stiffness.

The stiffness of the individual springs is calculated based on the tributary area. The longitudinal joints in the driving lane are modeled with the same LTE as the defined LTE for the transverse joints. The lane/shoulder joint is defined as 90% LTE when it is a tied PCC shoulder, and 0% when it is an asphalt shoulder. For both shoulder conditions, the asphalt layer is not continuous across the lane/shoulder joint and is assumed to provide no support. The full-depth asphalt shoulder is also assumed to provide no support. A “Hard” contact surface interaction is also applied to all joint faces to allow compression at the joint faces if they come into contact with each other.

#### 4.2.1.4 Wheel and Thermal Loads

Loading is performed in two steps: thermal loading and traffic loading. In the first step, an equivalent linear temperature gradient (ELTG) is applied, which accounts for curling due to temperature gradients, drying shrinkage, and built-in curl. The ELTG is applied by defining nodal temperatures at each of the five layers of nodes in the PCC slab. The temperature at the bottom of the PCC is set to 0°F. The ELTG varies linearly from the bottom to the top of the PCC. All nodes in the asphalt layer are set to 0°F. In the second step, traffic is applied as a uniform pressure evenly

distributed over the tire footprint. Single and tandem axle loads were considered. The dual tire footprint can be seen in Figure 57.

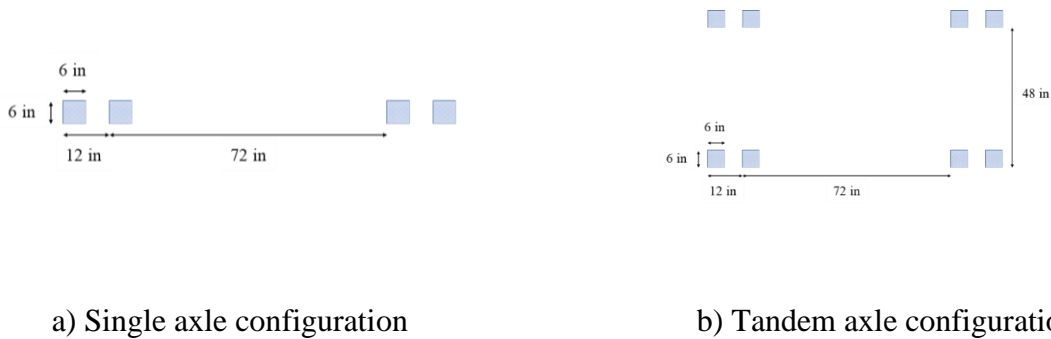


Figure 57 – Axle configuration

#### 4.2.1.5 Finite Element Mesh

An accurate prediction of structural response is dependent on using an appropriate FEM mesh in the computational models. Quadratic brick elements have been shown to be able to predict pavement behavior well [22]. Twenty node quadratic brick elements (C3D20) were used in ABAQUS. These elements are similar to elements used in pavement specific FEM, such as EverFE [23]. This node configuration has been shown to provide a high level of accuracy, along with an acceptable computational time demand [24].

The mesh size was selected based on the results of a mesh convergence study. Both depths of joint activation were examined with different mesh fineness. Two structures were examined for both the 6-ft panel size and 12-ft panel size models. Table 13 presents the different structures examined in the convergence study. Mesh convergence was achieved using 3 in by 3 in by half of the layer thickness for the loaded slab, and 6 in by 6 in by the layer thickness for the remainder of the models. Since second-order elements are used, one element along the thickness for each layer is sufficient for modeling flexure [24].

Table 13 – Mesh convergence study parameters.

<b>Joint Depth</b>	<b>Panel size, L x W ft</b>	<b>PCC thickness, in</b>	<b>Asphalt thickness, in</b>	<b>Modulus of subgrade reaction, psi/in</b>
PCC only	6 x 6	3	7	100
PCC only	6 x 6	3	7	315
PCC only	6 x 6	5	7	100
PCC only	6 x 6	5	7	315
PCC only	12 x 12	3	7	100
PCC only	12 x 12	3	7	315
Full-depth	12 x 12	6	7	100
Full-depth	12 x 12	6	7	315

#### 4.2.1.6 Model Validation

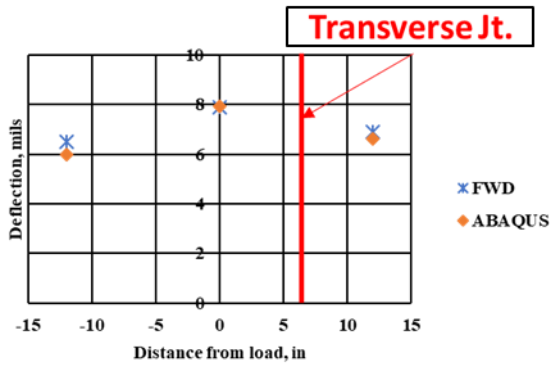
It is essential that the computational model accurately predicts the pavement response. To validate the FEM model, five test sections from two testing facilities were used. Three BCOA sections from MnROAD, Cells 60, 96, and 97, and two sections from the University of California Pavement Research Center (UCPRC) Heavy Vehicle Simulator (HVS) test sections, Sections B and F, were used. The parameters used for the validation sections can be seen in Table 14. The parameters for the MnROAD sections were obtained from construction reports and research summary publications [25-30]. The asphalt stiffness at the time of the FWD testing was established using a mastercurve derived with laboratory data and temperatures measured from thermocouples embedded at mid-depth in the asphalt layer. FWD testing at mid-slab was used to backcalculate the k-value of the subgrade. The parameters corresponded well with previous research conducted on the BCOA sections at MnROAD [26-30]. The asphalt stiffness for the UCPRC sections was estimated using FWD and laboratory test data to develop mastercurves at a frequency of 20 Hz, based on the loading rate of the HVS.

Table 14 – Pavement parameters for validation sections.

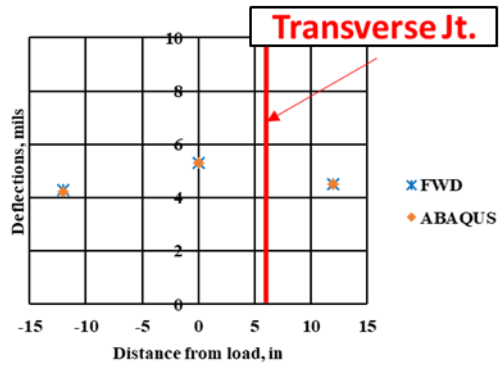
Parameter	Cell 60	Cell 96	Cell 97	Section B	Section F <sup>1</sup>
PCC thickness, in	5	6	6	4.5	4.5
Asphalt thickness, in	7	7	7	4.5	1 (RHMA) 3.5 (HMA)
PCC modulus of elasticity, 10 <sup>6</sup> psi	4.6	4.7	4.7	7.54	7.54
Modulus of subgrade reaction, k-value psi/in	315	315	315	720	720
Asphalt modulus of elasticity, 10 <sup>6</sup> psi	0.35	0.90	0.35	0.475	0.95 (RHMA) 0.55 (HMA)
Asphalt testing temperature, °F	90	68	90	95	85
Asphalt testing load frequency, Hz	25	25	25	20	20
Panel size, L x W ft	5 x 6	5 x 6	10 x 12	6 x 6	6 x 6

<sup>1</sup>Section F consisted of a 1-in newly placed rubberized hot-mixed asphalt (RHMA) layer on top of an older 3.5-in HMA layer.

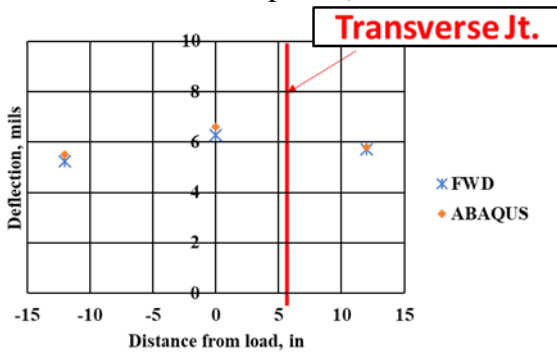
Figure 58 presents the deflections measured with the FWD and predicted from the computational model as a 9-kip load is applied in the outer wheelpath adjacent to the transverse joint. Section B at UCPRC was tested using a 13.5-kip FWD load. The temperatures at the time of loading was considered in the analysis with respect to the asphalt stiffness and temperature gradients within the PCC overlay. For Cell 60, the asphalt layer was expected not to be continuous through the joint. For Cell 96, the asphalt layer was expected to be continuous underneath the joint in the overlay. For Cell 97, both depths of joint activation are expected. Early in the service life, the asphalt layer is likely still continuous and later in the service life the asphalt layer is not. The presumed depth of joint activation for the MnROAD cells were based on measured deflections from FWD testing. For Sections B and F, the asphalt is likely continuous during the time of testing based on measured deflections and visual inspection. From these plots, it is evident that the computational models can accurately predict the response of the in-service BCOA structures to applied loads.



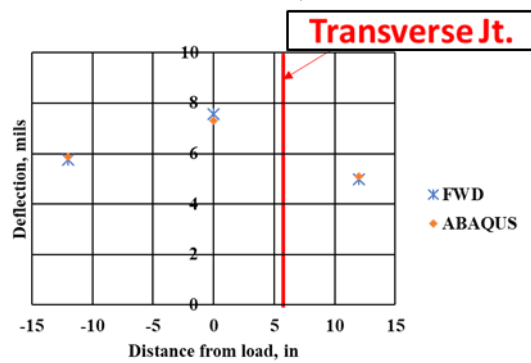
a) Cell 60: Not-continuous asphalt (9-kip load)



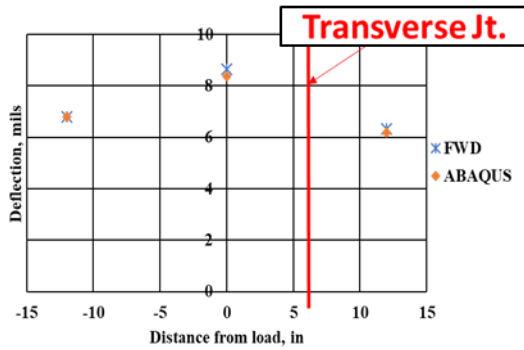
b) Cell 96: Continuous asphalt (9-kip load)



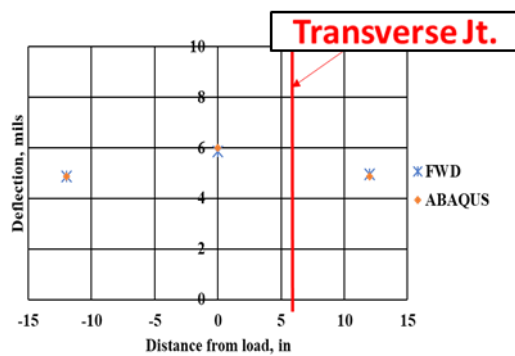
c) Cell 97: Continuous asphalt (9-kip load)



d) Cell 97: Not-continuous asphalt (9-kip load)



e) Section B: Continuous asphalt (13.5-kip load)



f) Section F: Continuous asphalt (9-kip load)

Figure 58 – Model validation

#### 4.2.2 Artificial Neural Network Response Prediction Models

Performing a computational analysis of all combinations of loading configurations and environmental conditions throughout the analysis periods for faulting is computationally prohibitive. Therefore, the use of ANNs is beneficial to produce responses rapidly, similar to the methodology employed in Pavement ME and the linear regression stress prediction models in the BCOA-ME [1, 16, 25, 31, 32].

##### 4.2.2.1 Critical Response Parameters

The critical responses from the structural model are to be used to calculate the differential energy of subgrade deformation, shown in Equation 50. The critical response to be obtained from the computational model is the deflection basin on the approach and leave slab after the environmental loading step and the traffic loading step. The deflection basin is defined as 2 ft long by 6 ft wide on both sides of the transverse joint, adjacent to the lane/shoulder joint. The volume of the deflection basin is calculated as the sum of the nodal deflections in the basin multiplied by the tributary area corresponding to the nodes. The same number of nodal deflections are used for the approach and leave slab basins. The deflection basin can be seen in Figure 59. When the joint depth is through the PCC only, the response is recorded at the bottom of the PCC layer. When the joint is full-depth, the response is recorded at the bottom of the asphalt layer. In Pavement ME, the critical responses to determine differential energy for concrete pavement design are the deflections at the corners on both the loaded (approach slab) and unloaded (leave slab) sides of the joint [1, 16]. In the present model, a 2 ft by 6 ft deflection basin was selected to characterize the pavement response in lieu of the more traditionally used corner deflection. A 2019 study showed the deflection basin better correlates with predicted deflection as compared to corner deflections [33]. This basin size also accommodates the 6 ft by 6 ft slab size, which is commonly used in overlay design. A fractional factorial of FEM analyses was performed to generate a database of whitetopping responses to a range of traffic and environmental loading conditions. The established critical response, along with corner deflections, were obtained for each analysis to train the ANNs [34]. The selection of this basin area also provided an improved accuracy between predicted and measured performance during the calibration process.

$$DE = \frac{1}{2}k(B_L^2 - B_{UL}^2) \quad (50)$$

where:

- $DE$  is the differential energy of subgrade deformation, lb-in;
- $k$  is the modulus of subgrade interaction, psi/in;
- $B_L$  is the deflection basin on the loaded slab, in<sup>2</sup>;
- $B_{UL}$  is the deflection basin on the unloaded slab, in<sup>2</sup>.

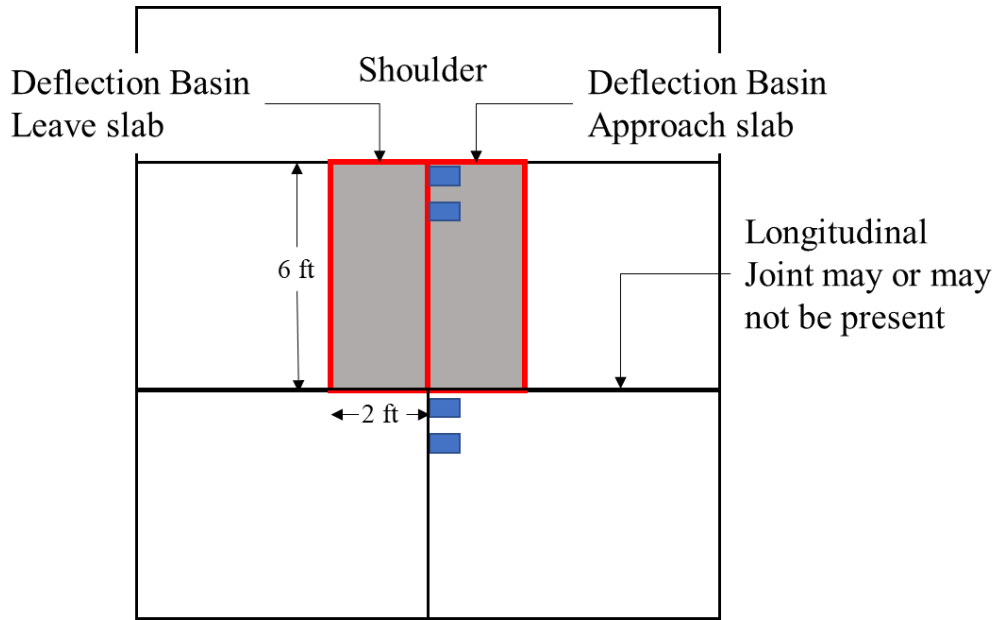


Figure 59 – Deflection basin definition

An accurate predictive model requires the computational model be analyzed over an inference space with 10 parameters. A database to be used in developing the ANNs is populated by using the computational models to evaluate these 10 parameters for a large range of values. All parameters considered, along with their corresponding values, can be seen in Table 15. A full factorial would result in a total of approximately 105,000 FEM analyses. In order to account for the different joint depths, there are 18 possible combinations examining joint depth, PCC thickness, and asphalt thickness. However, only 12 of these combinations are feasible based on the FSR established by DeSantis et al. [18]. Three structures are analyzed with a joint that activated through the PCC, three more with a full-depth joint, and an additional three considering both joint activation depths separately, resulting in 12 combinations. This reduces the total number of analyses to 23,328 per joint spacing for the partial lane width panels and 11,664 for the large panels because only full-depth joint activation is considered for the large panels. To further reduce the number of analyses required, a fractional factorial is used [35]. Additional analyses were not performed to account for the three level of asphalt stiffness. Instead, each level of asphalt stiffness (low, medium, or high) is assigned to one third of the analyses in a full factorial of the other parameters. This reduces the required number of analyses by two thirds. The total amount of FEM analyses conducted in ABAQUS is 19,440 (7,776 analyses for each of the partial lane width panels, and 3,888 analyses for the full lane width panels) using the fractional factorial design.

Table 15 – Overall design matrix.

<b>Joint activation depth</b>	<b>PCC only</b>	<b>PCC &amp; Asphalt (0% LTE through Asphalt)</b>	
<b>PCC thickness (in)</b>	3.5	5.5	8
<b>PCC modulus of elasticity (psi)</b>	4.0E+06		
<b>PCC Poisson's ratio</b>	0.18		
<b>PCC CTE (in/in/°F)</b>	5.5E-06		
<b>PCC joint spacing (ft)</b>	6	8	12
<b>PCC temp. difference (°F)</b>	-12, -6	0	24
<b>Asphalt thickness (in)</b>	3.5	5.5	7.5
<b>Asphalt modulus of elasticity (psi)</b>	1.0E+05	8.0E+05	3.0E+06
<b>Asphalt Poisson's ratio</b>	0.35		
<b>Modulus of subgrade reaction, k-value (psi/in)</b>	100	250	400
<b>Shoulder width (ft)</b>	6		
<b>Lane shoulder LTE (%)</b>	0 (Asphalt)	90 (Tied PCC)	
<b>Transverse joint LTE (%)</b>	50	70	95
<b>Wheel wander (in)</b>	0	6	18
<b>Single axle (kip)</b>	18	30	
<b>Tandem axle (kip)</b>	36	60	

#### 4.2.2.2 Development of Artificial Neural Networks

The ANNs are developed to predict the deflection basins for both the loaded and unloaded side of the joint. To train and test the ANNs using the factorial of analyses, the neural network toolbox in MATLAB® was used [36]. ANNs were established to be able to rapidly predict the critical response of a given whitetopping structure to be used to determine DE, as well as the joint shear capacity. These ANNs were established to predict the deflection basins for both the approach and leave side of the joint. In order to reduce the number of prediction models and to reduce the prediction variability between the different ANNs, the output of each ANN is the difference between the deflections on the approach (loaded) slab and the leave (unloaded) slab (basins and corners). This decreases the likelihood of an erroneous difference in prediction for the loaded and unloaded slabs (instead of two outputs, there is only one). Therefore, a total of 15 ANNs were trained, of which 10 ANNs were for partial lane-width panels, and 5 were for full-lane width panels; 6 ANNs for the deflection basins, 6 ANNs for corner deflections, and 3 ANNs for corner deflections based on temperature effects alone. These ANNs are separated into panel size based on the likelihood of the joint activation depth, axle type, and temperature loading. Due to symmetry of the temperature loading condition, only one ANN is necessary for both the loaded and unloaded sides of the joint [37]. The primary calculation for each month is to determine the DE, which can be found using Equations 51 and 54. The corner deflections due to traffic and



environmental loading conditions are also used directly in the calculation of monthly incremental faulting and are evaluated from Equations 52 and 53 respectively.

$$\Sigma\delta_{B,A,m} = ANN_{\Sigma B,A,JD}(JTSpace, l_{eff}, q_i^*, k, \frac{AGG}{k * l_{eff}}, LTE_{shoulder}, s, \Phi) \quad (51)$$

$$\Sigma\delta_{C,A,m} = ANN_{\Sigma C,A,JD}(JTSpace, l_{eff}, q_i^*, k, \frac{AGG}{k * l_{eff}}, LTE_{shoulder}, s, \Phi) \quad (52)$$

$$\Sigma\delta_{C,T,m} = ANN_{\Sigma T,JD}(JTSpace, l_{eff}, 0, k, \frac{AGG}{k * l_{eff}}, LTE_{shoulder}, 0, \Phi) \quad (53)$$

$$DE_m = \sum_1^A \sum_1^j \sum_1^i \left(\frac{1}{2}k \left(\sum \delta_{B,A,m}\right) * WWpr_i * load_{A,j}\right) \quad (54)$$

Where:

$\Sigma\delta_{B,A,m}$  is the basin sum deflection for the difference between the loaded and unloaded slab for axle type A (A=1 for single; A=2 for tandem) for month  $m$ , in.

$\Sigma\delta_{C,A,m}$  is the corner deflection for the difference between the loaded and unloaded slab for axle type A (A=1 for single; A=2 for tandem) for month  $m$ , in.

$\Sigma\delta_{C,T,m}$  is the corner deflection for the loaded slab due to environmental loading only for month  $m$ , in.

$ANN_{\Sigma B,A,JD}$  is the ANN output for the difference between the squared sum of the 2-ft by 6-ft deflection basin for the loaded slab and the squared sum of the 2-ft by 6-ft deflection basin for the unloaded slab for axle type A (1 for single and 2 for tandem) and joint activation depth JD (0 for PCC only and 1 for full-depth), in<sup>4</sup>.

$ANN_{\Sigma C,A,JD}$  is the ANN output for the difference between the corner deflection on the loaded slab and the unloaded slab for axle type A (1 for single and 2 for tandem) and joint activation depth JD (0 for PCC only and 1 for full-depth), in.

$ANN_{\Sigma T,JD}$  is the ANN output for the corner deflection for the condition when only temperature is present for joint activation depth JD (0 for PCC only and 1 for full-depth), in.

$JTSpace$  is the joint spacing of the overlay, in.

$l_{eff}$  is the effective radius of relative stiffness of the overlay [38], in.

$q_i^*$  is the adjusted load/pavement weight ratio as defined below.

$k$  is the modulus of subgrade reaction, psi/in.

$\frac{AGG}{k * l_{eff}}$  is the nondimensional joint stiffness.

$LTE_{shoulder}$  is the L/S joint load transfer efficiency (LTE), %.

$s$  is wheel wander offset from the lane/shoulder (L/S) joint, in.

$\Phi$  is Korenev's non-dimensional temperature gradient as defined below.

$DE_m$  is the differential energy density deformation accumulated for month  $m$ , lb-in.

$WWpr_i$  is wheel wander distribution over the number of bins  $i$ , in.

$load_{A,j}$  is the number of axles of axle type  $A$  at each load level  $j$ , where  $A$  is either a single or tandem axle, lb.

$$q_i^* = \frac{P_i}{A \gamma_{eff} h_{eff}} \quad (55)$$

where,

$P_i$  is the axle load, lb.

$A$  is the axle type parameter (1 for single axle and 2 for tandem axle).

$h_{eff}$  is the effective thickness of the pavement, in.

$\gamma_{eff}$  is the effective unit weight of the pavement, pci.

$$\Phi = \frac{2\alpha_{PCC}(1+\mu_{PCC})l_{eff}^2}{h_{eff}^2} \frac{k}{\gamma_{eff}} \Delta T \quad (56)$$

where,

$\alpha_{PCC}$  is the CTE of the overlay, in/in/°F.

$\mu_{PCC}$  is the Poisson ratio of the overlay.

$\Delta T$  is the temperature difference in the overlay (the product of the overlay thickness and EELTG), °F.

#### 4.2.2.3 Special consideration for joint spacing

Joint spacing plays a particularly important role in the development of faulting since it determines whether the whitetopping undergoes faulting only within the PCC overlay (called partial-depth faulting) or both the overlay and underlying asphalt (called full-depth faulting). These two cases of joint activation, illustrated in Figure 60, lead to significantly different magnitudes of faulting since pumping occurs in either the asphalt layer or the subgrade, respectively [39]. Furthermore, depending on the joint spacing, the joint opening varies substantially due to thermal expansion, which is not fully accounted for in the FEM models.

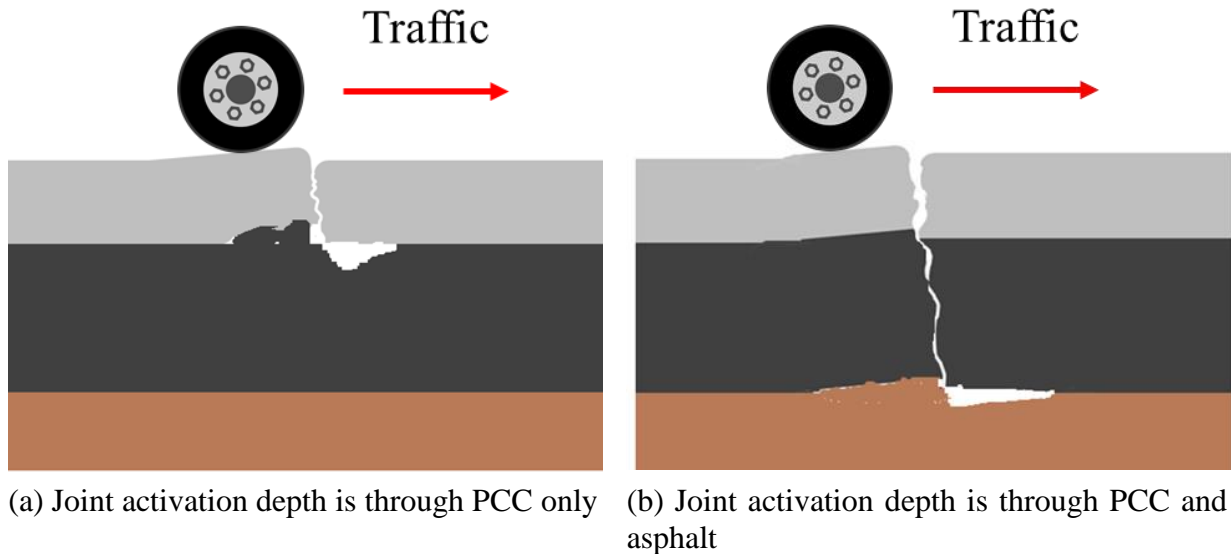


Figure 60 - Faulting due to pumping of the different layers.

Therefore, to account for these effects, the output of the ANNs was multiplied by a non-dimensionalized joint spacing, and the resulting deflection basin difference can be seen in Equation 57. This value was used to calibrate the faulting model, as discussed later.

$$\delta_{\Sigma B,A,JD} = \psi \frac{JTSpace}{h_{PCC}} [NN_{\Sigma B,A,JD}] \quad (57)$$

Where:

$\delta_{\Sigma B,A,JD}$  is the normalized deflection basin, in<sup>4</sup>.

$h_{PCC}$  is the thickness of the overlay, in.  
 $\psi$  is a non-dimensional stability factor and is equal to 1.0 for medium slabs (joint spacing < 10 ft) and 0.01 for long slabs (joint spacing  $\geq$  10 ft). Short slabs (joint spacing  $\leq$  4.5 ft) are not considered in the present study.

#### 4.2.2.4 ANN Training

The training of ANNs can have a relatively high variability due to the possibility of local minima in the objective function [40]. To reduce this variability, 10 ANNs are trained for each predictive model with different semi-random starting conditions. The model prediction is obtained by taking a robust average of the 10 ANNs and discarding the two highest and two lowest estimates. Each ANN was trained using 2 hidden layers of 20 neurons each, which was found to provide enough flexibility for an accurate prediction. Overfitting was prevented by using the Bayesian Regularization training algorithm which includes weight decay. This method was selected over early stopping algorithms, such as Levenberg-Marquardt optimization, since computational time for training was not a concern. The ANNs were trained using outputs from a finite element analysis performed using ABAQUS and validated with whitetopping sections from the Minnesota Road Research Facility (Cells 60, 96, and 97), as well as two sections from the University of California Pavement Research Center heavy vehicle simulator test sections (Sections B and F). Details can be found elsewhere [34].

#### 4.2.2.5 ANN Predictors

Axle load spectra is used to characterize traffic in the development of the ANNs. The effect of these loads is evaluated monthly over the design life of the whitetopping. In addition, wheel wander is accounted for by using the national averages documented in the Pavement ME as Level 3 defaults for the average wheel location and standard deviation. Five wheel locations (mean location is 18 in from the outer edge of the lane/shoulder joint) with a standard deviation of 10 in are used within this framework. Other inputs related to material properties are obtained directly as user inputs.

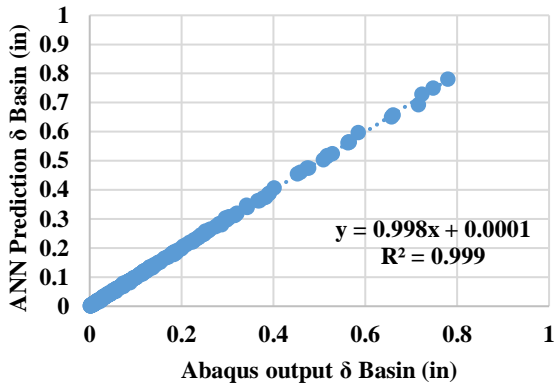
### 4.2.3 Validation

To evaluate model performance, 85% of the data was used in the training set and the remaining 15% in the testing set. The performance of the predictive models for each of the test sets can be seen in Table 16.

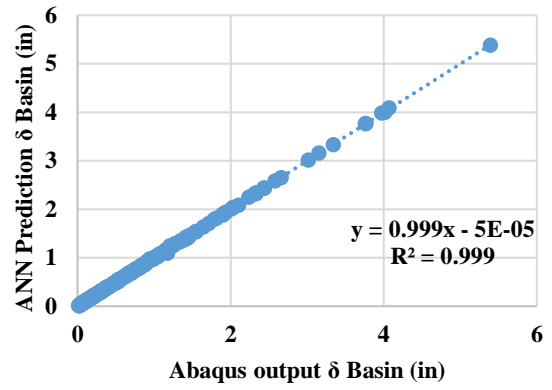
Table 16 – Predictability of ANNs

ANNs	Slab size	ANN	Axle (A)	Joint activation depth (JD)	R <sup>2</sup>
$ANN_{\Sigma B,A,JD}$	Medium	Basin	Single	PCC only	0.99
$ANN_{\Sigma B,A,JD}$	Medium	Basin	Tandem	PCC only	0.99
$ANN_{\Sigma C,A,JD}$	Medium	Corner	Single	PCC only	0.99
$ANN_{\Sigma C,A,JD}$	Medium	Corner	Tandem	PCC only	0.99
$ANN_{\Sigma T,JD}$	Medium	Corner (Temp. only)	-	PCC only	0.99
$ANN_{\Sigma B,A,JD}$	Medium	Basin	Single	Full-depth	0.99
$ANN_{\Sigma B,A,JD}$	Medium	Basin	Tandem	Full-depth	0.99
$ANN_{\Sigma C,A,JD}$	Medium	Corner	Single	Full-depth	0.99
$ANN_{\Sigma C,A,JD}$	Medium	Corner	Tandem	Full-depth	0.99
$ANN_{\Sigma T,JD}$	Medium	Corner (Temp. only)	-	Full-depth	0.99
$ANN_{\Sigma B,A,JD}$	Large	Basin	Single	Full-depth	0.99
$ANN_{\Sigma B,A,JD}$	Large	Basin	Tandem	Full-depth	0.99
$ANN_{\Sigma C,A,JD}$	Large	Corner	Single	Full-depth	0.99
$ANN_{\Sigma C,A,JD}$	Large	Corner	Tandem	Full-depth	0.99
$ANN_{\Sigma T,JD}$	Large	Corner (Temp. only)	-	Full-depth	1.0

The performance of the ANNs was assessed using the test sets and the results are summarized in Figure 61 through Figure 69. Figure 61 shows the performance of the ANNs in predicting deflection basins for the medium sized slabs with the joint only activating through the PCC layer and loaded with single and tandem axles. Figure 62 shows the performance of the ANNs in predicting corner deflections of medium sized slabs when the joint only activates through the PCC layer and loaded with single and tandem axles. Figure 63 shows the performance of the ANNs in predicting corner deflections of medium sized slabs when the joint only activates through the PCC layer and a linear temperature gradient is present.

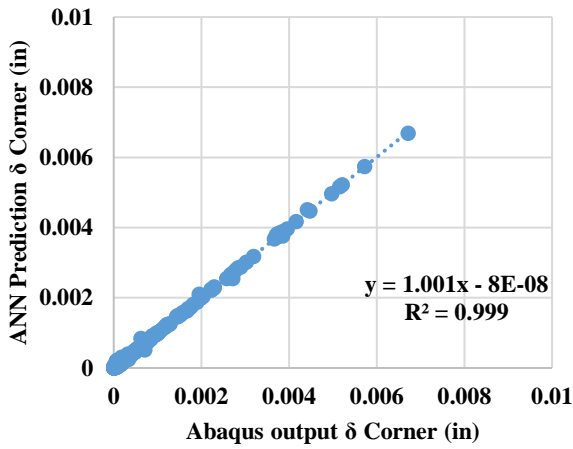


a) Single axle (A=1): PCC depth only

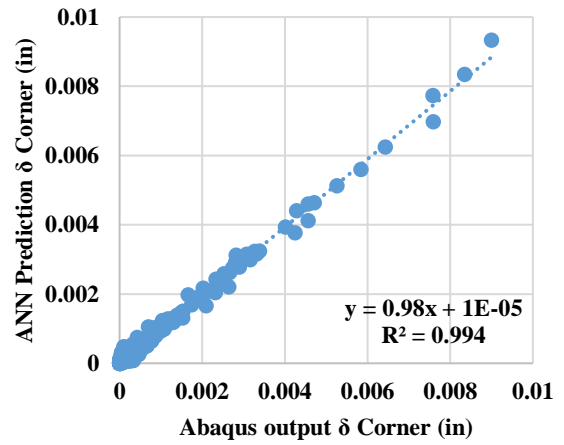


b) Tandem axle (A=2): PCC depth only

Figure 61 – Basins for 8-slab model (joint activates only through PCC)



a) Single axle (A=1): PCC depth only



b) Tandem axle (A=2): PCC depth only

Figure 62 – Corner deflections for 8-slab model (joint activates only through PCC)

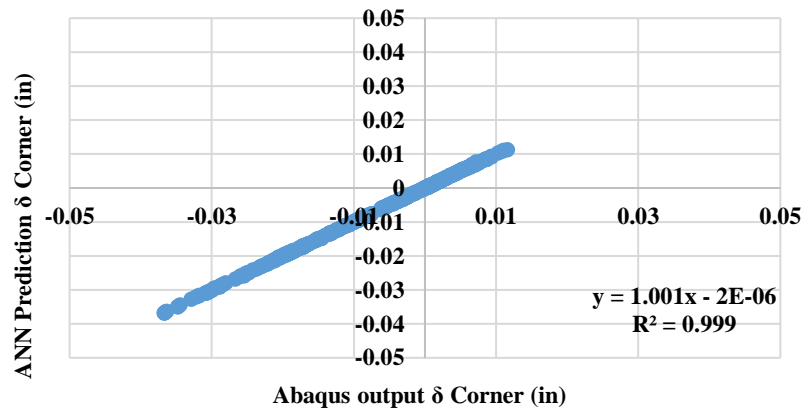
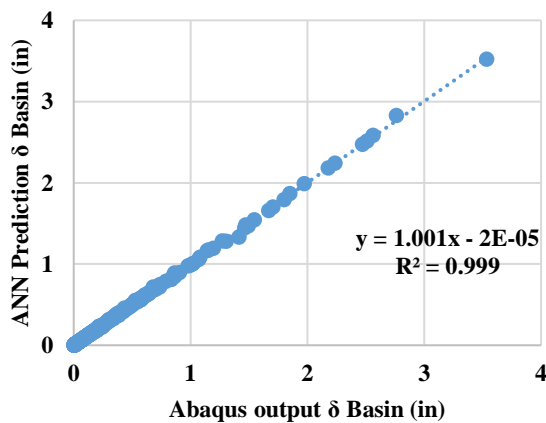
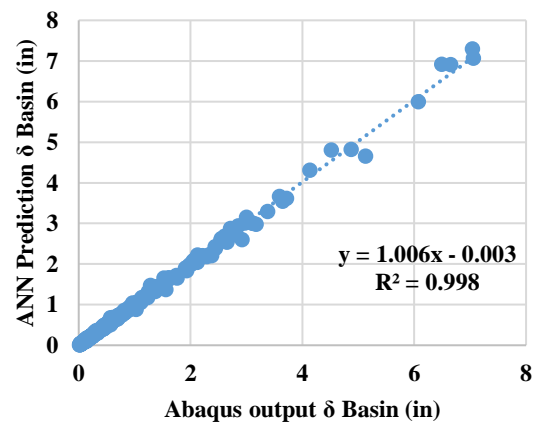


Figure 63 – Corner deflections due to temperature for 8-slab model (joint activates only through PCC)

Figure 64 shows the performance of the ANNs in predicting deflection basins for the medium sized slabs with the joint activating through the PCC and asphalt layer and loaded with single and tandem axles. Figure 65 shows the performance of the ANNs in predicting corner deflections for the medium sized slabs with the joint activating through the PCC and asphalt layer and loaded with single and tandem axles. Figure 66 shows the performance of the ANN in predicting the corner deflection of medium sized slabs when the joint only activates through both the PCC and asphalt layer and a linear temperature gradient is present.



a) Single axle (A=1): Full-depth



b) Tandem axle (A=2): Full-depth

Figure 64 – Basins for 8-slab model (joint activation is full-depth)

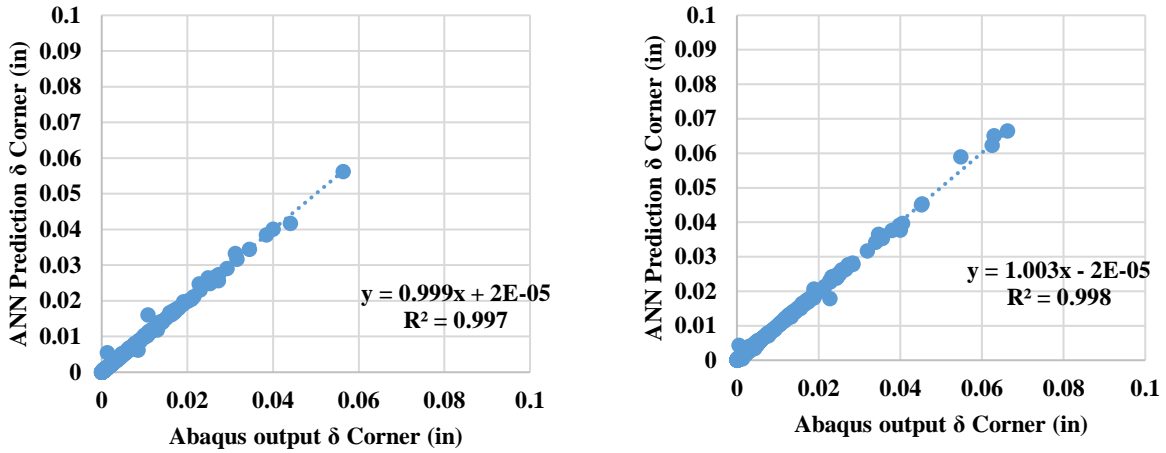


Figure 65 – Corner deflections for 8-slab model (joint activation is full-depth)

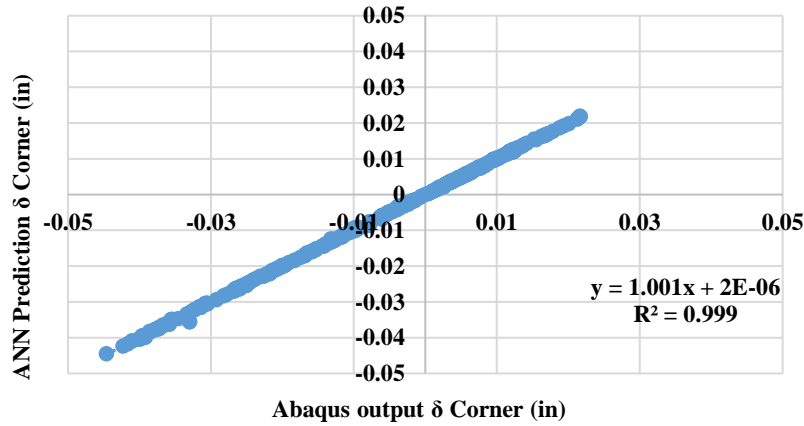
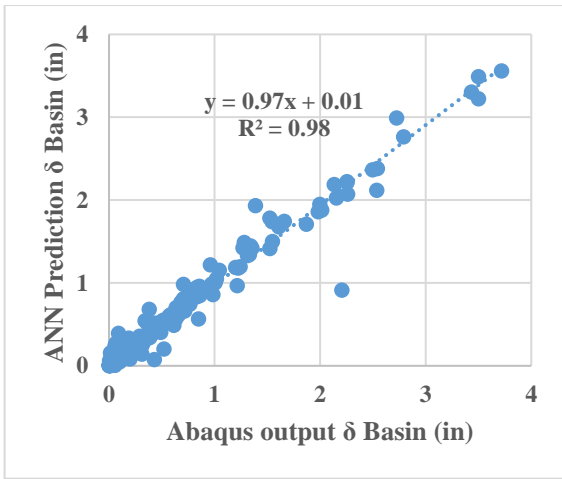
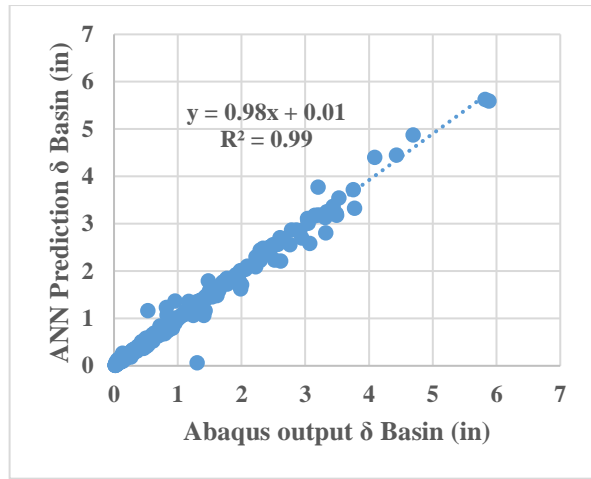


Figure 66 – Corner deflections due to temperature for 8-slab model (joint activation is full-depth)

Figure 67 shows the performance of the ANNs in predicting deflection basins for the large slabs with the joint activating through the PCC and asphalt layer and loaded with single and tandem axles. Figure 68 shows the performance of the ANNs in predicting corner deflections for the large slabs with the joint activating through the PCC and asphalt layer and loaded with single and tandem axles. Figure 69 shows the performance of the ANN in predicting the corner deflection of large slabs when the joint only activates through both the PCC and asphalt layer and a linear temperature gradient is present.

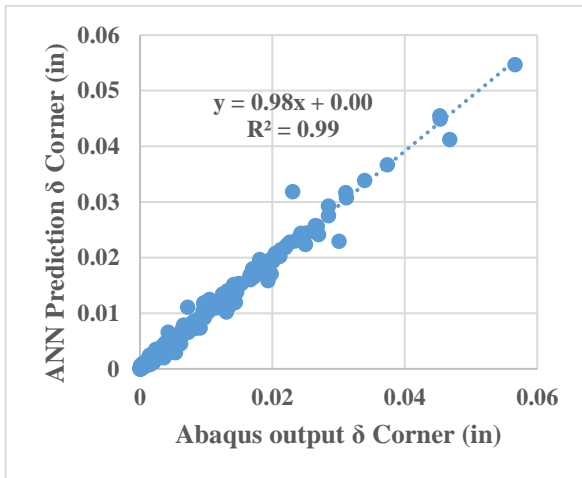


a) Single axle (A=1): Full-depth

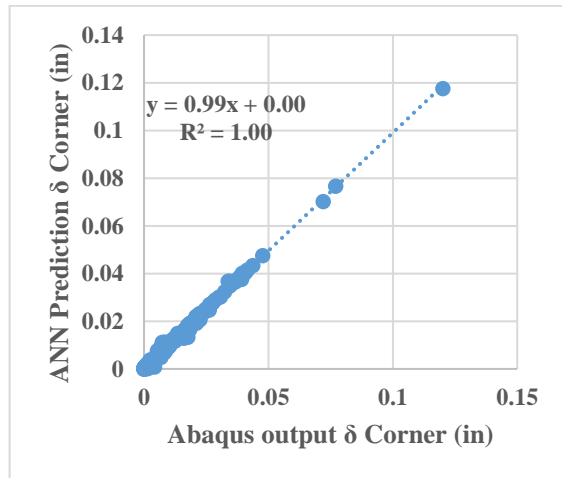


b) Tandem axle (A=2): Full-depth

Figure 67 – Basins for 4-slab model (joint activation is full-depth).



a) Single axle (A=1): Full-depth



b) Tandem axle (A=2): Full-depth

Figure 68 – Corner deflections for 4-slab model (joint activation is full depth).



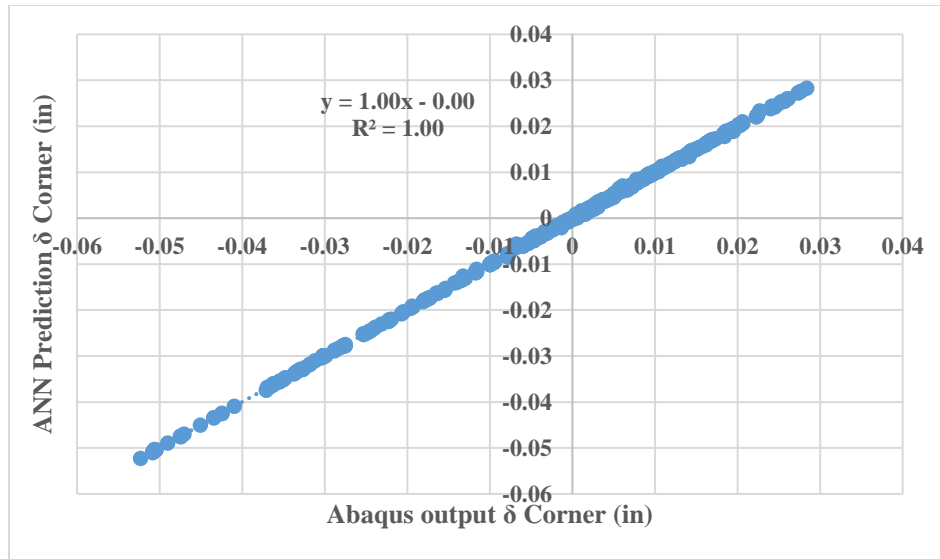
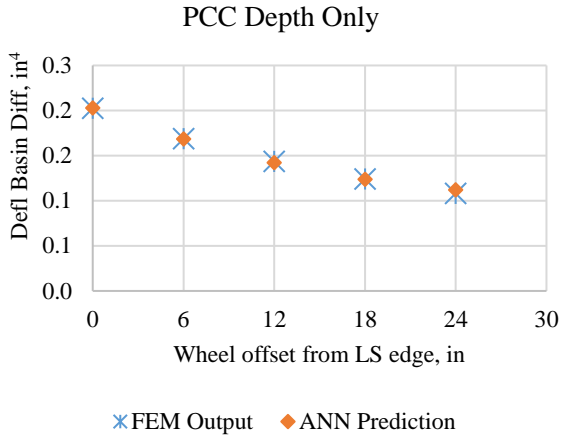
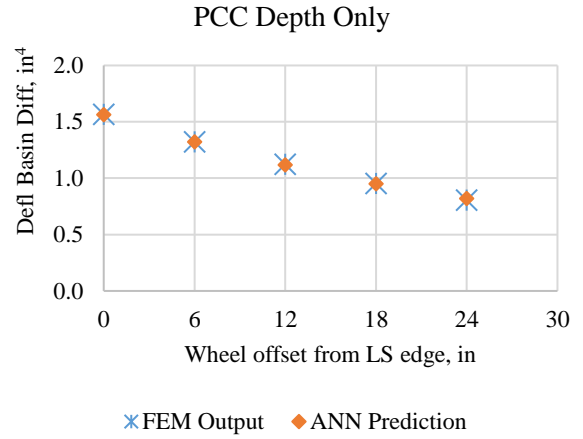


Figure 69 – Corner deflections due to temperature for 4-slab model (joint activation is full-depth).

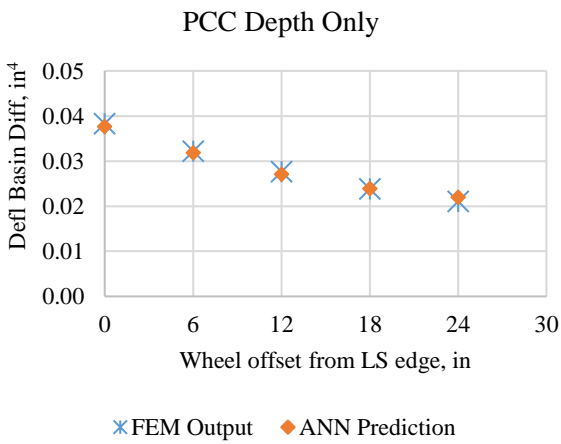
A small validation study was conducted to investigate the effects of wheel offset for two separate structures using the ANNs for predicting the response of the medium sized slabs. The joint spacing, PCC stiffness, asphalt stiffness, and k-value for both structures was 6 ft, 4E+06 psi, 8E+05 psi, and 100 psi/in, respectively. Both depths of joint activation were also considered. The comparisons can be seen in Figure 70.



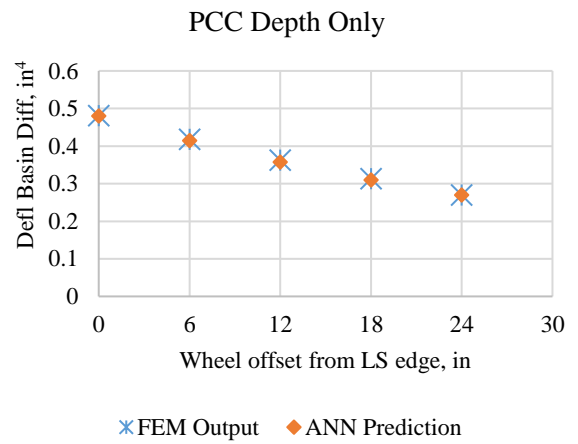
a) Single Axle: PCC = 3.5 in, Asphalt = 3.5 in



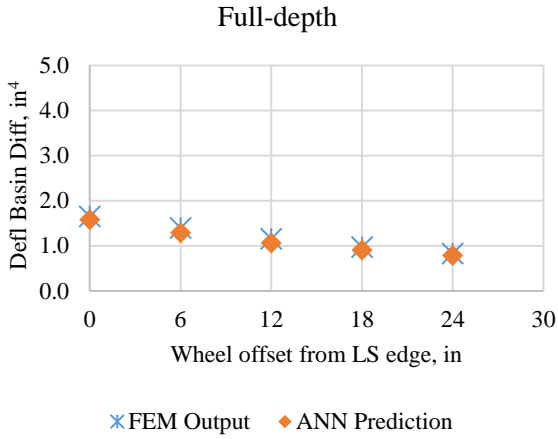
b) Tandem Axle: PCC = 3.5 in, Asphalt = 3.5 in



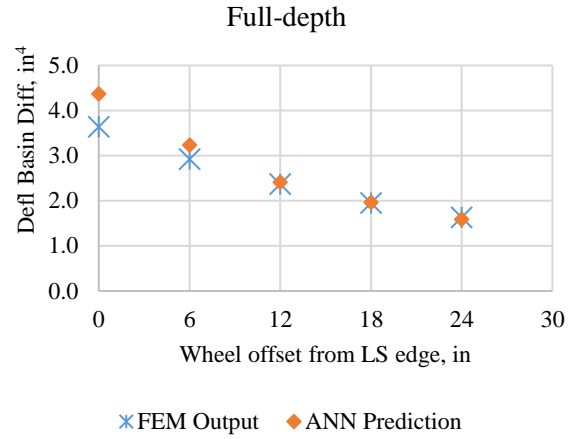
c) Single Axle: PCC = 8 in, Asphalt = 7.5 in



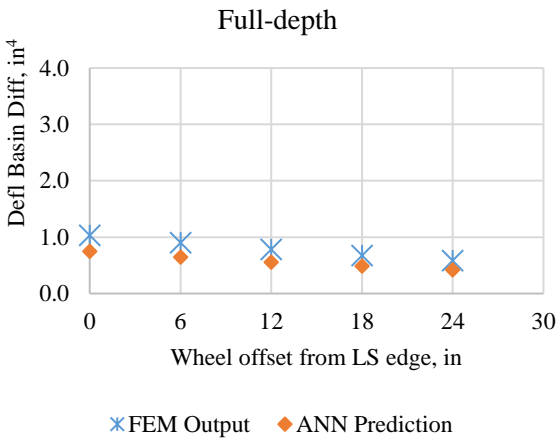
d) Tandem Axle: PCC = 8 in, Asphalt = 7.5 in



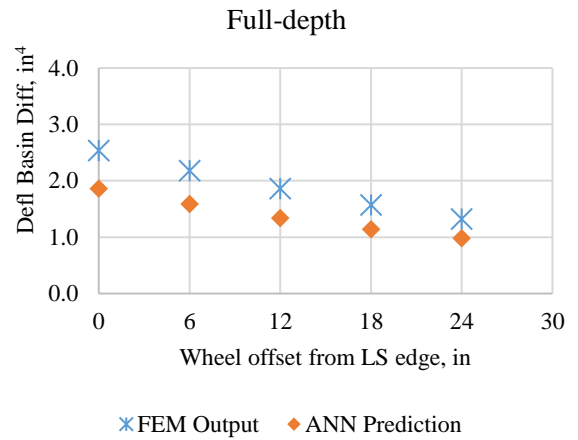
e) Single Axle: PCC = 3.5 in, Asphalt = 3.5 in



f) Tandem Axle: PCC = 3.5 in, Asphalt = 3.5 in



g) Single Axle: PCC = 8 in, Asphalt = 7.5 in



h) Tandem Axle: PCC = 8 in, Asphalt = 7.5 in

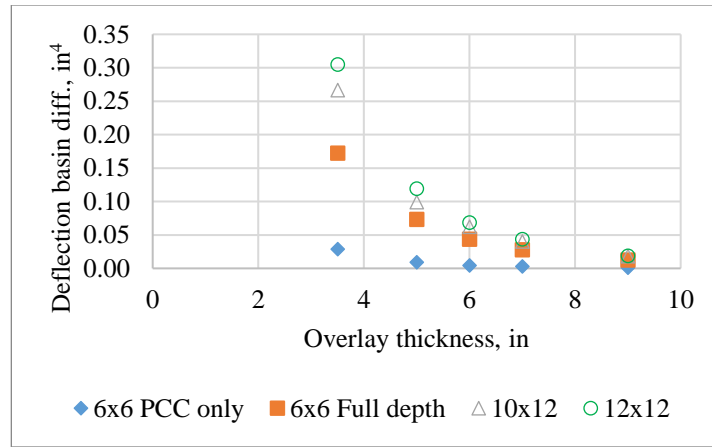
Figure 70 – Validation of ANNs.

#### 4.2.4 Sensitivity Analysis

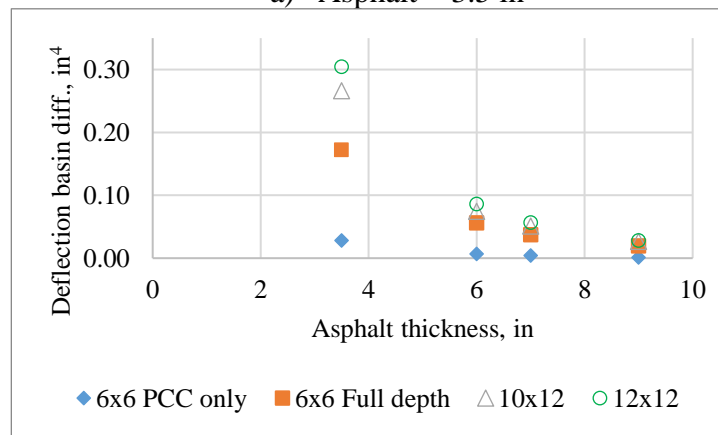
In addition to the validation analysis of the ANNs, a sensitivity analysis was also performed to ensure the range of parameters used in training the networks was sufficient. For the different joint spacings presented, different ANNs needed to be used based on the depth of joint activation. Therefore, when a 6x6 ft joint spacing is presented, and the joint only activates through the PCC layer it is denoted as 6x6 PCC only. When a 6x6 ft joint spacing has a joint activation depth that extends through both the PCC and asphalt layer, it is denoted as 6x6 full-depth. The ANNs for full lane width slabs are used when the joint spacing is greater than or equal to 10 ft. The first comparison evaluates the effect of joint spacing when an 18-kip single axle load is applied. The range of parameters considered are presented in Table 17, and the results can be seen in Figure 71.

Table 17 –Parameters for the sensitivity analysis of the ANNs: single axle – layer thicknesses

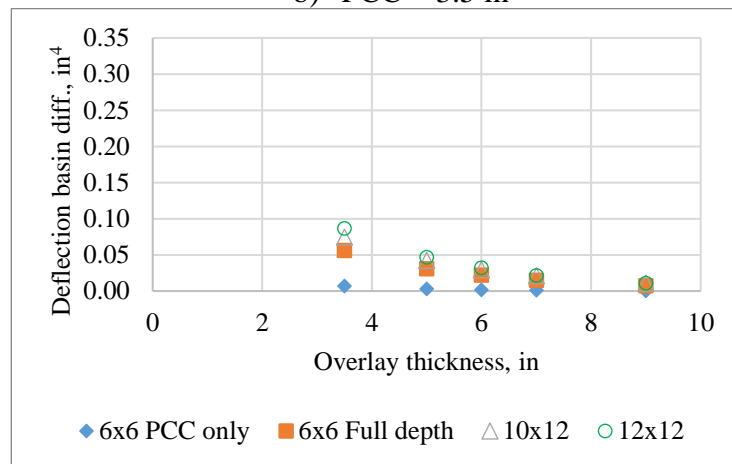
<b>Parameter</b>	
PCC thickness, in	Varies
Asphalt thickness, in	Varies
PCC modulus of elasticity, 10 <sup>6</sup> psi	4.0
Modulus of subgrade reaction, k-value psi/in	250
Asphalt modulus of elasticity, 10 <sup>6</sup> psi	0.80
Panel size, L x W ft	Varies
Shoulder type	Asphalt
Joint depth	Varies
Axle type	Single
Load, lbs	18,000
Wheel wander, in	6



a) Asphalt = 3.5 in



b) PCC = 3.5 in



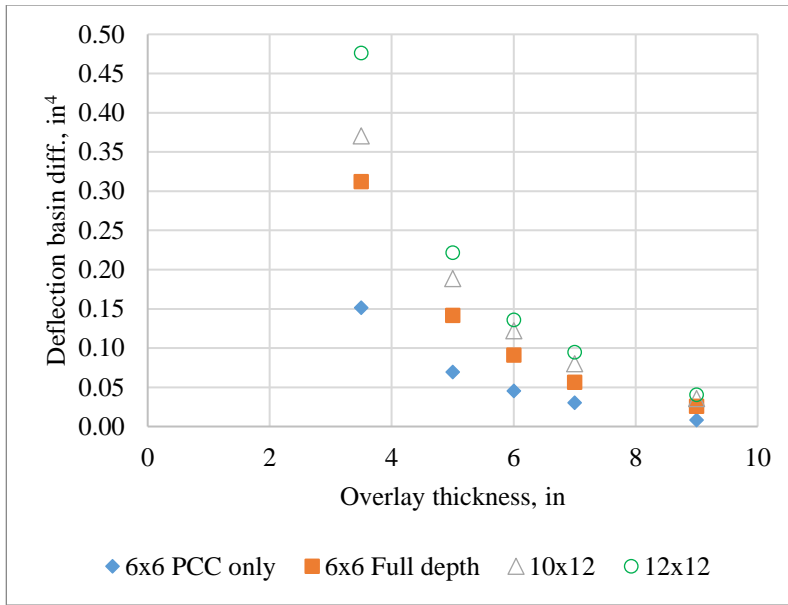
c) Asphalt = 6.0 in

Figure 71 – Parameters for the sensitivity analysis of the ANNs: single axle – layer thicknesses

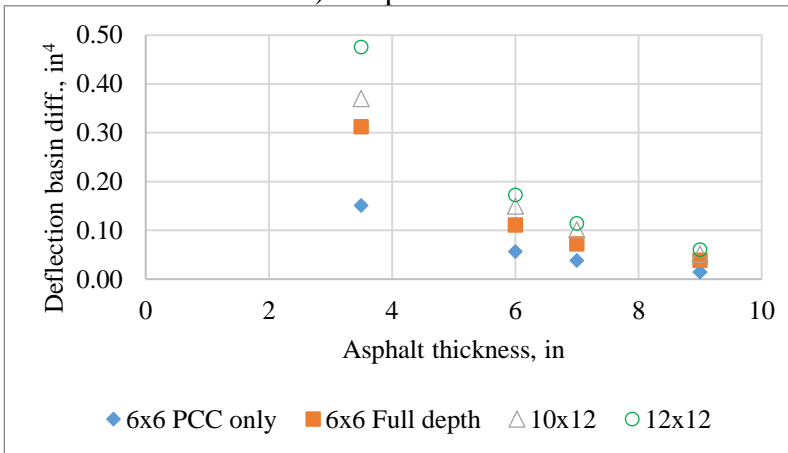
The second comparison evaluates the effect of joint spacings for a 36-kip tandem axle load. The parameters evaluated can be seen in Table 18, and the results can be seen in Figure 72.

Table 18 – Parameters for the sensitivity analysis of the ANNs: tandem axle – layer thicknesses.

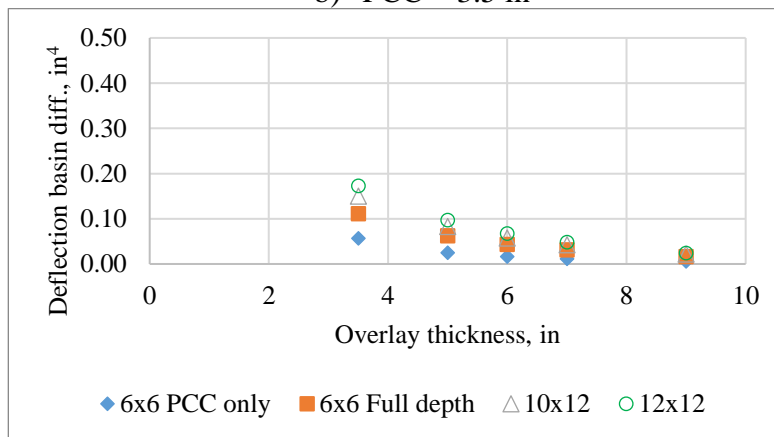
<b>Parameter</b>	
PCC thickness, in	Varies
Asphalt thickness, in	Varies
PCC modulus of elasticity, 10 <sup>6</sup> psi	4.0
Modulus of subgrade reaction, k-value psi/in	250
Asphalt modulus of elasticity, 10 <sup>6</sup> psi	0.80
Panel size, L x W ft	Varies
Shoulder type	Asphalt
Joint depth	Varies
Axle type	Tandem
Load, lbs	36,000
Wheel wander, in	6



a) Asphalt = 3.5 in



b) PCC = 3.5 in



c) Asphalt = 6 in

Figure 72 – ANNs sensitivity analysis: tandem axle – layer thicknesses.

The third comparison evaluates the effect of the modulus of subgrade reaction, k-value, for the different joint spacings when an 18-kip single axle load is applied. These parameters can be seen in Table 19, and the results can be seen in Figure 73.

Table 19 – Parameters for the sensitivity analysis of the ANNs: modulus of subgrade reaction

<b>Parameter</b>	
PCC thickness, in	Varies
Asphalt thickness, in	4.0
PCC modulus of elasticity, 10 <sup>6</sup> psi	4.0
Modulus of subgrade reaction, k-value psi/in	Varies
Asphalt modulus of elasticity, 10 <sup>6</sup> psi	0.80
Panel size, L x W ft	Varies
Shoulder type	Asphalt
Joint depth	Varies
Axle type	Single
Load, lbs	18,000
Wheel wander, in	6



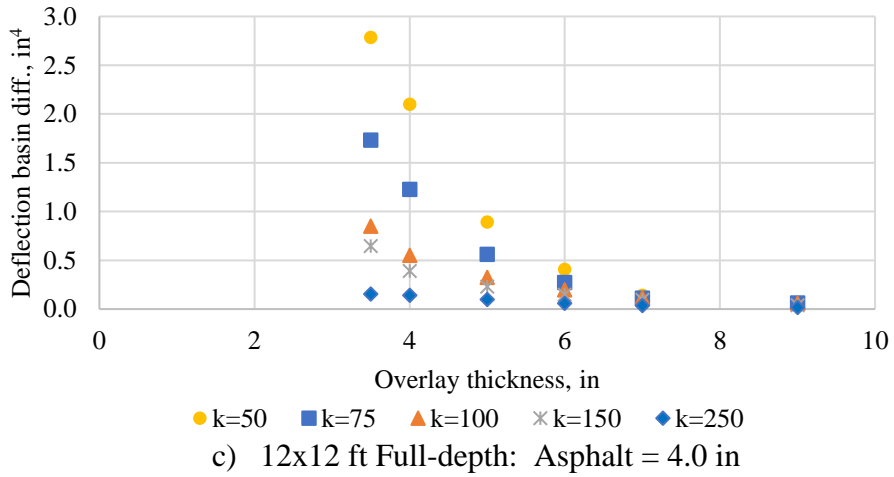
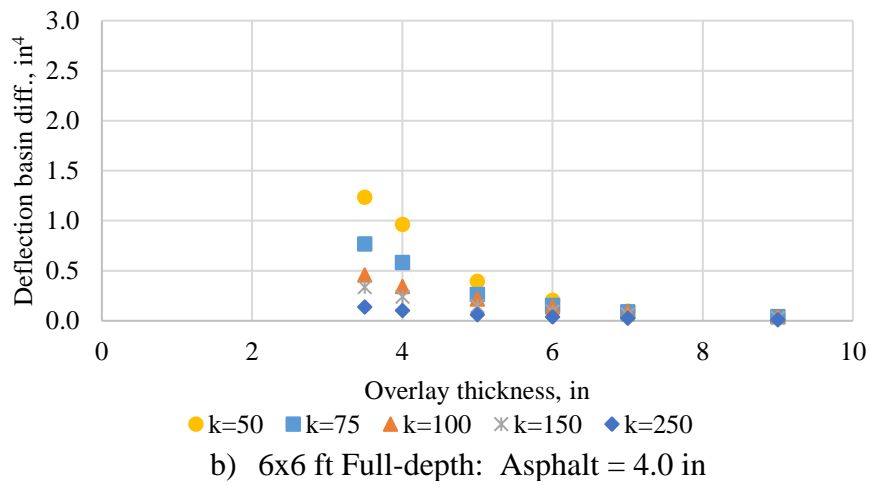
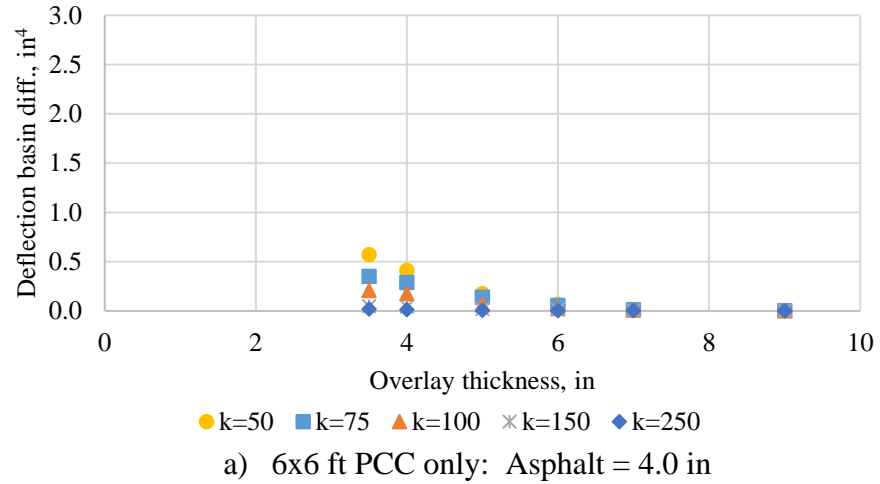
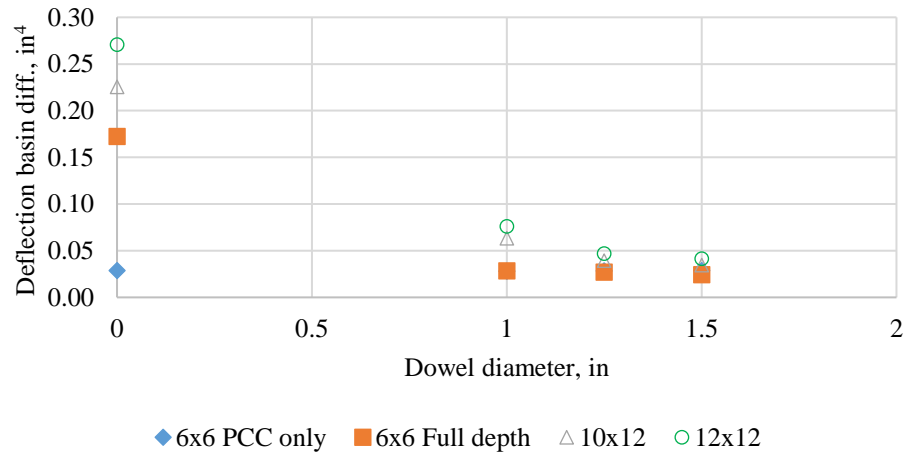


Figure 73 – ANNs sensitivity analysis: modulus of subgrade reaction

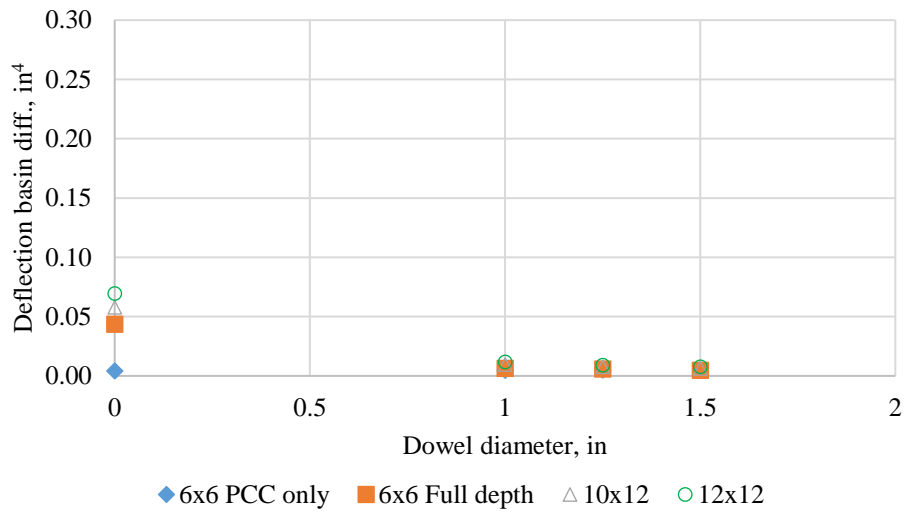
The fourth comparison evaluates the effect of joint spacing when dowels are present, and an 18- kip single axle load is applied. These parameters can be seen in Table 20, and the results can be seen in Figure 74.

Table 20 – Parameters for the sensitivity analysis of the ANNs: presence of dowels

<b>Parameter</b>	
PCC thickness, in	3.5 and 6.0
Asphalt thickness, in	3.5
PCC modulus of elasticity, $10^6$ psi	4.0
Modulus of subgrade reaction, k-value psi/in	250
Asphalt modulus of elasticity, $10^6$ psi	0.80
Panel size, L x W ft	Varies
Shoulder type	Asphalt
Joint depth	Varies
Axle type	Single
Load, lbs	18,000
Wheel wander, in	6



a) PCC = Asphalt = 3.5 in



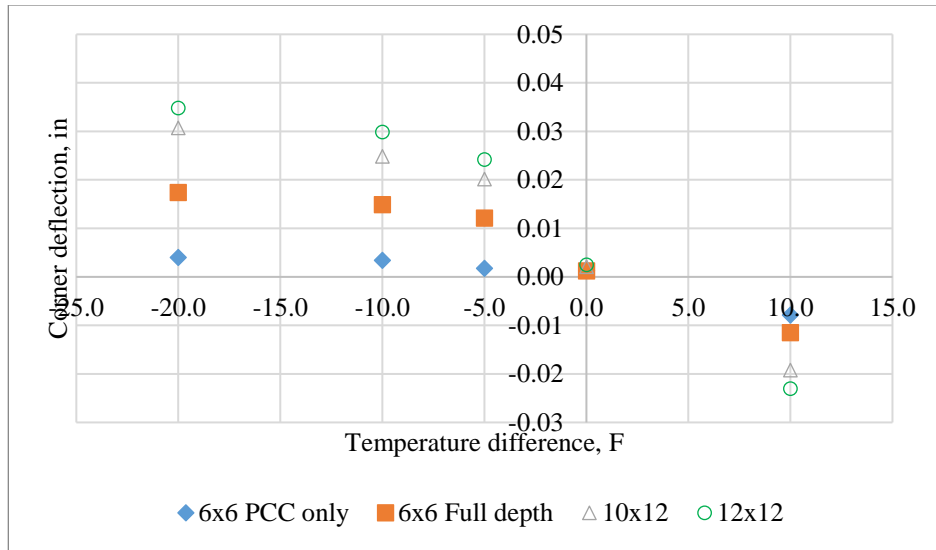
b) PCC = 6 in, Asphalt = 3.5 in

Figure 74 – ANNs sensitivity analysis: presence of dowels.

The next set of comparisons evaluates the effects of temperature gradients. The first comparison evaluates the effect of the overlay thickness for different joint spacings when an 18-kip single axle load is applied. These parameters can be seen in Table 21, and the results can be seen in Figure 75.

Table 21 – Parameters for the sensitivity analysis of the ANNs : temperature difference – PCC thickness.

<b>Parameter</b>	
PCC thickness, in	Varies
Asphalt thickness, in	3.5
PCC modulus of elasticity, 10 <sup>6</sup> psi	4.0
Modulus of subgrade reaction, k-value psi/in	250
Asphalt modulus of elasticity, 10 <sup>6</sup> psi	0.80
Panel size, L x W ft	Varies
Shoulder type	Asphalt
Joint depth	Varies
Axle type	Single
Load, lbs	18,000
Wheel wander, in	6



a) PCC=Asphalt=3.5 in (Note: y-axis different from other plots)

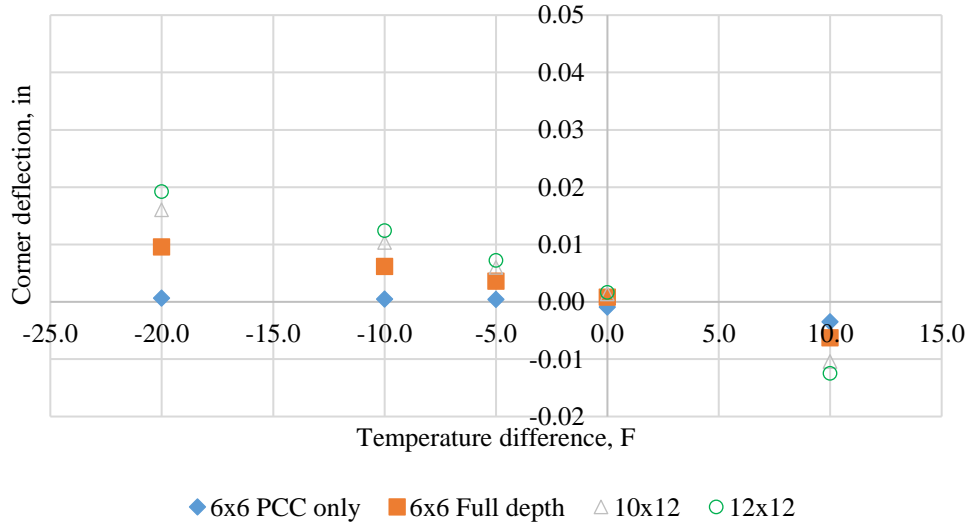
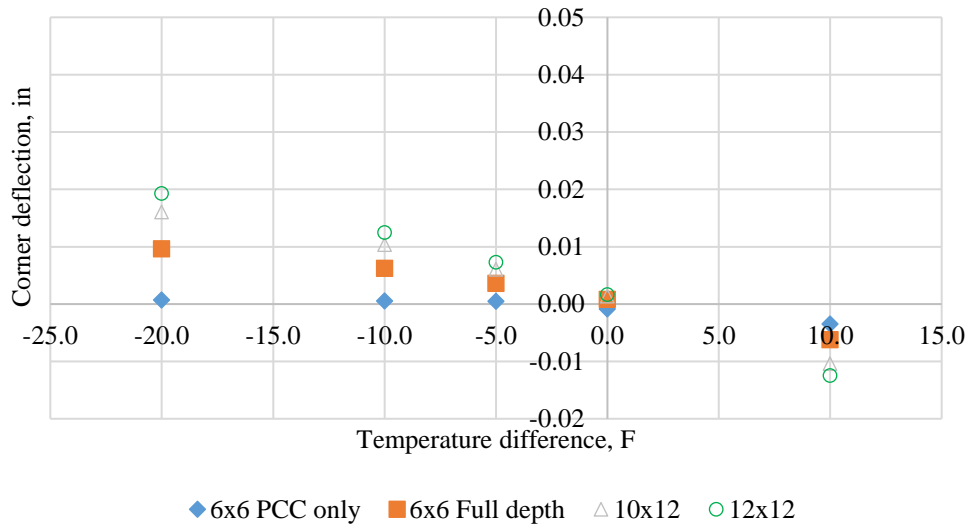


Figure 75 – ANNs sensitivity analysis: temperature difference – PCC thickness.

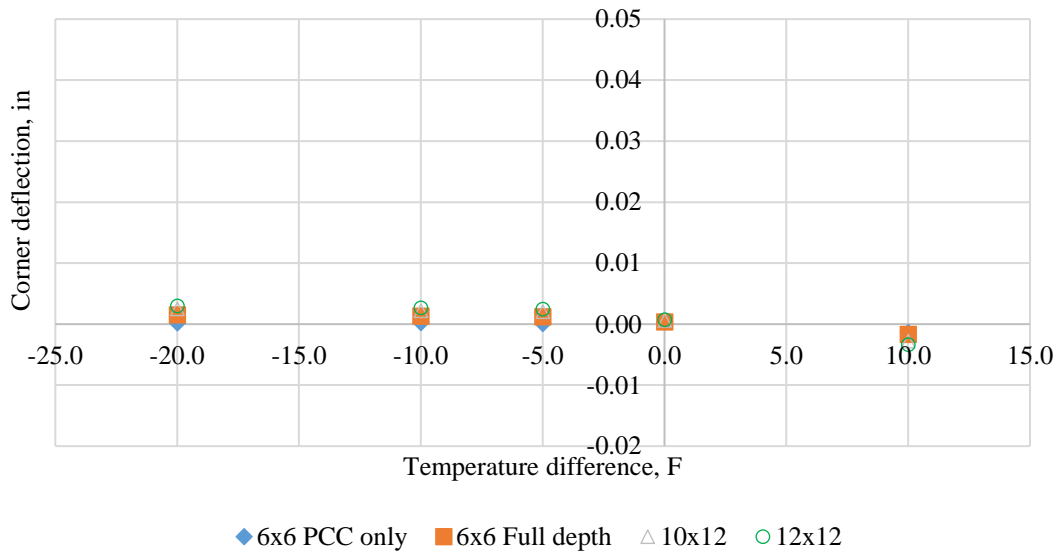
The second comparison evaluates the effects of asphalt thickness for different joint spacings when an 18-kip single axle load is applied. These parameters can be seen in Table 22, and the results can be seen in Figure 76.

Table 22 – Parameters for the sensitivity analysis of the ANNs: temperature difference – asphalt thickness

<b>Parameter</b>	
PCC thickness, in	6.0
Asphalt thickness, in	Varies
PCC modulus of elasticity, 10 <sup>6</sup> psi	4.0
Modulus of subgrade reaction, k-value psi/in	250
Asphalt modulus of elasticity, 10 <sup>6</sup> psi	0.80
Panel size, L x W ft	Varies
Shoulder type	Asphalt
Joint depth	Varies
Axle type	Single
Load, lbs	18,000
Wheel wander, in	6



a) PCC=6 in Asphalt=3.5 in



b) PCC=6 in Asphalt=7.0 in

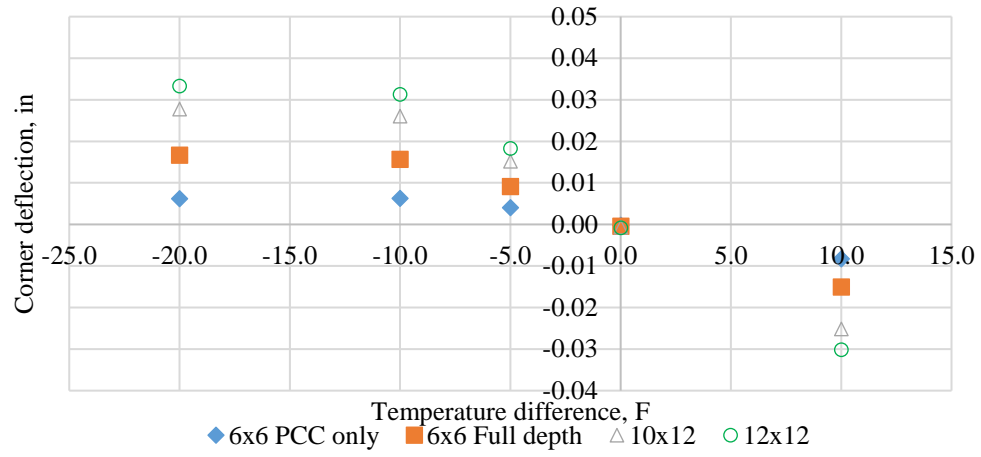
Figure 76 – ANNs sensitivity analysis: temperature difference – asphalt thickness

The third and final comparison evaluates the effects of the modulus of subgrade reaction for a range of joint spacings when an 18-kip single axle load is applied. These parameters can be seen in Table 23, and the results can be seen in Figure 77.

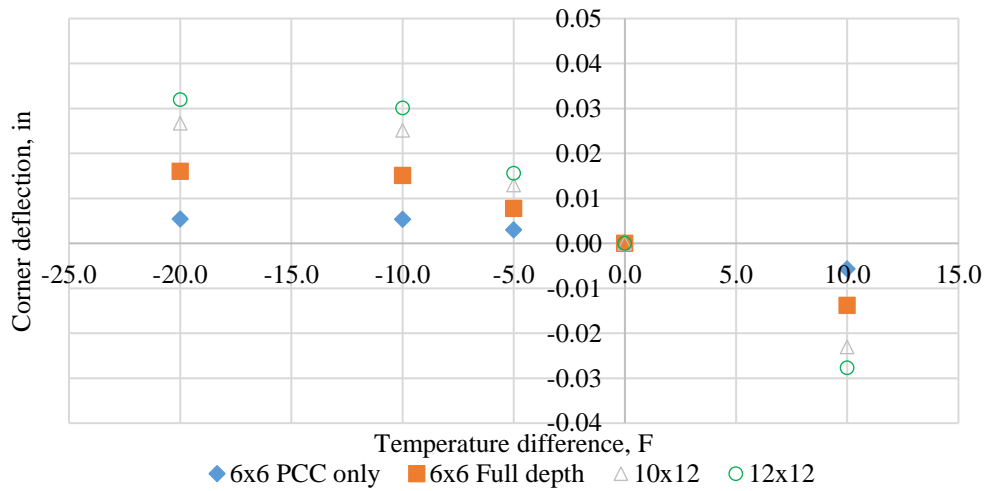
Table 23 – Parameters for the sensitivity analysis of the ANNs: temperature difference – modulus of subgrade reaction.

<b>Parameter</b>	
PCC thickness, in	3.5
Asphalt thickness, in	3.5
PCC modulus of elasticity, 10 <sup>6</sup> psi	4.0
Modulus of subgrade reaction, k-value psi/in	Varies
Asphalt modulus of elasticity, 10 <sup>6</sup> psi	0.80
Panel size, L x W ft	Varies
Shoulder type	Asphalt
Joint depth	Varies
Axle type	Single
Load, lbs	18,000
Wheel wander, in	6





a) k-value = 50 psi/in



b) k-value = 150 psi/in

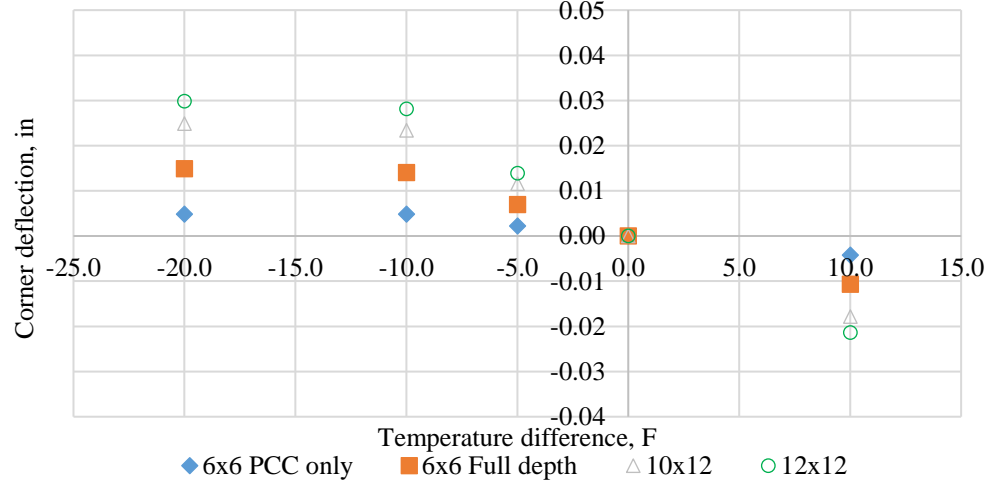


Figure 77 – ANNs sensitivity analysis: temperature difference – modulus of subgrade reaction.

The sensitivity analysis revealed the trends are as expected. The validation and sensitivity analysis provide evidence the ANNs are able to accurately predict the response of the BCOAs. Therefore, the ANNs can now be used within the framework of the predictive faulting model.

#### **4.2.5 Summary**

Models were developed for predicting the response of BCOA to environmental and traffic loading conditions. This eliminates the need to perform an FEM analysis for each loading condition and each different pavement structure when performing the incremental analysis incorporated within the design process. These BCOA response prediction models can now be incorporated into the framework for predicting the development of faulting in BCOA.

To accomplish this, first computational models were developed using a 3-D FEM software, ABAQUS, to accurately predict the behavior of BCOA. These models were validated with sections at MnROAD and the UCPRC testing facility. The computational model included two models. One accounts for a joint that only activates through the PCC and the other when the joint activates through both the PCC and asphalt layers. The critical response for each model is the deflection basin on the approach and leave slabs. When the joint only activates through the PCC, the deflection basin at the bottom of the PCC layer is used. When the joint activates full-depth, the deflection basin at the bottom of the asphalt layer is used. The deflection basins are to be used to more accurately represent the difference in energy density on both sides of the joint in lieu of corner deflections, as has been traditionally used.

Finally, a fractional factorial analysis was performed for a range of parameters, resulting in 19,440 FEM analyses that were used to populate a database for training the ANNs. These ANNs were developed to estimate the mechanistic response of BCOAs using a defined set of inputs. The use of ANNs allow predictions to be made very accurately and quickly. These estimates can be used in conjunction with performance data to produce a mechanistic empirical predictive faulting model for BCOA.

### **4.3 Joint Faulting Model Development**

#### **4.3.1 Introduction**

This section details the development of the BCOA faulting model. The framework used is presented first. This framework incorporates an incremental analysis so the effects of hourly changes in temperature throughout the pavement structure on damage can be characterized. Detailed information on the climatic as well as the other model inputs is provided. Next, the calibration sections are presented with detailed section information provided in Appendix B.

#### **4.3.2 Faulting Model Framework**

The framework for the faulting prediction model consists of using the ANNs developed in the previous section to determine the differential energy. Once the critical response is related to damage using differential energy, the next step is to relate damage to faulting. Within this framework, an iterative incremental analysis is performed to relate damage to faulting. This is then followed by a discussion on the functional form of the current faulting calculation. The overall framework is presented in Figure 78.

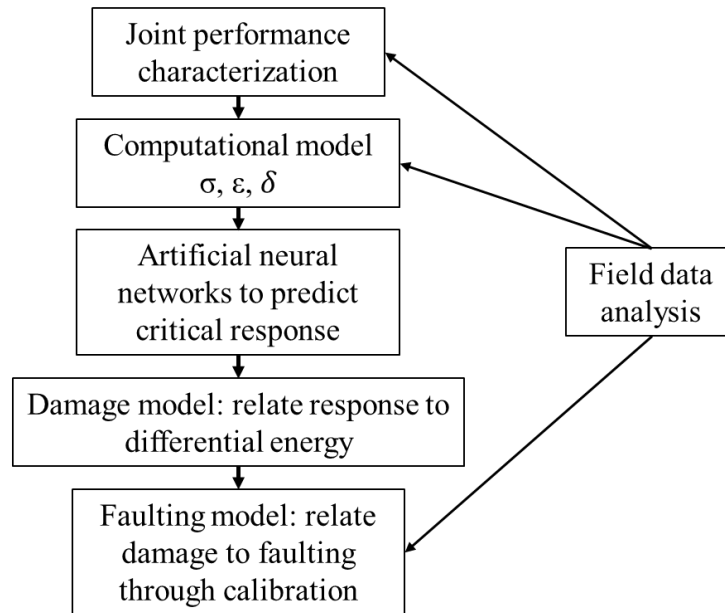


Figure 78 – Faulting model framework

Prior to performing the incremental analysis, initial parameters must be defined. These initial parameters include climatic considerations, traffic information, design features, and layer material properties. First, the treatment of climatic features is presented. Secondly, the traffic analysis is conducted using load spectra and is also presented in terms of ESALs for an easier assessment within the sensitivity analysis. This is then followed by the incremental analysis. The overall prediction framework can be seen in Figure 79.

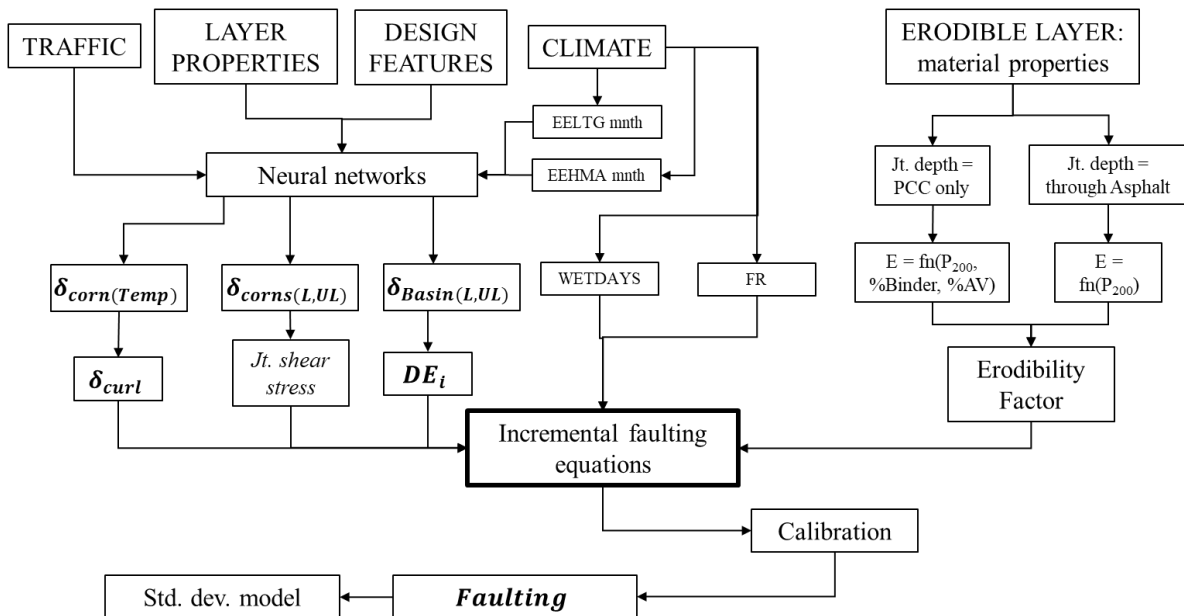


Figure 79– Predictive faulting model framework

#### 4.3.2.1 Climate

This section describes how the temperature throughout the depth of the BCOA is accounted for in the development of the faulting model. Within the current framework, a separate analysis for each structure must be carried out within the Enhanced Integrated Climatic Model (EICM) [41]. EICM performs an hourly incremental analysis that determines the temperature profile throughout the depth of the pavement structure at specified nodes. This is then used to help establish gradients for use in the design process. Therefore, for each calibration section, an EICM file is created. Within EICM, the structure must be defined including layer thicknesses, the number of nodes for each layer, thermal properties, and permeability, porosity, and water content to model moisture movement in granular layers.

Within the overlay, nodes are placed at 1-in increments. Additionally, using the North American Regional Reanalysis (NARR) climatic database, the nearest weather station to each calibration site is chosen to give hourly values of air temperature, precipitation, wind speed, and percent sunshine for several years that can be output as an .icm profile. To ensure the weather was representative of the given calibration section locations, multiple weather stations were used with triangulation. The analysis is then performed so the hourly nodal temperature depths throughout the structure can be determined. EICM generates a .tem file that contains these nodal temperatures. This information is then used to determine the PCC overlay mean monthly nighttime mid-depth temperature ( $T_{mid-depth}$ ), establish hourly ELTG based on equivalent strain, and to determine the freezing ratio (FR), which is the percentage of time that the top of the asphalt layer is less than 32°F. The .icm file for each EICM analysis is used to establish mean monthly air temperature and the number of rain days (days with precipitation > 0.1 in) in the year (WETDAYS).

Temperature gradients can cause the PCC slab to curl, which influences the magnitude of the corner deflections. A positive temperature gradient is present when the temperature at the top of the PCC slab is warmer than the bottom of the slab. This causes the slab to curl downward, leaving the mid-slab partially supported and the edges fully supported. A negative temperature gradient is present when the temperature at the top of the PCC slab is cooler than the bottom of the slab. This causes the slab to curl upward, leaving the edges and corners of the slab partially supported, while the mid-slab is fully supported. When a slab is curled up, the deflections are expected to be larger than when a slab is curled down due to the support conditions. The larger deflections imply an increase in the potential for the development of faulting. Due to the magnitude of deflections and the support conditions, this analysis only considers when a negative temperature gradient is present. To simplify this, only traffic between 8 pm and 8 am is considered. It is important to be able to account for the environmental loading effects in addition to the effects due to traffic loading.

The ELTGs are calculated using the temperature-moment concept [42] that converts the non-linear temperature profile for a specific hour generated by the EICM into an ELTG based on Equation 58 through 60. This conversion was proposed by Janssen and Snyder [42] to ensure that the resultant strains in the overlay resulting from the ELTG and the non-linear temperature gradient are the same. This results in the same deflection profile of the slab for the two conditions.

$$T_{ave} = \sum_{i=1}^n \left[ \frac{0.5(t_i + t_{i+1})(d_i - d_{i+1})}{(d_1 - d_n)} \right] \quad (58)$$

$$TM_0 = -0.25 \sum_{i=1}^n [(t_i + t_{i+1})(d_i^2 - d_{i+1}^2) - 2(d_1^2 - d_n^2)T_{ave}] \quad (59)$$

$$ELTG = -\frac{12 \cdot TM_0}{h^3} \quad (60)$$

where:

ELTG is the equivalent linear temperature gradient, °F/in;

$T_{ave}$  is the average temperature, °F;

$TM_0$  is the temperature moment, °F·in<sup>2</sup>;

$d_i$  is the depth of the  $i^{\text{th}}$  node, in;

$t_i$  is the temperature at depth  $d_i$ , °F.

An effective equivalent linear temperature gradient (EELTG) was established for each calibration section to simplify the calibration process by eliminating the need for an hourly incremental analysis. The EELTG is the equivalent linear temperature gradient that when applied throughout the design life results in the same damage (cumulative differential energy) as if the hourly linear temperature gradients were used. To establish the EELTG, first the non-linear temperature gradient for each project is determined on an hourly basis using the EICM [41]. Next, the hourly non-linear temperature gradients are converted to hourly ELTGs based on strain equivalency, as described above. When calculating the differential energies, 1 million ESALs are applied over the course of the year, with the same number of vehicles applied each day. Hourly traffic distributions were assigned using the percentages incorporated in Pavement ME and summarized in Table 24 [1]. Mean monthly mid-depth temperatures of the slab are used to estimate monthly joint widths so the joint stiffness can be determined and hourly temperatures at mid-depth of the asphalt are used to estimate the dynamic modulus of the asphalt layer.

Table 24 – Hourly truck traffic distributions from Pavement ME [1].

Time period	Distribution (percent)	Time period	Distribution (percent)
12:00 a.m. - 1:00 a.m.	2.3	12:00 p.m. - 1:00 p.m.	5.9
1:00 a.m. - 2:00 a.m.	2.3	1:00 p.m. - 2:00 p.m.	5.9
2:00 a.m. - 3:00 a.m.	2.3	2:00 p.m. - 3:00 p.m.	5.9
3:00 a.m. - 4:00 a.m.	2.3	3:00 p.m. - 4:00 p.m.	5.9
4:00 a.m. - 5:00 a.m.	2.3	4:00 p.m. - 5:00 p.m.	4.6
5:00 a.m. - 6:00 a.m.	2.3	5:00 p.m. - 6:00 p.m.	4.6
6:00 a.m. - 7:00 a.m.	5.0	6:00 p.m. - 7:00 p.m.	4.6
7:00 a.m. - 8:00 a.m.	5.0	7:00 p.m. - 8:00 p.m.	4.6
8:00 a.m. - 9:00 a.m.	5.0	8:00 p.m. - 9:00 p.m.	3.1
9:00 a.m. - 10:00 a.m.	5.0	9:00 p.m. - 10:00 p.m.	3.1
10:00 a.m. - 11:00 a.m.	5.9	10:00 p.m. - 11:00 p.m.	3.1
11:00 a.m. - 12:00 p.m.	5.9	11:00 p.m. - 12:00 a.m.	3.1

It is important to account for the effects of temperature on changes in the stiffness of the asphalt layer due to the affects it has on differential energy. Asphalt is a viscoelastic material that is temperature dependent, which will cause changes in stiffness due to hourly and seasonal temperature changes. When the asphalt layer is very stiff, lower deflections are likely to occur in comparison to when the asphalt layer is at a minimum stiffness. A higher stiffness results in lower deflections and a lower differential energy, whereas a lower stiffness results in higher deflections and a larger differential energy. Therefore, it is important to capture the effect of asphalt stiffness within the prediction process. An equivalent monthly asphalt stiffness was used for each month in the analysis period for the calibration sections, as described below.

The framework used to establish the equivalent monthly asphalt stiffness is similar to the procedure established in the BCOA-ME [25]. First, a mastercurve is established for the asphalt modulus using a uniform aggregate gradation. SHRP LTPPBIND version 3.1, which is a Superpave binder selection program developed for the Federal Highway Administration (FHWA), is used to select the asphalt binder grade according to the location of the project [43].

For each month, the differential energy is summed for the pavement section based on the loading conditions used when establishing the EELTG. The dynamic modulus of the asphalt ( $E_{HMA}$ ) is established based on hourly climatic data to determine the monthly differential energy. Then, `fminsearch` in MATLAB is used to find an equivalent asphalt dynamic modulus, that would result in the same differential energy each month. The EELTG and the 12 monthly equivalent dynamic moduli for each calibration section can be found in Appendix A.

#### 4.3.2.2 Traffic

##### Axle Load Spectra

The traffic analysis within this procedure uses axle load spectra. The analysis follows a similar procedure to the BCOA-ME [44]. Direct inputs for predicting joint faulting includes the one-way

average daily traffic (ADT), percent of trucks (as a decimal), the number of lanes in each direction, the growth type, and the growth rate. The growth type can either be compound or linear growth and is computed as follows (Table 25).

Table 25 – Function used in computing/forecasting truck traffic over time

Growth type	Model
Non-linear	$G_f = \frac{[(1 + G_{r,ADTT})^n - 1]}{G_{r,ADTT}}$
Linear growth	$G_f = n \times \left(1 + G_{r,ADTT} \times \frac{(n - 1)}{2}\right)$

where:

$G_{r,ADTT}$  is the user-defined growth rate of average daily truck traffic, ADTT;  
 $n$  is the design life, years.

The number of lanes is used to determine the lane distribution factor (LDF) as a function of the defined one-way ADT. The LDFs are established based on FHWA recommendations as a function of the number of lanes and the one-way ADT. The LDFs can be seen in Table 26.

Table 26 – Lane distribution factors for multiple-lane highways [1].

One-way ADT	2 lanes (one direction): % outer lane	3+ lanes (one direction): % outer lane
2,000	94	82
4,000	88	76
6,000	85	72
8,000	82	70
10,000	81	68
15,000	77	65
20,000	75	63
25,000	73	61
30,000	72	59
35,000	70	58
40,000	69	57
50,000	67	55
60,000	66	53
70,000	-	52

The axle load distributions for single and tandem axles can be seen in Table 27. The axle load distributions are adopted from the axle load distributions provided in the ACPA guidelines for “Design of Concrete Pavement for City Streets” [45]. These load distributions are a function of road category, the axle type, and the axle load. These distributions are also used in the BCOA-ME design procedure [44].

Table 27 – Axles per 1000 trucks for different road categories. Source: “Design of Concrete Pavement for City Streets” [45].

Axle load (kips)	Axles per 1000 trucks			
	Category LR	Category 1	Category 2	Category 3
<b>Single axles</b>				
4	846.15	1693.31	0.00	0.00
6	369.97	732.28	0.00	0.00
8	283.13	483.10	233.60	0.00
10	257.60	204.96	142.70	0.00
12	103.40	124.00	116.76	182.02
14	39.07	56.11	47.76	47.73
16	20.87	38.02	23.88	31.82
18	11.57	15.81	16.61	25.15
20	0.00	4.23	6.63	16.33
22	0.00	0.96	2.60	7.85
24	0.00	0.00	1.60	5.21
26	0.00	0.00	0.07	1.78
28	0.00	0.00	0.00	0.85
30	0.00	0.00	0.00	0.45
<b>Tandem axles</b>				
4	15.12	31.90	0.00	0.00
8	39.21	85.59	47.01	0.00
12	48.34	139.30	91.15	0.00
16	72.69	75.02	59.25	99.34
20	64.33	57.10	45.00	85.94
24	42.24	39.18	30.74	72.54
28	38.55	68.48	44.43	121.22
32	27.82	69.59	54.76	103.63
36	14.22	4.19	38.79	56.25
40	0.00	0.00	7.76	21.31
44	0.00	0.00	1.16	8.01
48	0.00	0.00	0.00	2.91
52	0.00	0.00	0.00	1.19

\*Tridem axles are not considered in this design procedure. *LR = Light residential.*

In order to determine the load spectra for each month of the design period, the following steps are taken. First, the monthly AADTT is calculated based on the ADT, growth type, growth rate, and LDF. Next, the number of single and tandem axles per 1000 trucks are determined based on the corresponding road classification for each day using the information provided in Table 27. The number of single and tandem axles per day are determined using the AADTT and the number of single and tandem axles per 1000 truck (Table 27). The last step is to ensure the number of single and tandem axles per load level per day are converted into the number of single and tandem axles per load level per month.



Another portion of the framework dealing with traffic considerations is wheel wander. The mean wheel location is assumed to be 18 in from the outer edge of the wheel to the edge of the lane. Also, a standard deviation of 10 in is assumed. Both values are based on the national averages used in Pavement ME as Level 3 default values [1]. Five-wheel locations are used in this analysis and include distances of 0, 8, 18, 28, and 36 in from the outer edge of the wheel to the edge of the lane. The probability of each wheel wander location based on the assumed standard deviation is 6.7, 24.2, 38.3, 24.2, and 6.7 %, respectively.

### ESAL Prediction

Although this procedure uses axle load spectra to determine differential energy, ESALs are also determined based on the load spectra previously presented. In order to determine ESALs, the following steps are taken. The equation used for calculating design ESALs is given as:

$$ESAL_{design} = DD \times LDF \times G_f \times ESAL_{daily} \times 365 \quad (61)$$

where:

*DD* is the directional distribution factor and indicates the fraction of total traffic in the design direction. For one-way traffic, which is required for this procedure, the default value is 1.0;

*LDF* is the lane distribution factor previously presented;

*G<sub>f</sub>* is the traffic growth factor determined based on the type of growth rate;

*ESAL<sub>daily</sub>* is the sum of daily equivalent single axle loads determined for each type of axle load, presented below.

$$ESALs_{daily} = N_R \times LEF \quad (62)$$

where:

*N<sub>R</sub>* is the number of repetitions for a specific axle load per day;

*LEF* are the load equivalency factors for each load level to convert into ESALs.

$$N_R = \frac{ADTT}{1000} \times Axles \text{ per } 1000 \text{ trucks} \quad (63)$$

where:

*Axles per 1000 trucks* is obtained from the axle load distributions provided in Table 27.

*ADTT* is the average daily truck traffic given as:

$$ADTT = ADT \times Truck \text{ percent} \quad (64)$$

where:

*ADT<sub>One-way</sub>* is the user-inputted one-way average daily traffic. If unavailable, ADTT can be estimated based on the typical values of ADTT for different road categories given in Table 28;

Truck percent is the percentage of total traffic comprised of trucks.

Table 28 – ADTT given for different road categories and classifications [45].

Classification	ADTT	Road category
Light residential	3	LR
Residential	10 to 50	1
Collector	50 to 500	2
Business	400 to 700	
Minor arterial	300 to 600	
Industrial	300 to 800	3
Major arterial	700 to 1500	

The LEFs can be calculated as follows:

$$LEF = \left( \frac{W_x}{W_{18}} \right)^{-1} \quad (65)$$

where:

$W_x$  is the number of 18-kip ESALs for any loading  $x$ , and  $W_x = W_{18}$  for  $x = 18$  kips.  $W_x$  is calculated using the following equation:

$$\log(W_x) = 5.908 - 4.62 \log(L_x + L_2) + 3.28 \log(L_2) + \frac{G_t}{\beta_x} - \frac{G_t}{\beta_{18}} \quad (66)$$

where:

$L_x$  is the axle loading, kips;

$L_2$  is the weight of the axle, kips (1 for single axle and 2 for tandem axle);

$\beta_x$  is a constant to reflect the current loading in kips ( $x$ );

$\beta_x = \beta_{18}$  for  $x = 18$  kips;

$G_t$  is the growth rate.

$$\beta_x = 1 + \frac{3.63(L_x + L_2)^{5.2}}{(h_{PCC} + 1)^{8.46} L_2^{3.52}} \quad (67)$$

$$\beta_{18} = 1 + \frac{1.62 \times 10^7}{(h_{PCC} + 1)^{8.46}} \quad (68)$$

where:

$h_{PCC}$  is the PCC thickness, in.

$$G_t = \log \left( \frac{4.5 - P_t}{4.5 - 1.5} \right) \quad (69)$$

where:

$P_t$  is the pavement terminal serviceability.

#### 4.3.2.3 Model Inputs

With the ELTGs defined for each calibration section, the iterative faulting calculations can be performed. The incremental analysis process can be seen in Figure 80.

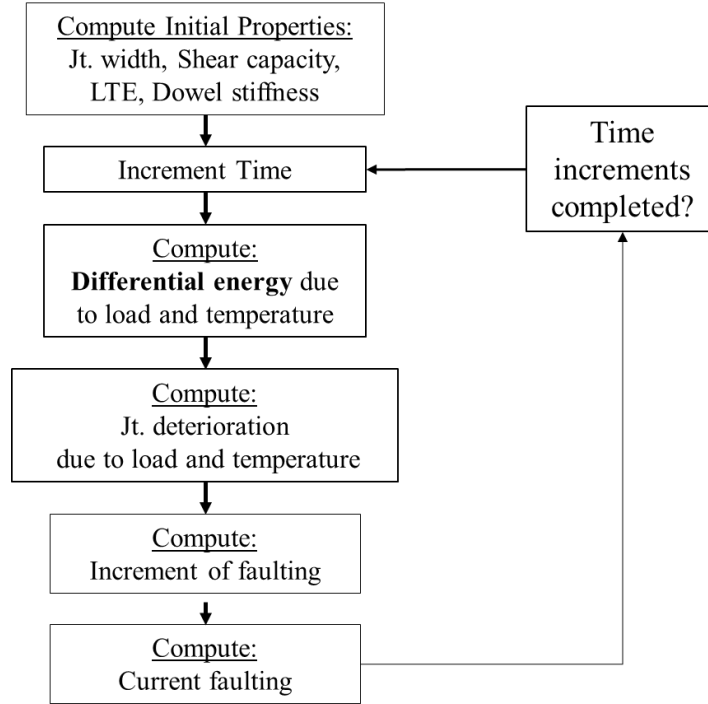


Figure 80 – Predictive faulting incremental analysis

The primary calculation for each month is to determine the differential energy using Equations 70 and 71.

$$\sum \delta_{B,m} = NN_{\Sigma B,A,JD} (JTSpace, l_{eff}, q_i^*, k, \frac{AGG}{k * l_{eff}}, LTE_{shoulder}, s, \Phi) \quad (70)$$

$$DE_m = \sum_1^A \sum_1^j \sum_1^i \left( \frac{1}{2} k \left( \sum \delta_{B,m} \right) * WWpr_i * load_{A,j} \right) \quad (71)$$

where the variables in Equation 70 are defined previously, and:

$DE_m$  is the differential energy density deformation accumulated for month  $m$ , lb-in;

$WWpr_i$  is wheel wander distribution over the number of bins  $i$ ;

$load_{A,j}$  is the number of axles of axle type  $A$  at each load level  $j$ , where  $A$  is either single or tandem axle, lbs;

$\sum \delta_{B,m}$  is the difference between the loaded and unloaded slab deflection basins for month  $m$ , in<sup>4</sup>.

For each calibration section, four files are needed to perform the faulting calculation including input, equivalent monthly asphalt stiffness, .tem, and .icm files. The .tem and .icm EICM files have been previously discussed along with the climatic considerations. Example input and asphalt stiffness text files are shown in Table 29. Twenty-two different inputs are specified for each section, as can be seen in Table 29a.

Table 29 – Examples of (a) an input text file and (b) an asphalt stiffness text file.

5	Overlay thickness (in)
4000000	Elastic modulus of overlay (psi)
4000	Compressive strength of overlay (psi)
650	Flexural strength of overlay (psi)
7	Asphalt thickness (in)
0	Blank
250	k-value (psi/in)
144	Joint spacing (in)
0	Joint depth (0=pcc only, 1=pcc and asphalt)
0	Dowel (0 if no, 1 if yes)
0	Dowel diameter (in)
0	LTE of shoulder
5.5	Coefficient of thermal expansion of overlay (*10 <sup>-6</sup> in/F/in)
240	Analysis period/ Design life
-1.0062	ELTG
9	Month of construction (September)
550	Cement Content (pcy)
2	Number of lanes in each direction
9383	Average Daily Traffic (ADT)
0.2	Percent trucks in design lane (as decimal)
0	Growth type (0=no growth, 1=linear, 2=compound)
0	Growth rate (%)

a) Input file

September	654,864
October	885,429
November	1,872,463
December	2,967,838
January	2,963,955
February	3,067,968
March	2,435,752
April	1,279,306
May	619,809
June	425,248
July	287,206
August	303,234

b) Asphalt stiffness file

In order to determine the inputs needed for predicting the response of the BCOA using the ANNs, the joint spacing and  $l_{eff}$  can be easily calculated from the input file. Note that a default value of 0.18 is assumed for the Poisson's ratio of concrete. The normalized load-pavement weight ratio is  $q_m^* = \frac{P_i}{A \cdot \gamma_{eff} \cdot h_{eff}}$ .  $P_i$  is each load level  $i$  (lbs.), and  $\gamma_{eff}$  is 150 lbs/ft<sup>3</sup> for all calibration sections.

The modulus of subgrade reaction, k-value is taken directly from the input file.  $\frac{AGG}{k \cdot l_{eff}}$  can be calculated based on the LTE of the joint, modulus of subgrade reaction, and the effective radius of relative stiffness.  $AGG$  is a function of the LTE of the joint, which is defined based on the presence of dowels, aggregate interlock, and the underlying base layer. The LTE of the joint is determined using Equation 72 and converted back to  $AGG$  based on the work by Croveti [38].

$$LTE_{joint} = 100 \left[ 1 - \left( 1 - \frac{LTE_{dowel}}{100} \right) \left( 1 - \frac{LTE_{agg}}{100} \right) \left( 1 - \frac{LTE_{base}}{100} \right) \right] \quad (72)$$

where:

- $LTE_{dowel}$  is the joint LTE if dowels are the only mechanism of load transfer, %;
- $LTE_{agg}$  is the joint LTE if aggregate interlock is the only mechanism of load transfer, %;
- $LTE_{base}$  is the joint LTE if the base is the only mechanism of load transfer, %;
- $LTE_{base}$  is established using Table 30.

Table 30 –  $LTE_{base}$  for different base types [1].

Base type	$LTE_{base}$ (%)
Aggregate base	20
Asphalt-treated or cement-treated	30
Lean concrete base	40
Frozen base	90

If the pavement system is frozen, the LTE of joints increases [1]. To account for this, when the mean monthly mid-depth PCC temperature is less than 32°F,  $LTE_{base}$  is set equal to 90%. Additionally,  $LTE_{shoulder}$  is either 90%, if there is a tied concrete shoulder, or 0% for an asphalt shoulder. The wheel wander,  $s$ , is normally distributed with the mean located in the wheelpath and a standard deviation of 10 in. Korenev's non-dimensional temperature gradient,  $\Phi$ , is in accordance with Equation 39 presented in the previous section on the development of the ANNs. All variables in this equation have been previously defined with the exception of the temperature difference,  $\Delta T$ . In this procedure, the temperature difference is calculated as the EELTG established based on the equivalency of the differential energy and the diurnal transient non-linear gradients, as described above, plus the default value of the effective built-in temperature difference from Pavement ME of -10 °F [1].

In order to examine the effects of aggregate interlock on joint stiffness, the joint width must be estimated. The joint width for each month is calculated with Equation 73. The two variables that still need to be determined to calculate the joint width are the temperature of the PCC overlay at the time the concrete sets and the long-term drying shrinkage in the PCC overlay. The concrete set temperature is estimated using Table 31, which requires the mean monthly temperature for the month of paving as well as the cement content. The drying shrinkage strain in the PCC overlay is established based on the tensile strength (correlated from compressive strength) using the recommendations in AASHTO 93. This recommendation is shown in Table 32. The non-dimensional aggregate joint stiffness can then be calculated for each month using Equation 74 and 75 adopted from Zollinger et al. [46]. Note that  $\Delta S_{tot}$  is equal to zero for the first month of the analysis and the individual monthly increments of loss in shear capacity can be calculated using Equation 76.

$$JW(m) = \max (12000 * c * JTSpace * (CTE * (T_c - T(m)) + \epsilon_{sh}), 0) \quad (73)$$

where:

$JW(m)$  is the joint width for month  $m$ , mils;

$c$  is the friction factor (0.85 for asphalt layers when the joint only activates through the PCC layer and 0.65 for non-stabilized base layers when the joint activates through both the PCC and asphalt layers);

$JTSpace$  is the joint spacing in the overlay, ft;

$CTE$  is the overlay PCC coefficient of thermal expansion, in/in/°F;

$T_c$  is the concrete set temperature, °F;

$T(m)$  is the mean mid-depth PCC overlay temperature for month  $m$ , °F;

$\varepsilon_{sh}$  is the PCC overlay drying shrinkage strain, in/in.

Table 31 – PCC set temperature for cement content and mean temperature during month of paving (°F).

Mean monthly air temp. (°F)	Cement content (lbs.)			
	400	500	600	700
40	52	56	59	62
50	66	70	74	78
60	79	84	88	93
70	91	97	102	107
80	103	109	115	121
90	115	121	127	134
100	126	132	139	145

Table 32 – PCC overlay drying shrinkage strain relationship [1].

Tensile strength (psi)	Shrinkage strain (in/in)
400	0.0008
500	0.0006
600	0.00045
700	0.0003
800	0.0002

$$S = 0.5 * h_{PCC} * \exp^{-0.032*JW} - \Delta S_{tot} \quad (74)$$

$$\log(J_{AGG}) = -3.19626 + 16.09737 * \exp^{-\exp\left(-\frac{S-e}{f}\right)} \quad (75)$$

where:

$S$  is the aggregate joint shear capacity;

$h_{PCC}$  is the PCC overlay thickness, in;

$JW$  is the joint opening, mils;

$\Delta S_{tot} = \sum_{i=1}^m \Delta S_i$  is the cumulative loss of shear capacity at the beginning of the current month;

$J_{AGG}$  is the non-dimensional aggregate joint stiffness for the current monthly increment;

$e = 0.35$ ;

$f = 0.38$ .

$$\Delta S_i = \begin{cases} 0 & \text{if } JW < 0.001h_{pcc} \\ n_{i,A} * \frac{0.005 * 10^{-6}}{1.0 + \left(\frac{JW}{h_{pcc}}\right)^{-5.7}} \left(\frac{\tau_i}{\tau_{ref}}\right) & \text{if } 0.001 < JW < 3.8h_{pcc} \\ n_{i,A} * \frac{0.068 * 10^{-6}}{1.0 + 6.0 * \left(\frac{JW}{h_{pcc}} - 3\right)^{-1.98}} \left(\frac{\tau_i}{\tau_{ref}}\right) & \text{if } JW > 3.8h_{pcc} \end{cases} \quad (76)$$

where:

$\Delta S_i$  is the loss of shear capacity from all traffic for current month  $i$ ;

$n_{i,A}$  is the number of axle A load applications for load level  $i$ ;

$h_{pcc}$  is the overlay slab thickness, in;

$JW$  is the joint opening, mils;

$\tau_i = J_{AGG} * (\Sigma\delta_{L,m} - \Sigma\delta_{UL,m})$  is the shear stress on the transverse joint surface from the response model using corner deflections;

$\tau_{ref} = 111.1 * \exp(-\exp(0.9988 * \exp(-0.1089 * \log(J_{AGG}))))$  is the reference shear stress derived from the PCA test results.

For a doweled pavement, the model adopted for the non-dimensional dowel stiffness can be found elsewhere [1, 16]. The initial non-dimensional dowel joint stiffness is calculated using Equation 77 and the critical non-dimensional dowel joint stiffness is calculated with Equation 78. The non-dimensional dowel stiffness is then calculated using Equation 79 and the dowel damage parameter is presented in Equation 80.

$$J_0 = \frac{152.8 * A_d}{h_{pcc}} \quad (77)$$

$$J_d^* = \begin{cases} 118, & \text{if } \frac{A_d}{h_{pcc}} > 0.656 \\ 210.0845 \frac{A_d}{h_{pcc}} - 19.8, & \text{if } 0.009615 \leq \frac{A_d}{h_{pcc}} \leq 0.656 \\ 0.4, & \text{if } \frac{A_d}{h_{pcc}} < 0.009615 \end{cases} \quad (78)$$

$$J_d = J_d^* + (J_0 - J_d^*) \exp(-DOWDAM) \quad (79)$$

$$\Delta DOWDAM = \frac{J_d * (\Sigma\delta_{C,A,m}) * DowelSpace * n_{i,A}}{d * f'_c} \quad (80)$$

where:

$A_d$  is the area of the dowel bar, in<sup>2</sup>;

$h_{pcc}$  is the overlay PCC thickness, in;

$J_0$  is the initial non-dimensional dowel stiffness;

$J_d^*$  is the critical non-dimensional dowel stiffness;

$J_d$  is the non-dimensional dowel stiffness for current month;

$DOWDAM$  is the cumulative dowel damage for the current month;  
 $DowelSpace$  is the dowel bar spacing, in;  
 $n_{i,A}$  is the number of axle A load applications for load level  $i$ ;  
 $d$  is the dowel bar diameter, in;  
 $f'_c$  is the PCC compressive stress estimated from the modulus of rupture, psi.

Two sets of incremental equations are used to determine faulting. The first set is for when the joint activates only through the PCC layer and the second set is for when the joint activates through both the PCC and asphalt layers. The difference between the two sets of equations is the treatment of the erodibility of the layer/material when undergoing pumping. The differential energy is calculated using the corresponding ANNs for the different joint activation depths. The erodibility factor of the layer being eroded away is also dependent on the depth of joint activation. If the joint is likely to only activate through the PCC layer, previously an erodibility value of one is assigned based on the erosion assessment established in the Pavement ME [1, 16]. However, a new approach was developed to account for the different material properties of the asphalt layer and is presented below.

$$E = fn(\% \text{ eff. binder content, } \% \text{ air voids, } P_{200}) \quad (81)$$

where:

- $\% \text{ eff. binder content}$  is the percent effective binder content in the asphalt mixture, %;
- $\% \text{ air voids}$  is the percent air voids in the asphalt mixture, %;
- $P_{200}$  is the percent fines passing the number 200 sieve, %.

The erodibility classification established in the Pavement ME is used when a joint activates through both the PCC and asphalt layer. An erodibility factor of four is assigned based on the likelihood of erosion in the different underlying layers beneath an asphalt layer as shown in Table 33. In addition to this erodibility classification, the percent aggregate passing the No. 200 sieve of the layer beneath the asphalt is an input.

Table 33 – Erodibility classification (adopted from [1]).

<b>Erodibility class</b>	<b>Material description and testing</b>
1	Hot mixed asphalt concrete with 6 percent asphalt cement that passes appropriate stripping tests and aggregate tests and a granular subbase layer or a stabilized soil layer (otherwise Class 2).
2	Asphalt treated granular material with 4 percent asphalt cement that passes appropriate stripping test and a granular subbase layer or a treated soil layer or a geotextile fabric is placed between the treated base and subgrade; otherwise Class 3.
3	Asphalt treated granular material with 3 percent asphalt cement that passes appropriate stripping test.
4	Unbound crushed granular material having dense gradation and high-quality aggregates.
5	Untreated soils (PCC slab placed on prepared/compacted subgrade)



When the joint activates only through the PCC, faulting can be predicted using Equations 82 through 85.

$$F_0 = (C_1 + C_2 * FR^{0.25}) * \delta_{curl} * [C_5 * E]^{C_6} * \log(WETDAYS * A_{P200}) \quad (82)$$

$$F_i = F_{i-1} + C_7 * C_8 * DE_i * [C_5 * E]^{C_6} \quad (83)$$

$$\Delta Fault_i = (C_3 + C_4 * FR^{0.25}) * (F_{i-1} - Fault_{i-1})^2 * C_8 * DE_i \quad (84)$$

$$Fault_i = Fault_{i-1} + \Delta Fault_i \quad (85)$$

where:

$F_0$  is the initial maximum mean transverse joint faulting, in;

$FR$  is the base freezing index defined as the percentage of the time that the top of the asphalt is below freezing ( $<32^\circ\text{F}$ );

$\delta_{curl}$  is the maximum mean monthly PCC upward slab corner deflection due to temperature curling and moisture warping, in;

$E$  is the erodibility factor of the asphalt layer as a function of the asphalt mixture properties;

$WETDAYS$  is the average number of annual wet days ( $> 0.1$  in of precipitation);

$A_{P200}$  is the percent of aggregate passing No. 200 sieve in the asphalt layer, %;

$F_i$  is the maximum mean transverse joint faulting for month  $i$ , in;

$F_{i-1}$  is the maximum mean transverse joint faulting for month  $i-1$ , in;

If  $i=1$ ,  $F_{i-1} = F_0$ ;

$DE_i$  is the differential energy density accumulated during month  $i$ ;

$\Delta Fault_i$  is the incremental monthly change in mean transverse joint faulting during month  $i$ , in;

$C_1 \dots C_8$  are the calibration coefficients;

$Fault_{i-1}$  is the mean joint faulting at the beginning of month  $i$  (0 if  $i = 1$ );

$Fault_i$  is the mean joint faulting at the end of month  $i$ , in.

When the joint activates through the PCC and asphalt layer, faulting can be predicted using Equations 86 through 89.

$$F_0 = (C_1 + C_2 * FR^{0.25}) * \delta_{curl} * \left[ \log(1 + C_5 * 5^{EROD}) * \log\left(\frac{P_{200} * WETDAYS}{\rho_s}\right) \right]^{C_6} \quad (86)$$

$$F_i = F_0 + C_7 \sum_{j=0}^m DE_j * \log(1 + C_5 * 5^{EROD})^{C_6} \quad (87)$$

$$\Delta Fault_i = (C_3 + C_4 * FR^{0.25}) * (F_{i-1} - Fault_{i-1})^2 * C_7 * DE_i \quad (88)$$

$$Fault_i = Fault_{i-1} + \Delta Fault_i \quad (89)$$

where:

$F_0$  is the initial maximum mean transverse joint faulting, in;  
 $FR$  is the base freezing index defined at the percentage of the time that the top of the base is below freezing ( $<32^\circ\text{F}$ );  
 $\delta_{curl}$  is the maximum mean monthly PCC upward slab corner deflection due to temperature curling and moisture warping, in;  
 $EROD$  is the erodibility of the layer beneath the asphalt, as defined in Table 33 above;  
 $P_{200}$  is the percent of aggregate passing No. 200 sieve of the layer beneath the asphalt (%);  
 $WETDAYS$  is the average number of annual wet days ( $> 0.1$  in of rainfall);  
 $\rho_s$  is the overburden on the layer beneath the asphalt, lbs;  
 $F_i$  is the maximum mean transverse joint faulting for month  $i$ , in;  
 $F_{i-1}$  is the maximum mean transverse joint faulting for month  $i-1$ , in (If  $i=1$ ,  $F_{i-1} = F_0$ );  
 $DE_i$  is the differential energy density accumulated during month  $i$ ;  
 $\Delta Fault_i$  is the incremental monthly change in mean transverse joint faulting during month  $i$ , in;  
 $C_1 \dots C_7$  are the calibration coefficients;  
 $Fault_{i-1}$  is the mean joint faulting at the beginning of month  $i$  (0 if  $i = 1$ ), in;  
 $Fault_i$  is the mean joint faulting at the end of month  $i$ , in.

When there is a section that is likely to have both depths of joint activation based on the FSR, the individual models need to be coupled together. In order to determine the likelihood of the different depths of joint activation within a given section, an extensive study was performed and the results are presented in previous studies [18, 20, 39]. It was determined that approximately every sixth joint will activate full-depth. This may vary for different structures but is believed to be a suitable approximation. Therefore, the following equation is used to calculate average joint faulting for sections that have joints that activate to different depths.

$$Fault_m = \sum_{i=1}^m \left( \frac{5}{6} \Delta Fault_{PCC,i} + \frac{1}{6} \Delta Fault_{Full,i} \right) \quad (90)$$

where:

$Fault_m$  is the mean joint faulting at the end of month  $m$ , in;  
 $\Delta Fault_{PCC,i}$  is the incremental monthly change in mean transverse joint faulting during month  $i$  when the joint is only through the PCC layer, in;  
 $\Delta Fault_{Full,i}$  is the incremental monthly change in mean transverse joint faulting during month  $i$  when the joint is through the PCC layer and the asphalt layer, in.

The next step in this research effort is to use the results from Task 3 to develop a fully calibrated faulting model that can be incorporated into the BCOA-ME design process.

## 4.4 Model calibration

The entire calibration database was introduced in Section 4.1 with Table 12 – Range of parameters for calibration sections. presenting the range of parameters used for developing the model. Two separate calibrations needed to be assembled in order to account for the different trends in faulting due to the different depths of joint activation. Table 34 and Table 35 presents details about individual sections used in the calibration of the model considering joint activation through PCC only and through both PCC and asphalt, respectively. As mentioned before, of all sections, 29 are undoweled, while the rest are doweled with a dowel diameter of 1 in. For calibrating the two models, 154 data points were available for PCC only activation and 115 for PCC and asphalt joint activation (total of 269 datapoints). Short slabs (joint spacing  $\leq 4.5$  ft) were not included in the calibration as their mechanism of faulting is usually different from the one considered here, as discussed above.

Table 34 - Calibrations sections for joint activation through PCC only.

Section ID	State	Overlay thickness, in	Asphalt thickness, in	Panel size, ft x ft	Dowel diameter, in	Estimated ESALs
Cell 60_PCC	MN	5	7	5x6	None	8.45E+06
Cell 60_PL_PCC	MN	5	7	5x6	None	1.70E+06
Cell 96_PCC	MN	6	7	5x6	None	1.25E+07
Cell 96_PL_PCC	MN	6	7	5x6	None	3.50E+06
Cell 61_PCC	MN	5	7	5x6	None	8.45E+06
Cell 61_PL_PCC	MN	5	7	5x6	None	1.70E+06
Cell 62_PCC	MN	4	8	5x6	None	8.45E+06
Cell 62_PL_PCC	MN	4	8	5x6	None	1.70E+06
Cell 63_PCC	MN	4	8	5x6	None	8.45E+06
Cell 63_PL_PCC	MN	4	8	5x6	None	1.70E+06
06-83A	CO	8	16	6x6	None	5.91E+06
06-83B	CO	6	13	6x6	None	1.02E+07
06-121A	CO	6	13	6x6	None	3.13E+06
06-121B	CO	7	12	6x6	None	4.39E+06
17-27	IL	5	8	5.5x5.5	None	1.00E+07
22-167	LA	5	9	4x4	None	5.57E+06
29-60	MO	4.5	5	4x4	None	1.91E+07

Table 35 - Calibrations sections for joint activation through both PCC and HMA.

Section ID	State	Overlay thickness, in	Asphalt thickness, in	Panel size, ft x ft	Dowel diameter, in	Estimated ESALs
Cell 92_FULL	MN	6	7	10x12	1	1.16E+07
Cell 92_PL_FULL	MN	6	7	10x12	1	3.19E+06
CSAH 9	MN	7	6	15x12	1	4.35E+05
TH 56_2006-26	MN	6	8.5	15x13.5	1	9.06E+04
06-6	CO	6	9	10x12	1	4.69E+06
Cell 95_FULL	MN	3	10	5x6	None	4.76E+06
Cell 60_FULL	MN	5	7	5x6	None	8.45E+06
Cell 60_PL_FULL	MN	5	7	5x6	None	1.70E+06
Cell 61_FULL	MN	5	7	5x6	None	6.20E+06
Cell 61_PL_FULL	MN	5	7	5x6	None	1.14E+06
Cell 97_FULL	MN	6	7	10x12	None	1.16E+07
CSAH 7_43-607-14	MN	5	6	6x6,6x7	None	3.26E+05
CSAH 22_CP 12-14-22	MN	6	4	6x6	None	1.69E+05
CSAH 22_002-622-033	MN	6	4	6.25x6.25	None	1.28E+05
TH 30_0705-14	MN	6	7.5	12x12	None	3.39E+05
CSAH 22_02-622-31	MN	6	3	6x6,6x7	None	2.26E+05
CSAH 2_43-602-(24-25)	MN	5	5	6x6,6x7	None	2.19E+05

Calibration requires estimation of coefficients  $C_1 - C_8$  introduced later for both activation depths, as well as the erosion model, such that the overall error between the measured and predicted data was minimized.

For the erosion model, in addition to the sections listed in Table 12, additional data from several unbonded overlay (UBOL) sections were used to improve the fit. These sections can be found elsewhere [47]. The erodibility factor of these UBOL sections was scaled up to represent additional damage to the section, as would be the case for BCOA sections (UBOL is typically used for relatively less damaged sections as compared to BCOA). The scaling factor was chosen empirically to obtain the best fit. The final fitted erosion model can be seen in Equations 91 and 92.

$$\alpha = \log(1 + a \times P_{200} + b \times \%AV + c \times (10 - \%Binder)) \quad 91$$

$$E = \begin{cases} (-1.195\alpha^2 + 4.1115\alpha - 1.823) & \text{Undoweled Pavements} \\ (-1.016\alpha^2 + 3.495\alpha - 1.550) & \text{Doweled Pavements} \end{cases} \alpha > 0.56 \quad 92$$

$$E = \begin{cases} (0.108 * \alpha) & \text{Undoweled Pavements} \\ (0.091 * \alpha) & \text{Doweled Pavements} \end{cases} \alpha < 0.56$$

Where:

$\alpha$  is the erodibility index.

$a, b, c$  are the calibration coefficients (0.75, 0.06, and 0.17, respectively).

$P_{200}$  is the percent aggregate passing No. 200 sieve for the asphalt, %.

%AV is the air voids percentage in the asphalt, %.

%Binder is the effective binder content of the asphalt, % (max. value =10%)

Predicted versus measured transverse joint faulting is presented for both models in Figure 81. Table 36 summarizes the calibration coefficients. In addition, the Pavement ME JPCP faulting national calibration coefficients are included for comparison purposes.

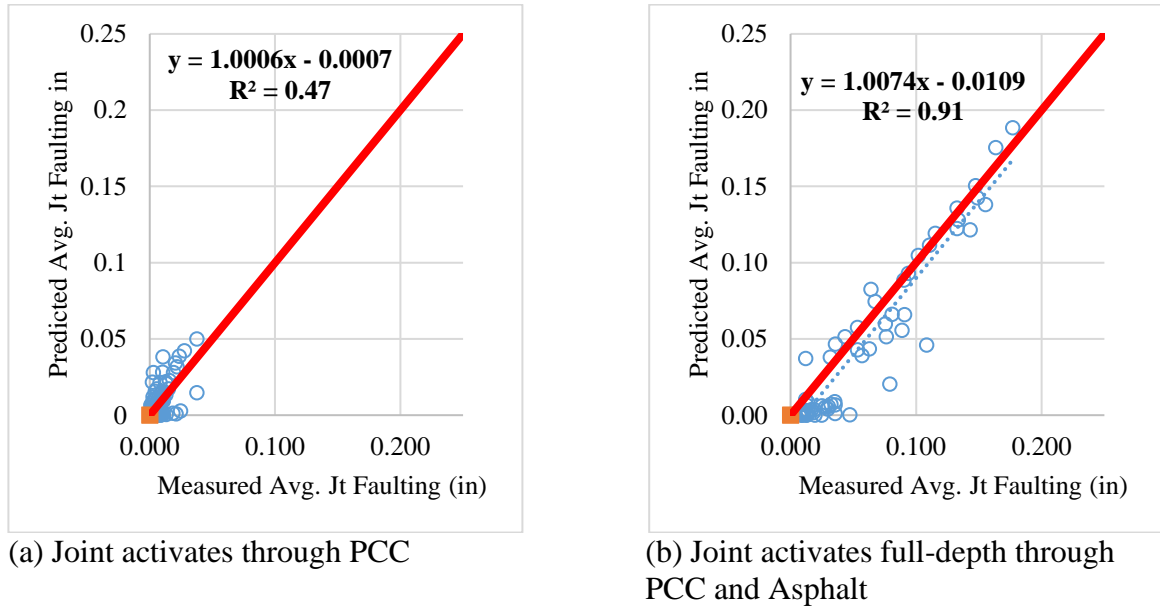


Figure 81 - Measured vs predicted faulting

Table 36 - Calibration coefficients

Calibration coefficient	Joint activates through PCC	Joint activates full depth	Pavement ME initial	Pavement ME current
C <sub>1</sub>	1.29	1.29	1.29	0.595
C <sub>2</sub>	1.1	1.1	1.1	1.636
C <sub>3</sub>	0.001725	1.0E-06	0.001725	0.00217
C <sub>4</sub>	0.0008	1.0E-05	0.0008	0.00444
C <sub>5</sub>	0.05	6.0E-04	250	250
C <sub>6</sub>	2.2	4.275	0.4	0.47
C <sub>7</sub>	3.245	1.27/5E-04	1.2	7.3
C <sub>8</sub>	1/5E-06	-	400	400
<b>Doweled: C<sub>7</sub></b>	0.1	(48.0*dowel diameter)* C <sub>7</sub>		

#### 4.4.1 Reliability model

Finally, the faulting predicted from the aforementioned model, which is at 50% reliability, needs to be scaled to a user-defined reliability  $R$ . The general model for this is as shown in Equation 93.

$$FAULT_R = FAULT - Stdev(FAULT) \times Z_R \quad (93)$$

Where,

$FAULT_R$  is the magnitude of faulting at the desired level of reliability R, in.

$FAULT$  is the predicted faulting determined corresponding to 50 percent reliability, in.

$Stdev(FAULT)$  is the standard deviation of the predicted faulting using the corresponding established reliability model, in.

$Z_R$  is the standardized normal deviate corresponding to a reliability level R, presented in Table 37.

85% reliability is recommended.

Table 37 - Reliability and corresponding standardized normal deviate.

Reliability, R (%)	Std. normal deviate, $Z_R$
50	0
75	-0.674
85	-1.037
90	-1.282
95	-1.645

The standard deviation model was developed similar to Pavement ME and are shown in Equations 94 and 95 for joint activation through only the PCC layer and both the PCC and HMA layers respectively.

$$Stdev(FAULT\_PCC) = 0.1259 * (FAULT\_PCC^{0.5784}) \quad (94)$$

Where:

$Stdev(FAULT\_PCC)$  is the transverse joint faulting standard deviation when the joint only activates through the PCC, in.

$FAULT\_PCC$  is the predicted transverse joint faulting when the joint only activates through the PCC, in.

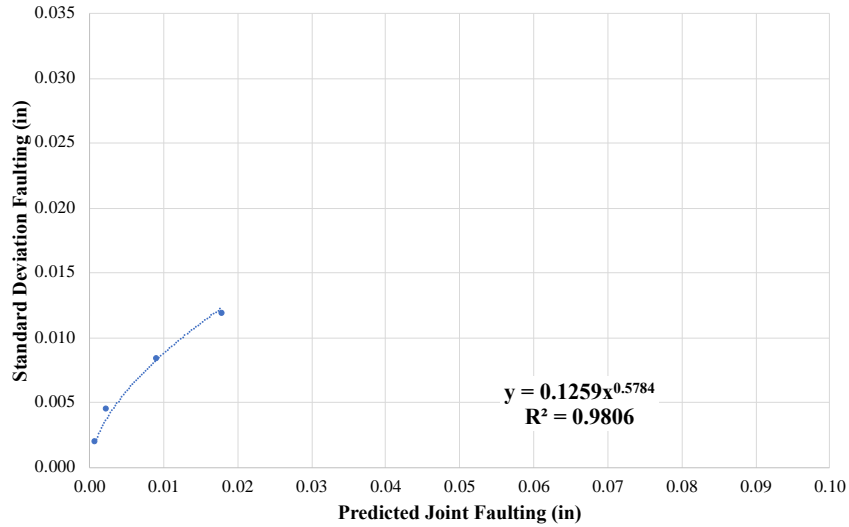
$$Stdev(FAULT\_FULL) = 0.0170 * (FAULT\_FULL^{0.1239}) \quad (95)$$

Where:

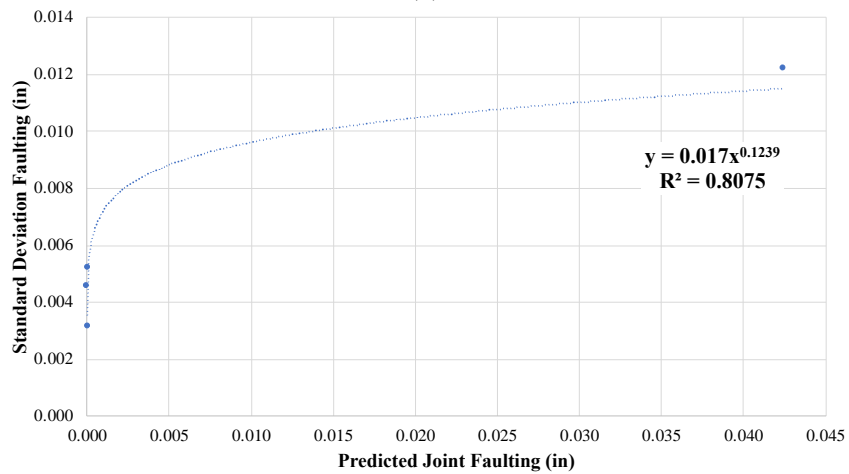
$Stdev(FAULT\_FULL)$  is the transverse joint faulting standard deviation when the joint activates through the PCC and asphalt layers, in.

$FAULT\_FULL$  is the predicted transverse joint faulting when the joint activates through the PCC and asphalt layers, in.

Figure 82 shows the goodness of fit of these models.



(a)



(b)

Figure 82 - Reliability models for joint activation through (a) PCC only and (b) both PCC and HMA

#### 4.4.2 Examples

Examples of measured and predicted faulting from some sections in MnROAD are shown in Figure 83. These include sections that experience joint activation through both the PCC and asphalt layers (joint spacing  $\geq 10$  ft), and through the PCC layer only (joint spacing  $< 10$  ft). All of these sections, except Cell 95, were used to perform the calibration. Cell 95 is of particular interest since this section has fiber-reinforced concrete, which results in the observed faulting to be less than the predicted, since the presence of fibers is not currently accounted for in the faulting prediction model.

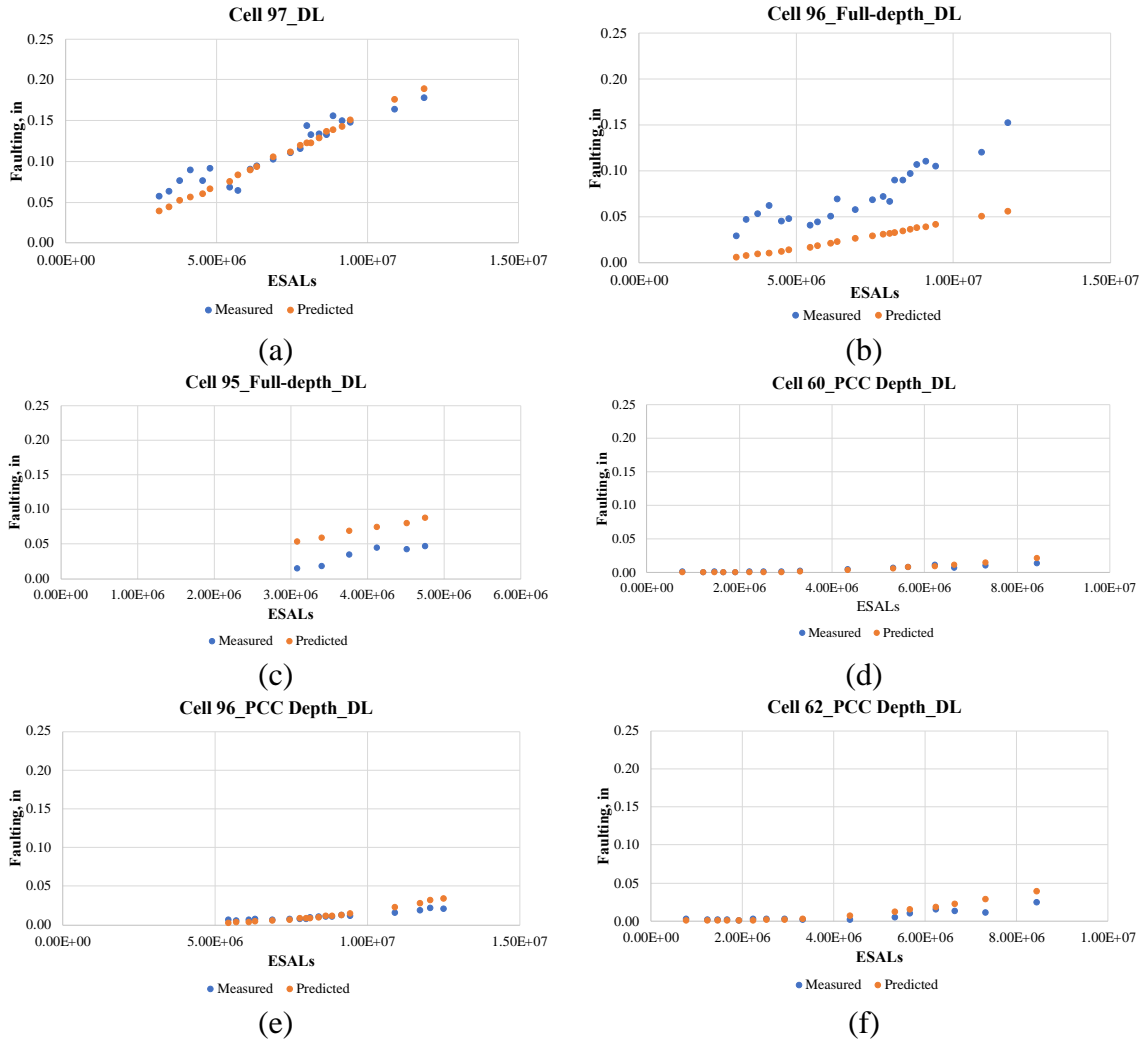


Figure 83 - Predicted and measured faulting as a function of ESALs for MnROAD sections: (a)-(c) show faulting in sections with joint activation through both the PCC and asphalt, while (d)-(f) through the PCC only.

## 4.5 BCOA-ME Webtool


The newly developed faulting model for BCOAs was incorporated into the existing webtool, BCOA-ME. The existing tool designed BCOA sections to achieve a desired level of performance in terms of fatigue cracking over a specified design life and level of reliability. The final output was a design thickness of the PCC overlay. With the new faulting model, an additional analysis that evaluates the faulting in the section using the design thickness (based on the fatigue cracking model) is performed, and a graph showing cumulative faulting as a function of design life is presented to the user. Several screenshots of the model are shown in Table 38 below.

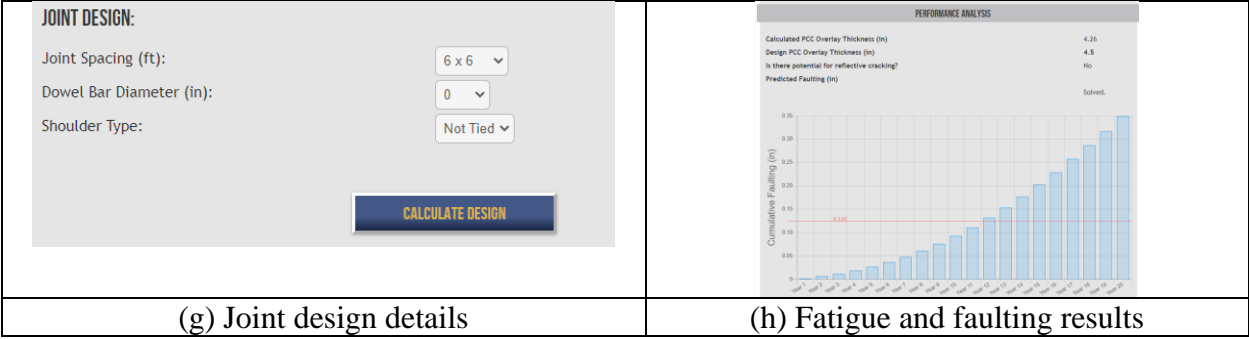
The model is available at:



- [https://www.engineering.pitt.edu/Sub-Sites/Faculty-Subsites/J\\_Vandenbossche/BCOA-ME/BCOA-ME-Design-Guide/](https://www.engineering.pitt.edu/Sub-Sites/Faculty-Subsites/J_Vandenbossche/BCOA-ME/BCOA-ME-Design-Guide/)

Table 38 – BCOA-ME webtool with faulting calculation

 <p>(Last site update Jan. 2016; Last guide update April 2015)</p> <p>The bonded concrete overlay of asphalt mechanistic-empirical design procedure (BCOA-ME) was developed at the University of Pittsburgh under the FHWA Pooled Fund Study TPF 5-165. This pavement structure has been referred to as thin and ultra-thin whitetopping. This site is a repository for all information relating to the BCOA-ME. The information has been sorted based on its intended use and can be retrieved by clicking on the appropriate tab below. The BCOA-ME can be run directly from this site by clicking on the "Design Guide" tab below.</p>	<p><b>GENERAL INFORMATION</b></p> <p>Latitude (degree): 44.53 <span>Geographic Information</span></p> <p>Longitude (degree): -93.14</p> <p>Elevation (ft): 874</p> <p>Estimated Design Lane ESALs: 0 <span>ESALS Calculator</span></p> <p>Maximum Allowable Percent Slabs Cracked (%): 25</p> <p>Desired Reliability against Slab Cracking (%): 85</p>
<p>(a) Main landing page</p>	<p>(b) Geographic information inputs</p>
<p><b>ESALS ESTIMATION:</b></p> <p>Is One-Way ADT Available? <input checked="" type="radio"/> Yes <input type="radio"/> No</p> <p><b>ESTIMATE ESALS:</b></p> <p>Design Life (yrs): 20</p> <p>Terminal Serviceability: 2</p> <p>Number of Lanes in Each Direction: 2</p> <p>Percent Trucks(%): 7</p> <p>ADTT Growth Rate (%): 3</p> <p>Traffic Growth Rate Type: Non linear</p> <p>Road Category: Major arterial</p> <p>One-Way Average Daily Traffic (ADT): 20000</p> <p><span>CANCEL</span> <span>SUBMIT</span></p>	<p><b>CLIMATE</b></p> <p>AMDAT Region ID 5</p> <p>Map of Sunshine Zone 2</p>
<p>(c) Traffic inputs</p>	<p>(d) Climate inputs</p>
<p><b>EXISTING STRUCTURE</b></p> <p>Post-milling HMA Thickness (in): 6</p> <p>Composite Modulus of Subgrade Reaction, k-value (psi/in): 150 <span>k-Value Calculator</span></p> <p>Does the existing HMA pavement have transverse cracks? <input checked="" type="radio"/> Yes <input type="radio"/> No <span>Transverse Cracking</span></p> <p>HMA Fatigue: Adequate <span>Fatigue Cracking Example</span></p> <p><b>HMA PROPERTIES IN THE WHEELPATH:</b></p> <p>P200 of HMA (%): 4.3</p> <p>P200 of subbase (%): 50</p> <p>Effective Binder Content by Volume (%): 12.5</p>	<p><b>PCC OVERLAY PROPERTIES</b></p> <p><b>PCC PROPERTIES:</b></p> <p>Average 28-day Flexural Strength (three-point ben): 650</p> <p>Estimated PCC Elastic Modulus (psi): 4000000 <span>Epcc Calculator</span></p> <p>Coefficient of Thermal Expansion (10<sup>-6</sup> in/°F/in): 5.5 <span>CTE Calculator</span></p> <p>Cement Content (lb/cyd): 550</p> <p>Fiber Type: No Fibers</p>
<p>(e) Details of existing HMA</p>	<p>(f) PCC overlay details</p>



The model can easily be used by pavement design engineers to evaluate the development of faulting in a BCOA using the model developed in the present study, thus ensuring seamless technology transfer.

## 5 CONCLUSIONS

Joint transverse faulting is a distress that significantly impacts pavement ride quality affecting infrastructure and vehicle costs. Accurate prediction of faulting development is essential for a proper pavement design. The Pennsylvania Department of Transportation (PennDOT) identified issues with the prediction of transverse joint faulting for jointed plain concrete pavements (JPCP) using the current AASHTOWare Pavement ME which includes local calibration. In addition, a faulting model that simulates the peculiar characteristic of bonded concrete overlays of asphalt (BCOA) was unavailable. Faulting for BCOA design could previously only be estimated based on models developed for JPCP, a different pavement with a different structural behavior. To address these issues, this project had two main goals:

1. Modify the current Pavement ME model for JPCP faulting prediction to better capture faulting development in Pennsylvania introducing a new methodology to use road management system (RMS) data for model evaluation, calibration, and validation.
2. Develop a singular faulting model that encompasses the design aspects specific to that of a BCOA structure.

For JPCP, an analysis of transverse joint faulting from field data from PennDOT's RMS collected allowed the following observations:

- The PennDOT RMS database provides valuable information on faulting performance;
- Pennsylvania JPCP shows a good performance regarding faulting as more than half of the analyzed field segments present no faulting;
- Poor correlations of field average faulting with pavement age, cumulative traffic, and IRI for the entire RMS dataset can be linked to pavement rehabilitation;
- The analysis of faulting greater than the 90<sup>th</sup> percentile level improves faulting correlation with cumulative traffic also showing the benefits of a shorter joint spacing and treated bases;

A comparative analysis of field data with faulting predictions the AASHTOWare Pavement ME in comparison with field data shows that the model (PA calibration) overpredicts joint faulting, especially, for high traffic levels and large joint spacing. The overall conclusion of this prediction evaluation is that the Pavement ME model requires a recalibration or a modification to better represent Pennsylvania JPCP faulting performance in order to more accurately design new pavements. The RMS data was sufficient to perform this procedure.

Since pavements are usually designed for high levels of reliability, results show that RMS databases are an appropriate resource for model calibration due to the large amount of data collected. However, the consideration of potential rehabilitated sections within distresses databases is imperative for the model calibration and validation. By equalizing the average measured and predicted faulting within a subdivided calibration database, the effect of unknown rehabilitated sections is taken into account.

Considering the results of the reliability study, the current model exhibited deficiencies in faulting prediction for various base types and also in mid-range and long-term faulting development. The former was addressed by enhancing the model with parameters and coefficients that correlated

additional drainage, percentage of fine material, and number of wet days. The latter was addressed by calibrating the model coefficients making the faulting development curve less steep. Validation with field data considering potential rehabilitated sections confirmed the modified model accuracy in comparison to the conservative predictions of the current model.

A sensitivity analysis of the modified faulting model showed coherent results. Using the modified model allows design of JPCP for high levels of traffic which can result in satisfactory pavement performance. The modified model predictions were compared with the Pavement ME faulting predictions. It was demonstrated that the modified model predictions are more realistic. A program called PittFaultCompanion was developed as part of this project to facilitate faulting prediction using the new model.

For BCOA, prior to this work a faulting model that considers the structural design of a BCOA and that was calibrated using the performance data from a BCOA was not available. A faulting prediction requires a combination of a structural response model and a calibrated faulting model that incorporates measured field data, engineering judgment, and uncertainty. In the present study, the faulting model was developed for medium- and large-sized slabs. Short slabs (joint spacing  $\leq$  4.5 ft) were not considered due to lack of performance data.

A series of Artificial Neural Networks (ANNs) were developed and validated to predict the Differential Energy (DE) of a BCOA system. The DE is used to quantify damage created through the difference in the deflection basins between the loaded and unloaded slabs, and is directly related to the accumulation of faulting. For BCOA, faulting can develop at the top of the asphalt layer when the joint activates only through the PCC or the top of the layer beneath the asphalt when the joint activates full-depth. Consequently, separate calibration models were developed for each case. The calibration showed good agreement with the measured data and an uncertainty model was also developed to account for variation in the field. The model was used to analyze the sensitivity of various parameters before being incorporated into the BCOA-ME program.

Faulting is a common distress in JPCP and BCOAs. Comprehensive modeling of this distress can substantially impact how a pavement is designed and can help to create successful designs that efficiently carry the demanded loads. This project improves upon the standard design procedure for Pennsylvania by modifying the existing JPCP faulting model and introducing a new model for BCOA. The results of the project can better assist in properly choosing the optimum parameters for each project design to improve the ride quality and pavement life cycle without overdesign.

## References

1. Applied Research Associates (ARA), Inc., ERES Division. Guide for Mechanistic-Empirical Design of New and Rehabilitated Pavement Structures. **Final Report NCHRP 1-37A**. Transportation Research Board of the National Academies, Washington, D.C., 2004.
2. **Permanent International Association of Road Congresses. Combating Concrete Pavement Slab Pumping by Interface Drainage and Use of Low Erodability Materials: State of the Art and Recommendations**, Permanent International Association of Road Congresses, Paris, France, 1987.
3. Khazanovich, L. and Tompkins, D. Incorporating Slab/Underlying Layer Interaction into the Concrete Pavement Analysis Procedures. (**Program NCHR**, ed.). The National Academies Press; 2017. doi:10.17226/24842
4. Larralde, J. **Structural Analysis of Rigid Pavements with Pumping**. Ph.D. thesis, Purdue University, West Lafayette, IN, 1984.
5. Van Wijk, A.J., J. Larralde, C. W. Lovell, and W. F. Chen. Pumping Prediction Model for Highway Concrete Pavements. ASCE, **Journal of Transportation Engineering**, Vol. 115, No. 2, 1989, pp. 161-175.
6. Bhatti, M.A., J. A. Barlow, and J. W. Stoner. Modeling Damage to Rigid Pavements Caused by Subgrade Pumping. ASCE, **Journal of Transportation Engineering**, Vol. 122, No. 1, Jan-Feb 1996, pp. 12-21.
7. Zollinger, D.G., N. Buch, D. Xin, and J. Soares. Performance of CRCP Volume 6 - CRCP Design, Construction, and Performance. **FHWA-RD-97-151**, Report, U.S. Department of Transportation, Washington, DC, February 1998.
8. Ioannides, A.M., and G.T. Korovesis. Analysis and Design of Doweled Slab-On-Grade Pavement Systems. **Journal of Transportation Engineering**, ASCE, Vol. 118, No. 6, New York, NY, pp. 745-768, 1992.
9. Khazanovich, L., M. Darter, R. Bartlett, and T. McPeak. Common Characteristics of Good and Poorly Performing PCC Pavements. **Report No. FHWA-RD-97-131**. Federal Highway Administration, 1998.
10. Selezneva, O., Jiang J. and Tayabji, S. D. Preliminary Evaluation and Analysis of LTPP Faulting Data – Final Report. **Report No. FHWA-RD-00-076**. Federal Highway Administration, 2000.
11. NCHRP. Changes to the Mechanistic-Empirical Pavement Design Guide Software through Version 0.900. NCHRP Research Results Digest 308, **NCHRP Project 1-40D**, Transportation Research Board, National Research Council, Washington, DC., 2000.
12. Sachs, S., Vandenbossche, J., and M. Snyder. Developing Recalibrated Concrete Pavement Performance Models for the Mechanistic-Empirical Pavement Design. **NCHRP Project 20-07(327)**. National Cooperative Highway Research Program, Transportation Research Board, Washington, DC., 2014.
13. Bhattacharya, B. B., D. Raghunathan, O. Selezneva, P. Wilke, M. I. Darter, and H. L. Von Quintus. PennDOT Pavement ME Design Preliminary User Input Guide (**Draft Report**). Pennsylvania Department of Transportation, Harrisburg, PA, 2017.
14. Darter, M., L. Khazanovich, T. Yu, and J. Mallela. Reliability Analysis of Cracking and Faulting Prediction in the New Mechanistic-Empirical Pavement Design Procedure. **Transportation Research Record: Journal of the Transportation Research Board**, 1936, 2015, 150–160.

15. Mu, F., J. W. Mack, and R. A. Rodden. Review of National and State-Level Calibrations of the AASHTOWare Pavement ME Design for New Jointed Plain Concrete Pavement. **Proceedings of the 2015 International Airfield and Highway Pavements Conference**, Miami, FL, 2015 708–719.
16. Khazanovich, L., M. Darter, H.T. Yu. Mechanistic-Empirical Model to Predict Transverse Joint Faulting. **Transportation Research Record: Journal of the Transportation Research Board**, 1896, 2004, 34-45.
17. Echevarria, C. E. B.; Vidal, J. P. C. Adaptacion y calibracion de modelo de escalonamento a pavimentos optimizados de hormigon. **Proceedings of the 13th PROVIAL International Congress (in Spanish)**, Arica, Chile, 2018.
18. DeSantis, J.W., J.M. Vandenbossche, K. Alland, S. Sachs, T. Burnham, and A. Montenegro. Joint Performance in Bonded Concrete Overlays of Asphalt. **Proceedings of the 11th International Conference for Concrete Pavements (ICCP)**. San Antonio, TX, 2016, pp. 638-660.
19. ABAQUS Inc. ABAQUS software version 6.13: Analysis user’s manual. ABAQUS Inc., Providence, RI, 2013.
20. DeSantis, J.W., S. Sachs, and J.M. Vandenbossche. Faulting Development in Concrete Overlays and Pavements. **International Journal of Pavement Engineering**, 2019, pp. 1-16.
21. Crovetti, J.A. Design and Evaluation of Jointed Concrete Pavement Systems Incorporating Open-Graded Permeable Bases. Ph.D. Dissertation, University of Illinois at Urbana-Champaign. 1994.
22. Guo, E., L. Ricalde, and I. Kawa. FAA Finite Element Design Procedure for Rigid Pavements. **Report No. DOT/FAA/AR-07/33**. Federal Aviation Administration, Washington, D.C., 2007.
23. Davids, W., G. Turkiyyah, and J. Mahoney. EverFE: Rigid Pavement Three-Dimensional Finite Element Analysis Tool. **Transportation Research Record: Journal of the Transportation Research Board**, No. 1629, 1998, pp. 41-49.
24. Kuo, C.M. Three-dimensional Finite Element Analysis of Concrete Pavement. PhD Dissertation, University of Illinois at Urbana-Champaign, 1994.
25. Vandenbossche, J.M., N. Dufalla, and Z. Li, Bonded Concrete Overlay of Asphalt Mechanistic-Empirical Design Procedure. **International Journal for Pavement Engineering**, Vol. 18, No. 11, 2016, pp. 1-12.
26. Burnham, T.R. Construction Report for MnROAD Thin Whitetopping Test Cells 60-63. **Report MN/RC – 2006-18**. 2006.
27. Vandenbossche, J. M. and A. J. Fagerness. Performance, Analysis, and Repair of Ultrathin and Thin Whitetopping at Minnesota Road Research Facility. **Transportation Research Record: Journal of the Transportation Research Board**, No. 1809, 2002, pp. 191-198.
28. Barman, M., F. Mu, and J.M. Vandenbossche. Development of a Rational of Mechanistic-Empirical Based Design Guide for Thin and Ultra-thin Whitetopping: **Task 1 Report**. University of Pittsburgh, Pittsburgh, PA, 2011.
29. Mu F. and J.M. Vandenbossche. Development of a Rational of Mechanistic-Empirical Based Design Guide for Thin and Ultra-Thin Whitetopping. **Task 2 Report: Review and Selection of Structural Response Models**. University of Pittsburgh, Pittsburgh, PA, 2011.
30. Li, Z., J.M. Vandenbossche, and N. Dufalla. Structural Model for Longitudinal Cracking in Bonded Whitetopping with a 1.83-m x 1.83-m (6-ft x 6-ft) Joint Spacing. **American Society**

- of Civil Engineering Journal of Transportation Engineering, Part B: Pavements**, Vol. 143, No. 4, 2017.
31. Li, Z., and J.M Vandenbossche. Redefining the Failure Mode for Thin and Ultra-thin Whitetopping with a 1.8-x1.8-m (6-x6-ft) Joint Spacing. **Transportation Research Record: Journal of the Transportation Research Board**, No. 2368, 2013, pp. 133-146.
  32. Li, Z., Dufalla, N., Mu, F., and Vandenbossche, J.M. Bonded Concrete Overlay of Asphalt Pavements Mechanistic-Empirical Design Guide (BCOA-ME). Theory Manual, **FHWA TFP study**, Vol. 5, 2013, pp. 165.
  33. DeSantis, John W., Julie M. Vandenbossche, and Steven G. Sachs. Artificial Neural Networks for Predicting the Response of Unbonded Concrete Overlays in a Faulting Prediction Model. **Transportation Research Record** 2673.10 (2019): 762-769.
  34. DeSantis, J. W., and J. M. Vandenbossche. Redevelopment of Artificial Neural Networks for Predicting the Response of Bonded Concrete Overlays of Asphalt for use in a Faulting Prediction Model. *Transportation Research Record*, Under Review.
  35. Montgomery, D. Design and Analysis of Experiments 8<sup>th</sup> Edition. John Wiley & Sons, Inc., New York, 2013.
  36. MATLAB and Statistics Toolbox Release 2013a, The MathWorks, Inc., Natick, MA.
  37. Sachs, S. **Development of a Joint Faulting Model for Unbonded Concrete Overlays of Existing Concrete Pavements Through a Laboratory and Numeric Analysis**. PhD Dissertation, University of Pittsburgh, 2017.
  38. Khazanovich, L. **Structural Analysis of Multi-Layered Concrete Pavement Systems**. PhD Dissertation. University of Illinois, Urbana, 1994.
  39. DeSantis, J.W., J.M. Vandenbossche, K. Alland, and J. Harvey. Development of Artificial Neural Networks for Predicting the Response of Bonded Concrete Overlays of Asphalt for Use in a Faulting Prediction Model. **Transportation Research Record: Journal of the Transportation Research Board**, No. 2672, 2018. pp. 360-370.
  40. Ripley, B.D. **Pattern Recognition and Neural Networks**. Cambridge University Press, 1996.
  41. Larson, G., and B. Dempsey. **Enhanced integrated climatic model**. University of Illinois, Urbana, IL, 2003.
  42. Janssen, D.J. and M. B. Snyder. The Temperature-Moment Concept for Evaluating Pavement Temperature Data. **Journal of Infrastructure Engineering**, Vol. 6, No. 2, 2000, pp. 81-83.
  43. Pavement Systems LLC. **A Superpave Binder Selection Program**. Federal Highway Administration Asphalt Team, Bethesda, MD, 2005.
  44. Vandenbossche JM, Dufalla N, Li Z. Bonded concrete overlay of asphalt mechanical-empirical design procedure. **International Journal of Pavement Engineering**, Vol. 18, No. 11, 2017, 1004-1015.
  45. Portland Cement Association. Design of concrete pavement for city streets. Portland Cement Association, 1974.
  46. Zollinger DG, Buch N, Xin D, Soares J. Performance of CRCP Volume 6-CRCP Design, Construction, and Performance. **FHWA-RD-97-151**, Report, Washington, DC., 1998.
  47. Donnelly, C.A., DeSantis, J.W., Vandebossche, J.M., and Sachs, S.G., Mechanistic-Empirical Faulting Prediction Model for Unbonded Concrete Overlays of Concrete. *Transportation Research Board*, **Transportation Research Record**, In Press

## Appendix A

The concrete coefficient of thermal expansion (COTE x10<sup>-6</sup>/°F) data provided from PennDOT is displayed in Tables A-1 to A-3.

Table A-1 – Concrete Coefficient of Thermal Expansion (COTE x10<sup>-6</sup>/°F)

District	Cylinder / Core	Proj SR	Sec.	Mix Design	Lithology	Lithology	COTE US
1	AA cylinder	376	A03	14-201	LS	GL	<b>3.98</b>
1	AA cylinder	376	A03	14-201	LS	GL	<b>3.93</b>
1	AA cylinder	376	A03	14-201	LS	GL	<b>3.89</b>
1	AA Pave cylinder	90085	0.00		LS	GL	<b>3.89</b>
1	AA Pave cylinder	90085	0.00		LS	GL	<b>4.05</b>
1	AA Pave cylinder	90085	0.00		LS	GL	<b>3.87</b>
2	AA Pave cylinder	22	C10	14-BC11H	DO/LS	DO/LS	<b>4.74</b>
2	AA Pave cylinder	22	C10	14-BC11H	DO/LS	DO/LS	<b>4.67</b>
2	AA Pave cylinder	322	150.00	14-430	DO/LS	DO/LS	<b>4.93</b>
2	AA Pave cylinder	322	150.00	14-430	DO/LS	DO/LS	<b>4.86</b>
2	AA Pave cylinder	220	C08	14-430	LS	DO/LS	<b>3.82</b>
2	AA Pave cylinder	220	C08	14-430	LS	DO/LS	<b>3.94</b>
5	AA Pave cylinder	61	11S	14-200-4	SSCG	SSCG	<b>6.09</b>
5	AA Pave cylinder	61	11S	14-200-4	SSCG	SSCG	<b>5.97</b>
5	AA Pave cylinder	61	11S	14-200-4	SSCG	SSCG	<b>6.11</b>
5	AA Pave cylinder	61	11S	14-200-4	SSCG	SSCG	<b>6.04</b>
6	AA Pave cylinder	202	330	14-253#4	DO	QS	<b>4.81</b>
6	AA Pave cylinder	202	330	14-253#4	DO	QS	<b>4.81</b>
6	AA Pave cylinder	95	BRO	16-203#2	DO	QS	<b>4.81</b>
6	AA Pave cylinder	95	BRO	16-203#2	DO	QS	<b>4.81</b>
6	AA-LL	95	CP2	14-16224	DO	QS	<b>5.29</b>
6	AA-LL	95	CP2	14-16224	DO	QS	<b>5.06</b>
6	AA-LL	95	CP2	14-16224	DO	QS	<b>5.04</b>
6	AA-LL	95	CP2	14-16224	DO	QS	<b>4.92</b>
6	AAPAVE cylinder	95	BRO	16-203#2	AR	QS	<b>5.33</b>



Table A-2 – Concrete Coefficient of Thermal Expansion (COTE x10<sup>-6</sup>/°F) PART II

District	Cylinder / Core	Proj SR	Sec.	Mix Design	Lithology	Lithology	COTE US
6	AAPAVE cylinder	95	BRO	16-203#2	AR	QS	<b>5.33</b>
9	AA Structural cylinder	4019	4.00	14-0517	DO	GL	<b>5.50</b>
9	AA Structural cylinder	4019	4.00	14-0517	DO	GL	<b>5.51</b>
9	AAPAVE cylinder	219	20E	17-001	CSS/SLS	SS	<b>5.08</b>
9	AAPAVE cylinder	219	20E	17-001	CSS/SLS	SS	<b>5.12</b>
9	AA Pave cylinder	219	38M	15-113	DO	SS	<b>5.24</b>
9	AA Pave cylinder	219	38M	15-113	DO	SS	<b>5.20</b>
9	AA Pave cylinder	4010	11S	17-617	DO	GL	<b>5.51</b>
9	AA Pave cylinder	4010	11S	17-617	DO	GL	<b>5.51</b>
10	AA Pave cylinder	80	540.00	14-001	GL	GL	<b>4.89</b>
10	AA Pave cylinder	80	540.00	14-001	GL	GL	<b>4.89</b>
11	AA Pave cylinder	376	L04	14-200	LS	GL	<b>4.01</b>
11	AA Pave cylinder	376	L04	14-200	LS	GL	<b>3.98</b>
11	AA#8GL	376	L04	14-224	GL	GL	<b>5.67</b>
11	AA#8GL	376	L04	14-224	GL	GL	<b>5.77</b>
11	AA Pave cylinder	376	L04	14-200	LS	GL	<b>5.77</b>
11	AA Pave cylinder	376	L04	14-200	LS	GL	<b>5.77</b>
11	AA Structural cylinder	1018	A01	14-1525	CSS	GL	<b>4.98</b>
11	AA Structural cylinder	1018	A01	14-1525	CSS	GL	<b>4.98</b>
11	AA Pave cylinder	65	B28	15-274	CSS	GL	<b>4.56</b>
11	AA Pave cylinder	65	B28	15-274	CSS	GL	<b>4.58</b>
12	AA Pave cylinder	90085	0.00	14-210	CSS	GL	<b>5.03</b>
12	AA Pave cylinder	90085	0.00	14-210	CSS	GL	<b>5.02</b>
12	AA Pave cylinder	90085	0.00	14-210	CSS	GL	<b>5.12</b>
12	AA Pave cylinder	90085	0.00	14-210	CSS	GL	<b>4.93</b>
12	AA Pave cylinder	90085	0.00	16-AA	CSS	GL	<b>4.88</b>

Table A-3 – Concrete Coefficient of Thermal Expansion (COTE x10<sup>-6</sup>/°F) PART III

<b>District</b>	<b>Cylinder / Core</b>	<b>Proj SR</b>	<b>Sec.</b>	<b>Mix Design</b>	<b>Lithology</b>	<b>Lithology</b>	<b>COTE US</b>
12	AA Pave cylinder	90085	0.00	16-AA	CSS	GL	<b>4.88</b>
12	AA Pave cylinder	90085	0.00	16-041SF	CSS	GL	<b>4.95</b>
12	AA Pave cylinder	90085	0.00	16-041SF	CSS	GL	<b>5.04</b>
12	AA Pave cylinder	90085	0.00	16-274	CSS	GL	<b>5.02</b>
12	AA Pave cylinder	90085	0.00	16-274	CSS	GL	<b>5.06</b>
12	AA Pave cylinder	90085	0.00	17-274	CSS	GL	<b>5.06</b>
12	AA Pave cylinder	90085	0.00	17-274	CSS	GL	<b>5.06</b>

## Appendix B

Tables B-1 to B-3 present additional information on the sections used for the BCOA model calibration.

Table B-1 – Calibration sections project information.

Source	Section ID	Overlay const. date	Age, yrs.	Estimated ESALs	Long., deg	Lat., deg
MnROAD	Cell60_PCC	Oct-04	8.59	8.45E+06	44.6	-93.8
MnROAD	Cell60_PL_PCC	Oct-04	6.98	1.70E+06	44.6	-93.8
MnROAD	Cell60_FULL	Oct-04	8.59	8.45E+06	44.6	-93.8
MnROAD	Cell60_PL_FULL	Oct-04	6.98	1.70E+06	44.6	-93.8
MnROAD	Cell61_PCC	Oct-04	8.59	8.45E+06	44.6	-93.8
MnROAD	Cell61_PL_PCC	Oct-04	6.98	1.70E+06	44.6	-93.8
MnROAD	Cell61_FULL	Oct-04	6.50	6.20E+06	44.6	-93.8
MnROAD	Cell61_PL_FULL	Oct-04	4.70	1.14E+06	44.6	-93.8
MnROAD	Cell62_PCC	Oct-04	8.59	8.45E+06	44.6	-93.8
MnROAD	Cell62_PL_PCC	Oct-04	6.98	1.70E+06	44.6	-93.8
MnROAD	Cell63_PCC	Oct-04	8.59	8.45E+06	44.6	-93.8
MnROAD	Cell63_PL_PCC	Oct-04	6.98	1.70E+06	44.6	-93.8
MnROAD	Cell92_FULL	Oct-97	12.51	1.16E+07	44.6	-93.8
MnROAD	Cell92_PL_FULL	Oct-97	12.51	3.19E+06	44.6	-93.8
MnROAD	Cell95_PCC	Oct-97	4.95	4.76E+06	44.6	-93.8
MnROAD	Cell95_PL_PCC	Oct-97	4.95	1.33E+06	44.6	-93.8
MnROAD	Cell95_FULL	Oct-97	4.95	4.76E+06	44.6	-93.8
MnROAD	Cell95_PL_FULL	Oct-97	4.95	1.33E+06	44.6	-93.8
MnROAD	Cell96_PCC	Oct-97	13.53	1.25E+07	44.6	-93.8
MnROAD	Cell96_PL_PCC	Oct-97	13.98	3.50E+06	44.6	-93.8
MnROAD	Cell96_FULL	Oct-97	12.66	1.17E+07	44.6	-93.8
MnROAD	Cell97_FULL	Oct-97	12.51	1.16E+07	44.6	-93.8
MnDOT	CSAH 22_002-622-033	2013	3.00	1.28E+05	45.3	-93.2
MnDOT	CSAH 22_CP 12-14-22	2012	4.00	1.69E+05	45.3	-93.2
MnDOT	CSAH 22_02-622-31	2011	5.00	2.26E+05	45.3	-93.2
MnDOT	TH 56_2006-26	2010	6.00	9.06E+04	44.1	-92.9
MnDOT	TH 30_0705-14	1993	22.00	3.39E+05	43.89	-94.2
MnDOT	CSAH 7_43-607-14	2009	7.00	3.26E+05	44.8	-94.3
MnDOT	CSAH 2_43-602-(24-25)	2011	5.00	2.19E+05	44.82	-94.17
NCHRP 1-61	06-6	1997	22.00	4.69E+06	40.63	-102.55
NCHRP 1-61	06-121A	2011	8.00	3.13E+06	39.87	-105.09
NCHRP 1-61	06-121B	2001	18.00	4.39E+06	39.58	-105.09
NCHRP 1-61	06-83A	2005	14.00	5.91E+06	39.61	-104.81
NCHRP 1-61	06-83B	1999	20.00	1.02E+07	39.62	-104.82
NCHRP 1-61	17-27	2003	16.00	1.00E+07	39.82	-89.10
NCHRP 1-61	22-167	1992	27.00	5.57E+06	31.93	-92.64
NCHRP 1-61	29-60	1999	20.00	1.91E+07	36.84	-94.41

Table B-2 – Calibration sections design features.

Section ID	Avg. joint spacing	Lane width	Tied PCC shoulder	Dowel diameter, in
Cell60_PCC	5	6	No, AC	None
Cell60_PL_PCC	5	6	No, AC	None
Cell60_FULL	5	6	No, AC	None
Cell60_PL_FULL	5	6	No, AC	None
Cell61_PCC	5	6	No, AC	None
Cell61_PL_PCC	5	6	No, AC	None
Cell61_FULL	5	6	No, AC	None
Cell61_PL_FULL	5	6	No, AC	None
Cell62_PCC	5	6	No, AC	None
Cell62_PL_PCC	5	6	No, AC	None
Cell63_PCC	5	6	No, AC	None
Cell63_PL_PCC	5	6	No, AC	None
Cell92_FULL	10	12	No, AC	1
Cell92_PL_FULL	10	12	No, AC	1
Cell95_PCC	5	6	No, AC	None
Cell95_PL_PCC	5	6	No, AC	None
Cell95_FULL	5	6	No, AC	None
Cell95_PL_FULL	5	6	No, AC	None
Cell96_PCC	5	6	No, AC	None
Cell96_PL_PCC	5	6	No, AC	None
Cell96_FULL	5	6	No, AC	None
Cell97_FULL	10	12	No, AC	None
CSAH 22_002-622-033	6.25	6.25	No, AC	None
CSAH 22_CP 12-14-22	6	6	No, AC	None
CSAH 22_02-622-31	6	6, 7	No, AC	None
TH 56_2006-26	15	13.5	No, AC	1
TH 30_0705-14	12	12	No, AC	None
CSAH 7_43-607-14	6	6, 7	No, Agg.	None
CSAH 2_43-602-(24-25)	6	6, 7	No, Agg.	None
06-6	10	12	Yes	1
06-121A	6	6	Yes	None
06-121B	6	6	Yes	None
06-83A	6	6	Yes	None
06-83B	6	6	Yes	None
17-27	5.5	5.5	No, Agg.	None
22-167	4	4	Yes	None
29-60	4	4	No, AC	None

Table B-3 – Calibration sections structural details.

Section ID	Overlay thickness, in	Overlay EMOD, psi	Overlay MOR, psi	Overlay CTE, x10 <sup>-6</sup> in/in/°F	Overlay cement content, lbs.	Asphalt thickness, in
Cell60_PCC	5.0	4.58E+06	595	4.11	400	7.0
Cell60_PL_PCC	5.0	4.58E+06	595	4.11	400	7.0
Cell60_FULL	5.0	4.58E+06	595	4.11	400	7.0
Cell60_PL_FULL	5.0	4.58E+06	595	4.11	400	7.0
Cell61_PCC	5.0	4.42E+06	545	4.39	400	7.0
Cell61_PL_PCC	5.0	4.42E+06	545	4.39	400	7.0
Cell61_FULL	5.0	4.42E+06	545	4.39	400	7.0
Cell61_PL_FULL	5.0	4.42E+06	545	4.39	400	7.0
Cell62_PCC	4.0	4.89E+06	575	3.89	400	8.0
Cell62_PL_PCC	4.0	4.89E+06	575	3.89	400	8.0
Cell63_PCC	4.0	5.02E+06	560	4.11	400	8.0
Cell63_PL_PCC	4.0	5.02E+06	560	4.11	400	8.0
Cell92_FULL	6.0	4.80E+06	860	5.5	650	7.0
Cell92_PL_FULL	6.0	4.80E+06	860	5.5	650	7.0
Cell95_PCC	3.0	4.70E+06	840	5.5	650	10.0
Cell95_PL_PCC	3.0	4.70E+06	840	5.5	650	10.0
Cell95_FULL	3.0	4.70E+06	840	5.5	650	10.0
Cell95_PL_FULL	3.0	4.70E+06	840	5.5	650	10.0
Cell96_PCC	6.0	4.70E+06	890	5.5	650	7.0
Cell96_PL_PCC	6.0	4.70E+06	890	5.5	650	7.0
Cell96_FULL	6.0	4.70E+06	890	5.5	650	7.0
Cell97_FULL	6.0	4.70E+06	830	5.5	650	7.0
CSAH 22_002-622-033	6.0	4.00E+06	650	6.0	420	4.0
CSAH 22_CP 12-14-22	6.0	4.00E+06	650	6.0	405	4.0
CSAH 22_02-622-31	6.0	4.00E+06	650	6.0	400	3.0
TH 56_2006-26	6.0	4.00E+06	738	3.8	413	8.5
TH 30_0705-14	6.0	4.00E+06	507	6.6	420	7.5
CSAH 7_43-607-14	5.0	4.00E+06	679	5.3	420	6.0
CSAH 2_43-602-(24-25)	5.0	4.00E+06	650	5.3	420	5.0
06-6	6.0	4.00E+06	650	4.8	520	9.0
06-121A	6.0	4.00E+06	650	4.8	520	13.0
06-121B	7.0	4.00E+06	650	4.8	520	12.0
06-83A	8.0	4.00E+06	650	4.8	520	16.0
06-83B	6.0	4.00E+06	650	4.8	520	13.0
17-27	5.0	3.60E+06	900	3.8	534	8.0
22-167	5.0	4.00E+06	600	6.0	564	9.0
29-60	4.5	4.00E+06	650	4.5	592	5.0